Dissertation

Load Partition and Microstructural Evolution at High Temperature in Multiphase Lightweight Metallic Materials

ausgeführt zum Zwecke der Erlangung des akademischen Grades eines Doktors der technischen Wissenschaften unter der Leitung von

Ass. Prof. Dipl.-Ing. Dr. Guillermo Requena
Institut für Werkstoffwissenschaft und Werkstofftechnologie

eingerichtet an der Technischen Universität Wien,
Fakultät Maschinenwesen und Betriebswissenschaften

von

Dipl. Ing. David Canelo Yubero

Matr. Nr.: 0928787

Brunnengasse 41/6-9
A-1160 Wien

Wien, im März 2014

.....
David Canelo Yubero

“We all have dreams. But in order to make dreams come into reality,
it takes an awful lot of determination, dedication, self-discipline and effort”

Jesse Owens
Olympic gold-medalist runner

Acknowledgements

First of all I would like to thank to Assistant Prof. Dipl.-Ing. Dr.techn. Guillermo Requena for being my scientific guide, for his immense patience and the most important, for being my friend. I can not forget our beginning with the diffraction experiments. It was a great adventure. I really enjoyed this trip. Sometimes is impossible to express in words everything. May be the best way is to say: Gracias Che!

I am very thankful to Em.O.Univ.Prof. Dipl.-Ing. Dr.techn Hans-Peter Degischer. You opened me the "door" of this Institute and it is the reason why I am right now here. Unforgettable our victory in the Drachenboot. Hasta la Victoria siempre! Gracias, Profe!

I am in debt with Prof. Dr. rer. nat. Walter Reimers for accepting to be one of the examiners and his time while reviewing this thesis. Danke vielmals!

The collaboration of Christoph Etzlstorfer was inestimable to make possible this work. It was a hard task although it was worth. Vielen herzlichen Dank!

I thank to F. Warchomicka, Cecilia, Pere, Richi, Robert and Marta (my "spanish adviser/secretary"), not only because of their help at the Institute with sample preparation, metallography, Ti discussions, EBSD measurements, dilatometer tests, but also and most valuable for me the personal affection of all these years.

I am also in debt to Edith Asiemo and Maja Jaber for the sample preparation, to Christian for the technical support and to Silvia, Tanja and Dagma (bureaucracy solvers ☺).

To all my fellows during all these years: Esteban, Domo, José, Camilo and F. Lasagni, my 'roomies' (unforgettable our walks to Billa and basket championships), Abel and Julián: all you rock!

To all my friends not only in Austria and Spain but also around the World: I miss you a lot. I wish you were here.

Obviously, I can not forget to my family. They have been always here for me, with moral and strength support during all my life.

Last but most definitively not least, to Austria for the financial support provided during these years. None of this work would have been possible without these projects:

- "FWF- Microstructure design of cast Al alloys for high temperature" - P22876.
- "K-Project for Non-Destructive Testing and Tomography" – COMET-Program Grant No.820492.

This thesis is dedicated to the memory of my Grandparents.

David

Kurzfassung

Aluminium und Titanlegierungen umgeben uns im täglichen Leben und sind essenziell wenn Gewichtsminimierung gleichzeitig mit relativ hoher Festigkeit notwendig ist. Bei Raumtemperatur kann die Festigkeit mit der Einbringung von verstärkenden keramischen Phasen, wodurch sich ein Metall-Matrix-Verbundwerkstoff bildet, erhöht werden. Die Verwendung von rigiden intermetallischen Phasen ist eine Alternative, wenn die Herstellung der Verbundwerkstoffe zu hohe Kosten erzeugt.

Die Untersuchung der Lastaufteilung zwischen den unterschiedlichen Phasen unter dem Einfluss externer thermo-mechanischer Belastung ist wichtig, um das Verhalten von mehrphasigen Legierungen während reeller Einsatzbedingungen zu verstehen. Das Fehlen solcher wissenschaftlicher Analysen über die Lastverteilung in Al und Ti-Legierungen mit mehrphasigen Gefügen bei hohen Temperaturen ist die Hauptmotivation für diese Arbeit.

Beugungstechniken, die in der Lage sind ein Material bis zu mehreren cm zu durchdringen, sind notwendig um die Entwicklung der Lastaufteilung während externer Lastaufbringung zu untersuchen. Neutronenquellen mit hohem Flux und Synchrotrone der dritten Generation sind als Beugungsquellen im Vergleich zu laborgestützten Röntgenquellen ideal für diesen Zweck. Des Weiteren sind Erfassungszeiten von ~ 3 min bei Neutronenbeugungen und ≤ 1s bei Synchrotron-Röntgenbeugung geeignete Verfahren um in situ Analysen bei hohen Temperaturen, bei welchen Relaxationseffekte eine relevante Rolle spielen können, durchzuführen.

Das Ziel dieser Arbeit ist die Untersuchung der Lastaufteilung und der mikrostrukturellen Evolution bei hohen Temperaturen von mehrphasigen Leichtmetallen mittels in situ Neutronen- und Synchrotron-Röntgenbeugung.

Die Gusslegierungen AlSi12 und AlSi10Cu6Ni2 wurden mit den lösungsgeglühten Zuständen von 1h und 4h bei 500°C sowie dem Gusszustand während erfolgender Hochtemperaturdruckversuche untersucht. Der Effekt der Lastverteilung unterschiedlicher Phasen wurde mit in situ Synchrotron-Röntgenbeugung analysiert. Das eutektische Si in der Al Kolbenlegierung ist in der Lage größere Last zu tragen als die AlSi12 Legierung in korrespondierenden Lösungsglühzuständen sowie unter identischen extern aufgebrachten Dehnungen. Für dieses Verhalten sind Kupfer-, Nickel- und Eisen-Aluminide, die ein stark vernetztes 3D Netzwerk mit eutektischem Si bilden, verantwortlich. Der Verlust der lasttragenden Eigenschaft der AlSi12 Legierung mit erfolgtem Lösungsglühen ist auf die Desintegration des 3D Si Netzwerkes, welches durch die Anwesenheit von Aluminiden während des Lösungsglühens partiell verhindert wird, zurückzuführen. Die Rolle der

Aluminide in der Legierung AlSi10Cu6Ni2 zu Beginn der Schädigung ist durch eine plötzliche Verringerung der von Al_2Cu getragenen Last bei höchster Druckfestigkeit der Legierung gekennzeichnet.

In einem weiteren Abschnitt wurden auf pulvermetallurgische Herstellungsweise drei mit SiC Partikel verstärkte Verbundwerkstoffe, von denen zwei durch ein Nassmischverfahren (wet blending) mit 2124 und 6061 Al-Legierungen sowie eine durch Kugelmühlen mit 2124 hergestellt wurden, thermischen Zyklen unterworfen, um die Unterschiede in den beobachteten Kriechwiderständen zu erklären. Der Einfluss der unterschiedlichen Mischverfahren auf die Relaxation während des thermischen Zyklierens wurde mittels Neutronenbeugung untersucht. Die thermischen Spannungen werden bei $T \geq 90°C$ teilweise abgebaut. Der Verbundwerkstoff, der durch Kugelmühlen produziert wurde, zeigte geringere Relaxation von thermischen Spannungen und höhere Kriechbeständigkeit im Vergleich zu den Verbundwerkstoffen die mittels Nassmischverfahren hergestellt wurden. Die durchschnittlichen thermischen axialen Druckspannungen der Matrizen betrugen nach erfolgter Aufheizung auf 230-300°C bei 2124 (Kugelmühlen-Verfahren) ~ 50MPa, bei 6061 ~ 15MPa (Nassmischverfahren) und bei 2124 ~ 10MPa (Nassmischverfahren), welche mit Raten von $\leq 5 \times 10^{-9} - 3 \times 10^{-8}\ s^{-1}$ abgebaut wurden.

Schließlich wurde eine Ti662 Legierung, die mit 12 vol.% und 20 vol.% TiC Teilchen über pulvermetallurgischem Weg hergestellt wurde, untersucht. Bei diesen Verbundwerkstoffen wurden durch Hochtemperatur Zugversuche mittels Synchrotron-Röntgenbeugung die Kapazität der Lastaufnahme unterschiedlicher Phasen und deren Schädigungsmechanismen erkundet. Die kleinere Größe der α-Lamellen der untersuchten teilchen-verstärkten Verbundwerkstoffe führte zu einer höheren Duktilität im Vergleich zur nicht verstärkten pulvermetallurgisch hergestellten Matrix. Die Präsenz von TiC Teilchen spielt keine effektive verstärkende Rolle aufgrund deren räumlichen inhomogenen Verteilung und der Tatsache, dass die lokale Dehnungsentwicklung der TiC Partikel die Fähigkeit zur teilweisen Lastaufnahme zeigt. Die β-Phase verformt sich bereits zu Beginn der Hochtemperatur Zugversuche plastisch. Die α-Phase in der pulvermetallurgisch hergestellten Ti662 deformiert sich mittels des Mechanismus der Kornrotation, wodurch eine geometrische Umorientierung der Lamellen stattfindet, sowie einer kristallographischen Rotation innerhalb der Lamellen. Andererseits zeigt die β-Phase eine Erhöhung der Missorientierung innerhalb einzelner Körner. Die Ti662 Ingot Metalllegierung ermöglicht eine in situ Analyse der Texturentwicklung aufgrund kleinerer Korngröße.

Abstract

Aluminium and titanium alloys surround our lives and are essential when weight minimization is required together with relatively high strengths. At room temperature, strength can be improved by reinforcing these alloys with ceramics phases, resulting in the formation of metal matrix composites. The introduction of rigid intermetallic phases is an alternative option when the production of the composites raises the costs.

The study of the load partition between phases under the effect of external (thermo-) mechanical loads is crucial to understand the behaviour of multiphase alloys during real service conditions. The lack of scientific works analysing the load partition in Al and Ti multiphase alloys at high temperature is the main motivation of the present work.

Bulk diffraction techniques capable to penetrate up to a few cm within materials are necessary to follow in situ the evolution of the load partition under the effect of external loads. Neutron sources with high flux and the third-generation synchrotron diffraction sources are ideal for this purpose compared with traditional x-ray laboratory sources. Furthermore, acquisition times up to ~ 3 min for the neutron diffraction and below 1 s for the synchrotron diffraction make them suitable tools for in situ analysis at high temperature, where relaxation effects can play a relevant role.

The aim of this work is the study of the load partition and the microstructural evolution at high temperature in selected multiphase lightweight metallic materials by means of in situ neutron and synchrotron diffraction techniques.

Cast AlSi12 and AlSi10Cu6Ni2 alloys, undergoing solution treatments during 1h and 4h at 500°C, are compared with their respective as cast conditions during high temperature compression tests. The effect of the load partition between different phases is analyzed by in situ synchrotron diffraction. The eutectic Si in the aluminium piston alloy is able to bear a higher load than in the AlSi12 alloy in corresponding heat treatment conditions and for identical externally applied strains. Cu, Ni and Fe aluminides, forming highly contiguous 3D networks with the eutectic Si are responsible for this behaviour. The decrease of the load carrying capability in the AlSi12 with solution treatments is due to the disintegration of 3D Si networks, which on the other hand, is partially preserved by the aluminides after solution treatments in the AlSi10Cu6Ni2 alloy. The role played by aluminides on damage onset in the AlSi10Cu6Ni2 alloy is revealed by the sudden decrease of the load born by Al_2Cu at the point of maximum strength of this alloy.

In a different section, three SiC-particle reinforced composites produced by powder metallurgy, two of them by wet blending using 2124 and 6061 Al-alloys, and one by ball

milling using a 2124 Al-alloy, are subjected to thermal cycling in order to explain the differences observed in their creep resistance. The effect of the blending route on the stress relaxation during thermal cycling is studied by in situ neutron diffraction. The thermal stresses partially relax at $T \geq 90°C$. The higher creep resistance of the composite produced by ball milling shows less relaxation of thermal stresses in comparison with the wet blended composites. The average axial compressive thermal stresses are ~ 50 MPa, ~ 15 MPa and ~ 10 MPa after heating to 230 - 300°C in the matrices of the ball milling 2124, wet blending 6061 and wet blending 2124 composites, respectively, which relax at rates $\leq 5 \times 10^{-9} - 3 \times 10^{-8}\ s^{-1}$.

Finally, a Ti662 alloy reinforced with 12% and 20% volume fractions of TiC particles and produced by powder metallurgy, is subjected to high temperature tensile tests to compare the load bearing capability of the different phases as well as the different deformation mechanisms. Two Ti662 matrices, produced by powder metallurgy and ingot metallurgy are used as reference alloys. Synchrotron diffraction is the selected tool for this study. The smaller α-lamella size of the PRMs in comparison with the unreinforced powder metallurgy matrix is responsible for their higher ductility. Furthermore, the presence of the TiC particles does not play an effective reinforcing role because of their inhomogeneous spatial distribution although local strain evolution shows that they are able to bear part of the load. The β-phase plastifies practically at the beginning of the tensile tests. The α-phase deforms by a mechanism of grain rotation in the Ti662 alloy produced by powder metallurgy as a consequence of the geometrical reorientation of the lamellae and crystallographic rotation within the lamellae. On the other hand, the β-phase shows an increase of crystallographic misorientation within individual grains. The Ti662 ingot metallurgy alloy, because of its smaller grain size, allows following in situ the texture evolution.

Contents

1 Introduction

Aluminium alloys are next to steel in metal world production [1]. Their low density, strength, recyclability, corrosion resistance, ductility, formability and conductivity make them essential in our lives. Automotive sector, building, transport, engineering and packing are the main application areas [2].

Titanium alloys show high specific stiffness and strength up to high temperatures and excellent corrosion resistance which contribute to their use in aerospace, automotive and offshore applications. Furthermore, the high biocompatibility makes them also suitable for medical applications [3].

One of the advantages of aluminium and titanium alloys compared to steel for structural applications lies in their higher specific stiffness for the cases of bars and membranes under elastic bending. Fig. 1.1 shows the specific stiffness of a rod under compression/tensile (E/ρ) together with that of a beam ($E^{1/2}/\rho$) and of a membrane ($E^{1/3}/\rho$) under bending in an Ashby diagram [4-5]. When components are loaded under bending (beam and membrane), the light alloys result in weight minimization.

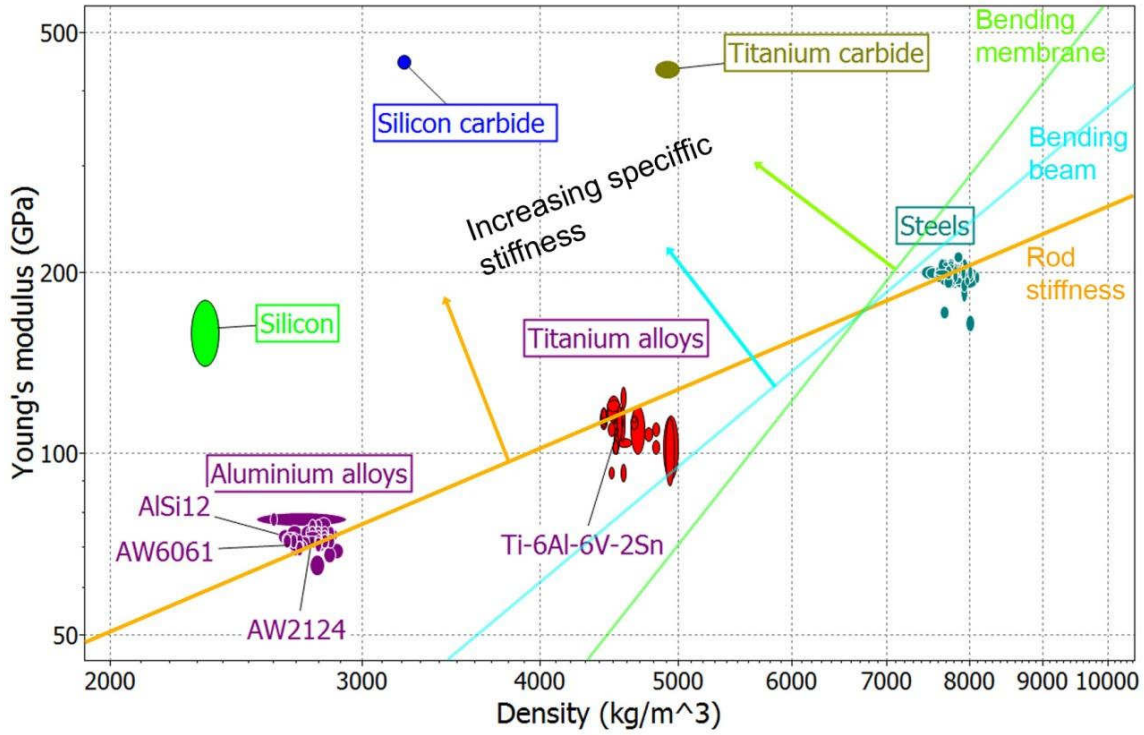

Fig. 1.1. Specific stiffness at RT of aluminium, titanium and steel alloys together with silicon, silicon carbide and titanium carbide [4-5]. Lines corresponding to a rod under elastic compression/tension stiffness and beam/membrane under elastic bending are shown.

As it can be inferred from Fig. 1.1, one way to improve the specific stiffness of the alloys is by reinforcing them with ceramics. This results in the formation of metal matrix composites (MMC): heterogeneous materials that combine the properties of metals and ceramics. Furthermore, the properties of MMCs are given not only by the properties of the individual components but also by their morphology, size, distribution, proportion, etc.

In this work, the load partition between ductile aluminium matrices and different types of rigid phases, i.e. eutectic Si, intermetallics and SiC, is studied under the effect of selected thermo-mechanical loads. Similarly, the load partition between α-β Ti phases and TiC is investigated in situ during tensile tests at high temperature. Also, the microstructural evolution of titanium alloys is studied in situ aiming at identifying unambiguously the deformation mechanisms of each phase.

The main properties for aluminium and titanium alloys related to this work are presented in Chapter 2. The strengthening mechanisms in MMCs, high energy diffraction methods and their application to determine internal stresses are also commented. Motivation and hypotheses of this work end this chapter.

Chapter 3 presents the studied materials and different high energy diffraction experimental setups together with the methodology used to study the microstructure evolution during deformation of Ti alloys.

The results are shown in Chapter 4, i.e., crystallographic strains, texture analysis and the evolution of the microstructure.

Chapter 5 includes the interpretation and discussion of results, analysing the load partition between the phases of Al and Ti alloys under different thermo-mechanical load conditions and the deformation mechanisms in Ti alloys.

Finally, Chapter 6 summarizes the principal conclusions of this work.

2 State of the Art

2.1 Light metals

Traditionally, aluminium and titanium have been included in the group of "light metals" together with magnesium and beryllium. The origin of this name is because they contribute to reduce the weight of components and structures [1].

2.1.1 Aluminium

Pure aluminium has a face-centered cubic (fcc) crystal structure with a melting point of 660°C, density of 2.7 g cm^{-3} and elastic modulus E = 70 GPa at room temperature (RT) [1]. Slip planes are {111} type (4 independent) and slip direction is <110> (3 in every (111) plane). This results in 12 independent slip systems {111} <110> (Fig. 2.1).

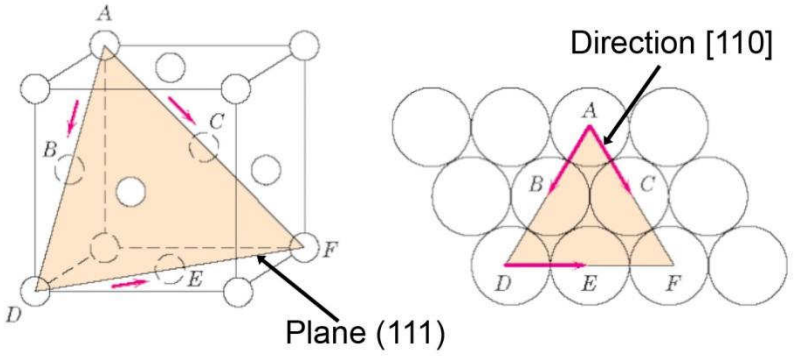

Fig. 2.1. Slip systems in a fcc crystal structure [6].

2.1.2 Titanium

Pure titanium exhibits from the melting point of 1670°C a body-centered cubic (bcc) crystal structure called β-phase undergoing an allotropic transformation at 882°C into a hexagonal closed-packed (hcp) crystal structure, also named α-phase (Fig. 2.2). The Burgers relationship describes this process [7-8]:

$$\beta\text{-}(110) \leftrightarrow \alpha\text{-}(0002)$$

$$\beta\text{-}[1\bar{1}1] \leftrightarrow \alpha\text{-}[11\bar{2}0]$$

According to this expression, the most densely packed (110) planes of the β-phase transform into the basal (0002) planes of the α-phase.

The α-phase has a density of 4.5 g cm^{-3} and lattice parameters of a = 2.95 Å and c = 4.68 Å at RT [8]. This represents a ratio c/a < 1.633, i.e. lower than the ideal value for the hcp crystal structure. Therefore, a slight atomic distortion is provoked during the

allotropic transformation by the contraction of the c axis leading to an increase of the spacing between prismatic planes.

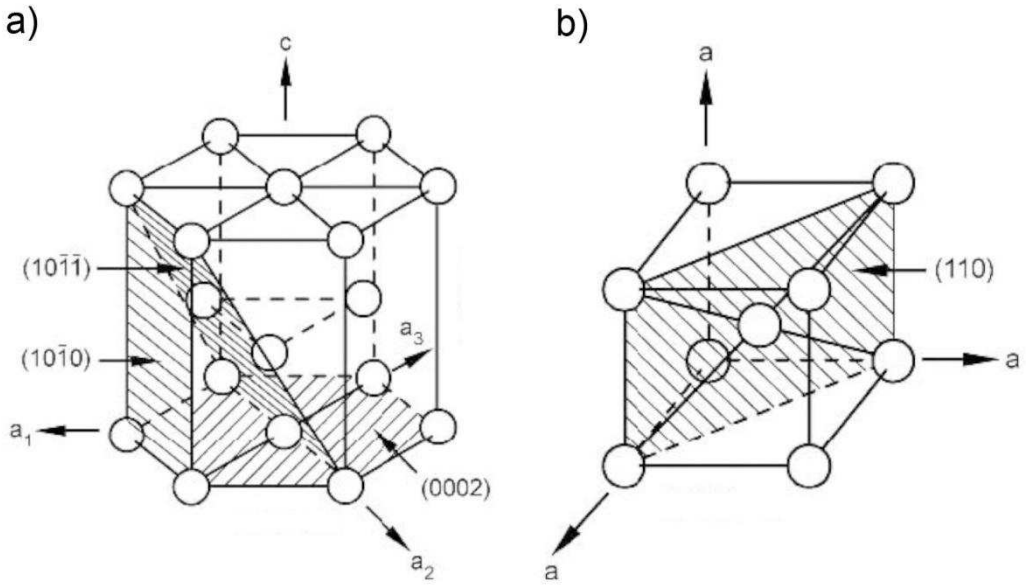

Fig. 2.2. Crystal structure of Ti a) α-phase and b) β-phase [8].

The Young´s modulus depends on the lattice orientation as can be seen in Fig. 2.3 for the α-phase. There is a marked change in E that results in a reduction of up to ~ 30% with increasing declination angle. The highest E corresponds to the c-axis (normal to the basal plane ~ 145 GPa) while the lowest to the stress perpendicular to the c-axis (normal to prismatic planes ~ 100 GPa) [8].

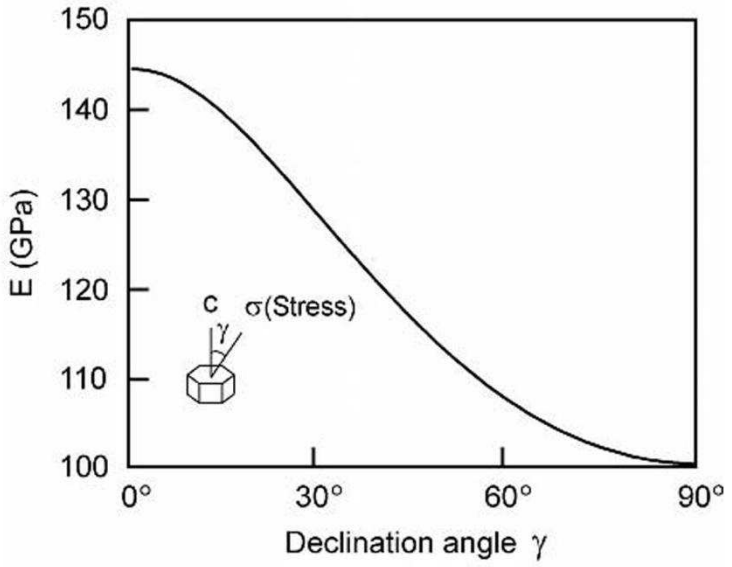

Fig. 2.3. Young´s modulus of the α-phase as a function of declination angle at RT [8].

The slip systems for the α-phase are indicated in Fig. 2.4. The slip direction <$11\bar{2}0$> and prismatic $(10\bar{1}0)$ and basal (0002) planes have three slip systems each. The pyramidal

$\{10\bar{1}1\}$ planes with $<11\bar{2}0>$ slip direction form six slip systems. Since the glide is a combination of basal and prismatic components they can not be considered as independent slip systems and among these twelve slip systems only four are independent. According to the Von-Mises criterion, 5 independent slip systems are required to provoke plastic deformation. This leads to the activation of secondary slip systems such as $<11\bar{2}3>$ $\{11\bar{2}2\}$ with six slip systems and only five independent. Furthermore, because of the ratio c/a < 1.633, the slip is favoured in the prismatic planes. Mechanical twinning can be also activated.

The β-phase has similar slip systems to those observed in bcc metals, i.e., slip direction <111> and slip planes {110} (12 independent slip systems), {112} (12 independent slip systems) and {123} (24 independent slip systems).

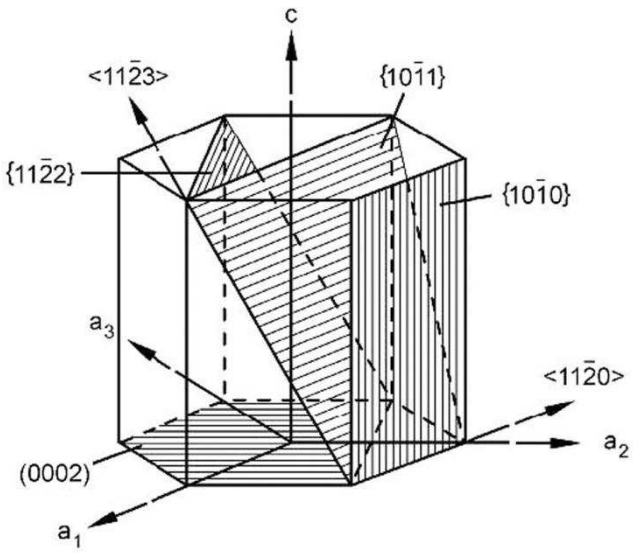

Fig. 2.4. Slip planes and directions for the α-phase [8].

2.2 Light alloys

2.2.1 Aluminium alloys

Aluminium alloys are divided into two major categories, i.e., cast and wrought alloys. Wrought alloys are produced as ingots or billets with subsequent cold/hot mechanical deformation to the final form, while cast alloys are directly cast into the final or semifinal dimensions.

Wrought alloys represent approximately 75% - 80% of the aluminium, produced as plates, sheets, foils, profiles, tubes, rods, bars and wires by rolling, extrusion, forming or forging [1]. A four-digit system is used to designate wrought alloys in both the Aluminium

Association system (AA), most widely recognized in the United States, and the European standard (EN 573). The first digit is the most important and indicates the main alloying elements:

- 1*xxx*: unalloyed composition used in electrical and chemical industries.
- 2*xxx*: copper is the principal alloying element. Widely used in aircrafts.
- 3*xxx*: manganese is the principal alloying element. Used for architectural applications and various products (cans).
- 4*xxx*: silicon is the principal alloying element. Used in welding rods and brazing sheets.
- 5*xxx*: magnesium is the principal alloying element. Used in automotive interiors and products exposed to marine environments.
- 6*xxx*: magnesium and silicon are principal alloying elements. Used in car body.
- 7*xxx*: zinc and magnesium are the principal alloying elements. Used in high-strength applications such as aircrafts structural components.

Cast aluminium alloys are described with a three digits system followed by a decimal value according to the Aluminium Association. There are 8 families of casting alloys and the Al-Si alloys (3*xx.x*) provide nearly the 90% of all shape castings produced [9]. The reason for their wide acceptance is their attractive combination of mechanical and physical properties and excellent castability because of the high fluidity imparted by the presence of eutectic forming elements (usually Si). The main use of these alloys is in machinery and automotive components such as cylinder heads, pistons and valve lifters [9].

The eutectic point of the binary Al-Si system is at ~ 577°C and ~ 12.6 wt.% Si (Fig. 2.5). The eutectic alloy is formed by α-Al and practically pure Si. Slow solidification rate leads to the formation of Si plates embedded in the α-matrix (brittle behavior). Rapid cooling generates a fibrous Si form (with improved ductility and tensile strength). The different Si morphologies present high interconnectivity degree, as showed by Bell et al. in the 1960s [10] by deep etching and verified recently with 3-D techniques [11-12].

Solution heat treatments modify the morphological structure of the eutectic Si, a phenomenon called spheroidization [13]. This results in a loss of interconnectivity and the rounding of eutectic Si (e.g. [12]).

Morphology, distribution and interconnectivity of eutectic Si in Al-Si alloys vary their strength and ductility [12, 14-15].

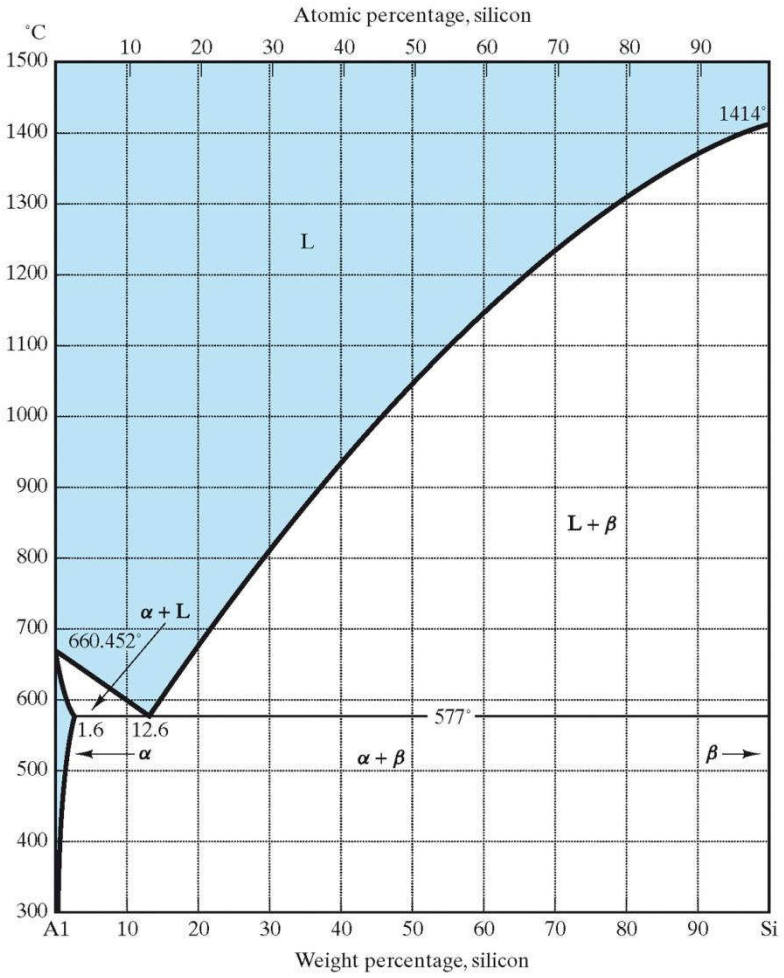

Fig. 2.5. Al-Si equilibrium phase diagram [16].

2.2.2 Titanium alloys

Properties of pure titanium can be modified with alloying elements which are classified in two groups attending to the stabilized phase, i.e., depending on whether they increase or decrease the beta transus temperature (Fig. 2.6). It has to be pointed out that the addition of these elements provokes a change in the phase transformations, occurring via a two-phase region instead of at a defined temperature. The α-stabilizers are the substitutional element Al (the most widely used owing to its good solubility in both the α- and β-phases) and the interstitial elements O, N and C, raising the β transus temperature. The β stabilizing elements are divided into β-isomorphous and β-eutectoid forming elements.

Commercial titanium alloys are usually classified into three different categories: α (with small amounts of β phase), α+β and β (are actually metastable) alloys according to their position in a pseudo-binary section through a β isomorphous phase diagram (Fig. 2.7).

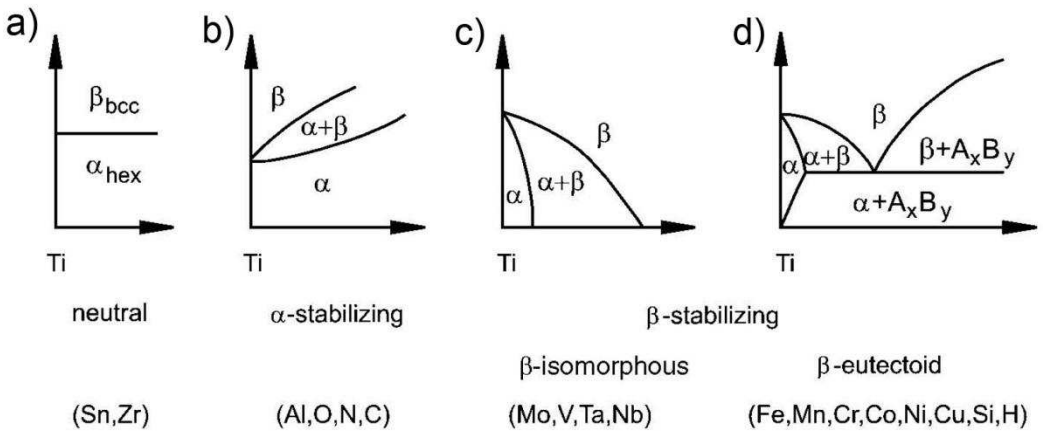

Fig. 2.6. Effect of alloying elements on phase diagrams of titanium alloys [3].

The most widely used titanium α+β alloy is the Ti-6Al-4V (Ti64). It presents high specific strength, thermal stability up to 400°C, excellent machinability, good weldability and good corrosion resistance [17]. When a higher strength is required up to 315°C in secondary structures (due to its low fracture toughness), Ti-6Al-6V-2Sn is a good alternative [17].

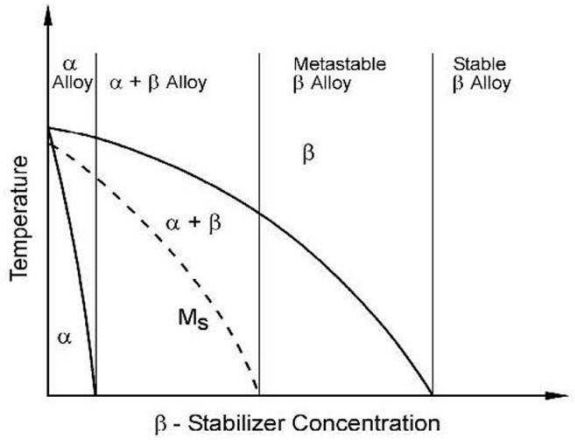

Fig. 2.7. Pseudo-binary section through a β isomorphous phase diagram (schematically) [8].

2.3 Metal matrix composites

A composite (or composite material) is defined as a material that consists of at least two constituents (distinct phases or combinations of phases) which are bonded together along the interface in the composite, each of which originates from a separate ingredient material which pre-exists the composite [18]. A Metal Matrix Composite (MMC) is obtained if one constituent is a metal or alloy forming at least one percolating network and the other constituent is embedded in this metal matrix, serving usually as reinforcement.

2.3.1 Classification of MMCs

There are two different classes of metal matrix composites [19]:

1) Continuously reinforced MMC: either monofilaments of approximately 0.1 mm in diameter (e.g. SiC) or multifilament tows of at least some hundreds of fibres of about 0.01 mm in diameter (e.g. SiC, Al_2O_3, carbon) are embedded within a rather ductile matrix. Percolating ceramic structures can also be used as a continuous reinforcement.
2) Discontinuously reinforced MMC, where either particles, platelets (SiC, Al_2O_3, B_4C), short fibres of high aspect ratio (usually Al_2O_3-SiO_2) or whiskers (forbidden in Europe) are embedded within the alloys.

2.3.2 Strengthening mechanisms

The reinforcements can strengthen the matrices by 1) changing the stress state of the matrix, or 2) by altering the flow properties of the matrix via changes in its microstructure [20].

1) Load partition: The different stiffness of matrix and reinforcement provoke unequal stress distributions between matrix and reinforcement during loading. The shear-lag model is the most widely used to describe the load transfer in an aligned short fibre composite [21]. It is based on a tensile stress transfer from the matrix to fibre by means of interfacial shear stress (see Fig. 2.8 [20]). The model assumes a radial variation of shear stress in the matrix and at the interface between fibre and matrix. The mathematical treatment is shown, e.g., in [20]. The tensile stress in the fibre is:

$$\sigma_f = E_f \varepsilon_3 [1 - cosh(nz/r_0) sech(ns)] \qquad (2.1)$$

E_f: Young´s modulus of the fibre

ε_3: fibre strain in z axis, direction of applied load

n: dimensionless constant given by $n = \left[\frac{2E_m}{E_f(1+\nu_m)\ln(1/f)}\right]^{1/2}$

E_m: Young´s modulus of the matrix ν_m: Poisson coefficient of the matrix

f: fibre volume fraction L: fibre length

r_0: radius of the fibre s: fibre aspect ratio L/r_0

z: axial distance from the centre of the fibre

The variation of interfacial shear stress along the fibre length gives:

$$\tau_i = n\varepsilon_{3C}/2\, E_f sinh(nz/r_0) sech(ns) \qquad (2.2)$$

where ε_{3C} is the overall composite strain.

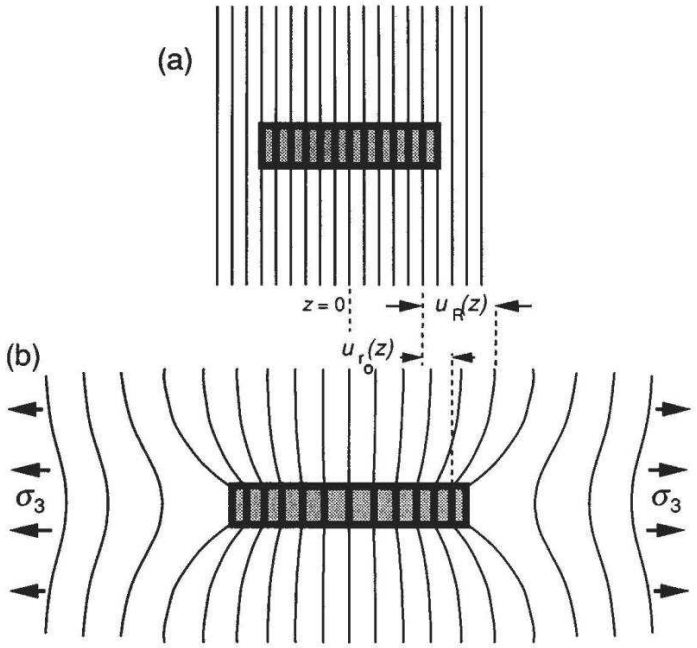

Fig. 2.8. Schematic illustration of the basis of the shear lag model, showing a) the unstressed system, b) the axial displacements, u, introduced on applying tension parallel to the fibre [20].

The main error source of this model lies in the neglected load carrying along the fibre ends. The lower the aspect ratio and smaller fibre/matrix stiffness ratio, the higher the error. The load carrying capacity of low aspect ratio reinforcements increases if this effect is taken into account.

Considering a section of area A normal to the loading direction that intersects the individual fibres at random positions along their length, the applied load is expressed in terms of contributions from the two components as the "***Rule of Averages***":

$$\sigma_3^A = f\bar{\sigma}_f + (1-f)\bar{\sigma}_m \qquad (2.3)$$

where $\bar{\sigma}_f$ and $\bar{\sigma}_m$ are the average fibre and matrix stresses, respectively:

$$\bar{\sigma}_1 = E_f\varepsilon_{3C}[1 - \tanh(ns)/ns] \qquad (2.4)$$

$$\bar{\sigma}_m \approx E_m\varepsilon_{3C}$$

The equilibrium of forces over a fibre length *l/2* (since the fibre is loaded from both ends) leads the following relation:

$$s = \sigma_f/2\tau_{ym} \qquad (2.5)$$

where τ_{ym} is the matrix shear yield strength. It is clear that load transfer is more efficient in composites with large aspect ratio reinforcement, i.e., continuous fibres or whiskers. Particle reinforced materials have a lower reinforcement aspect ratio and the load transfer is not as efficient as in continuous fibres but can still be significant in providing strengthening [22].

With a sufficiently long fibre, it should be possible to load the fibre to its ultimate tensile strength by means of load transfer through the plastically deformed matrix. Fig 2.9 shows different length fibres and their tensile strengths. When the length is smaller than the critical value, i.e., $l<l_c$, the fibre does not achieve its maximum tensile stress. When $l = l_c$, the fibre reaches its maximum tensile stress. If a larger fraction of fibre is required to be loaded, l should be larger than l_c.

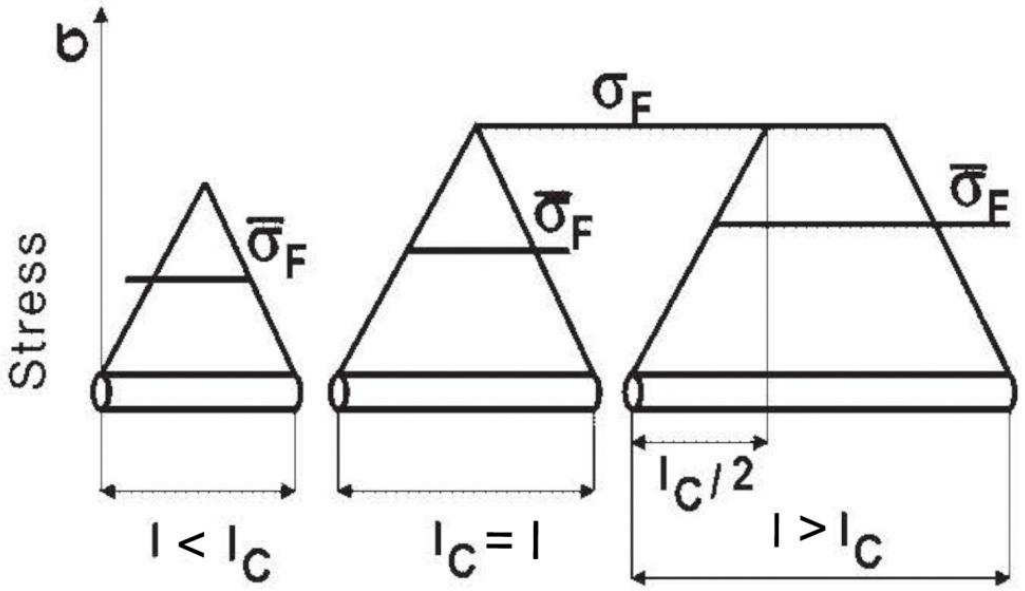

Fig 2.9. Dependence of the effective fibre strength on the fibre length [23].

Considering an elastic loading of an MMC, the averaged stresses in each phase should exhibit, whether they are calculated with the Eshelby model or experimentally, a variation as shown in Fig. 2.10. A decrease in the matrix stress can be observed when compared with the unreinforced matrix because of the load transfer. The beginning of plastification is clear for the unreinforced matrix while the yielding is delayed for the reinforced material.

2) The effect of matrix microstructure:

a. ***Dislocation strengthening***: dislocations can be formed in MMCs either as a result of applied straining or during cooling of MMCs due to local plastification around the reinforcement owing to the thermal mismatch between constituents. Different expressions have been deduced to estimate the dislocation density (ρ) (see , e.g., [24-25]) .The influence of dislocation density on matrix strength $\Delta\sigma_{YM}$ can be estimated using the next expression [26]:

$$\Delta\sigma_{YM} \sim Gb\sqrt{\rho} \qquad (2.6)$$

with

G: shear modulus of the matrix b: Burgers vector

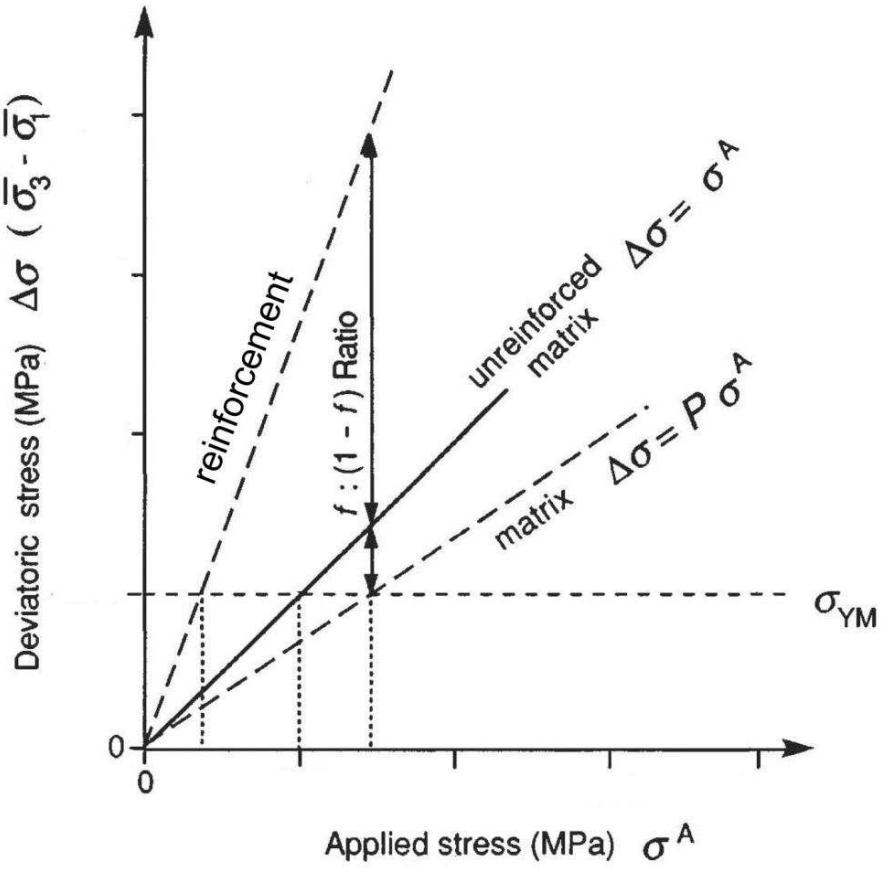

Fig. 2.10. Predicted variation in the average stresses within fibre and matrix for a MMC with effective load partition between matrix and reinforcement [20].

b. ***Strengthening from grain size refinement***: MMCs have typically smaller grain size than their unreinforced matrices. If is assumed that every particle nucleates a simple grain, the contribution to the yield stress of this refinement can be estimated with the Hall-Petch relation [27-28]:

$$\Delta\sigma_{YM} \approx \beta D^{-1/2} \approx \beta d^{-1/2} \left(\frac{1-f}{f}\right)^{1/6} \qquad (2.7)$$

where β is typically 0.1 MPa√m, although it depends on a number of factors [29], D is the grain size, d is the particle size and f represents the fraction of the total volume which is occupied by the reinforcement.

c. ***Orowan and dispersion strengthening***: the reinforcement in MMCs is usually coarse (at least a few μm) and the interparticle spacing large and, therefore, dispersion strengthening is not significant. In age hardenable materials, this mechanism is important since the reinforcement can help in the nucleation and coarsening of precipitates because of the high concentration of dislocations [30].

The strengthening effect produced by ultrafine oxide particles generated during powder metallurgy is also an important mechanism to be considered in MMCs. For instance, in Al powders, the powder particle surface is originally covered by oxide films. During milling or

consolidation, the oxide skin is tore from the Al powders leading to the formation of a new oxide skin. The small oxide particles are thus trapped between cold welded/sintered surfaces. These particles (< 10 nm) increase the strength by Orowan strengthening [31].

2.4 Internal stresses in multiphase materials

Internal stresses are those acting in a material equilibrated with its surroundings. When no external force is acting, they are known as residual stresses [32]. Type I stresses or macrostresses act over a length comparable to the macroscopic dimension of the component (Fig. 2.11). They are a consequence of macroscopic misfit generated during, for example, bending or quenching. Many grains can be involved in these macrostresses, showing a continuous behaviour from grain to grain. Microstresses are divided in type II and III stresses [33]. Type II stresses are localized in a length comparable to the grain size or the reinforcement size and can be a consequence of, e.g., thermal or elastic mismatches between the phases or when phase transformations take place. Discontinuities from grain to grain are observed. Type III microstresses occur in a length scale smaller than grain size, e.g., stress fields around dislocations, precipitates or coherency at interfaces.

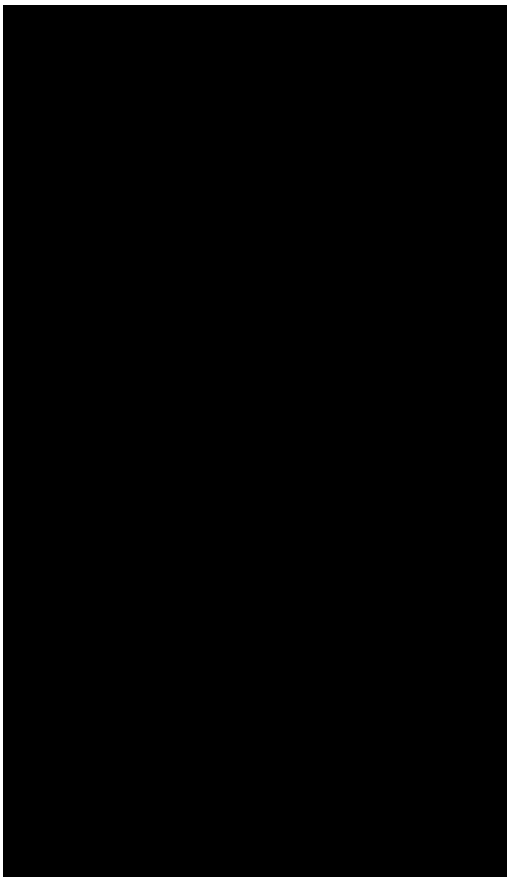

Fig. 2.11. Schematic of possible internal stresses within a material [32].

It is well known that metals generally have larger coefficient of thermal expansion (CTE) than ceramics and intermetallic reinforcements. Since fabrication of MMCs usually involves consolidation at high temperatures or heat treatments, residual stresses arise between phases during cooling to room temperature because of different thermal contractions. If T_{esf} is a temperature in an effectively stress free state, the misfit strain is $\Delta\alpha\ \Delta T$, where $\Delta T = T_{esf} - T_{RT}$ and $\Delta\alpha$ is the difference in thermal expansion coefficient (CTE) between matrix and particle. In the case of an isolate spherical particle, the stress field can be easily obtained by the Eshelby model [34]. Fig. 2.12 a) [20] shows the elastic field caused by cooling 500K an infinite matrix of Ti containing a spherical particle of SiC. A hydrostatic compressive condition is predicted for the particle while a large difference between hoop (tension) and radial (compression) stresses is expected for the Ti matrix. Therefore, a high deviatoric stress can originate the plastic flow of the matrix. Considering a yield stress of 100 MPa for the matrix, both hoop and radial stresses are redistributed (see Fig. 2.12 b)) leading to the plastic flow around the particle and even changing the hoop stresses from tension to compression.

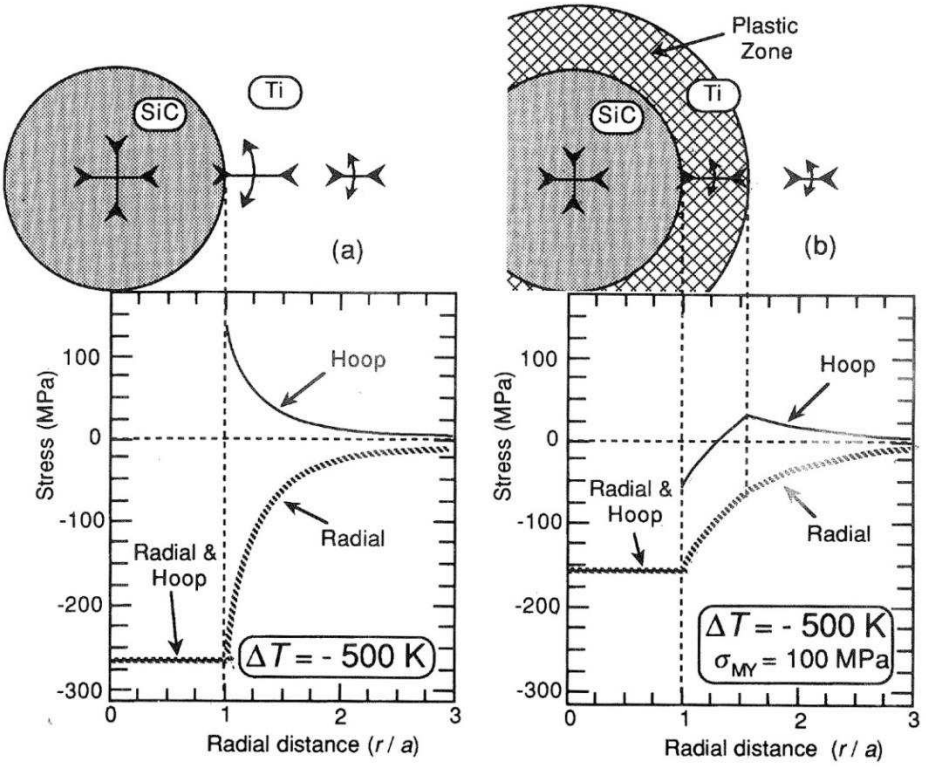

Fig. 2.12. Stress state around a SiC particle in an infinite Ti matrix in a) elastic state b) considering 100 MPa for yielding of the matrix [20].

The expected behaviour of Type II microstresses for an aligned fibre reinforced composite during thermal cycling can be described according to Rabinovitch et al. [35] (Fig. 2.13). The matrix is initially in tension with a stress equal to the yield stress (point A) because

of the cooling during processing. Subsequent heating leads to a decrease of tensile stresses, becoming finally compressive and causing yielding in compression (point B). Plastic flow takes place until the maximum temperature of the cycle is reached (point C). On cooling, compression stresses are reversed into tensile stresses, yielding at a temperature higher than RT (point D). Final cooling leads to the point A, regenerating the initial microstresses. The dilatometry traces are predicted to show hysteresis, but no net dimensional change if the residual stress after the thermal cycle is the same as initial. Transverse stresses were neglected during the thermal cycling.

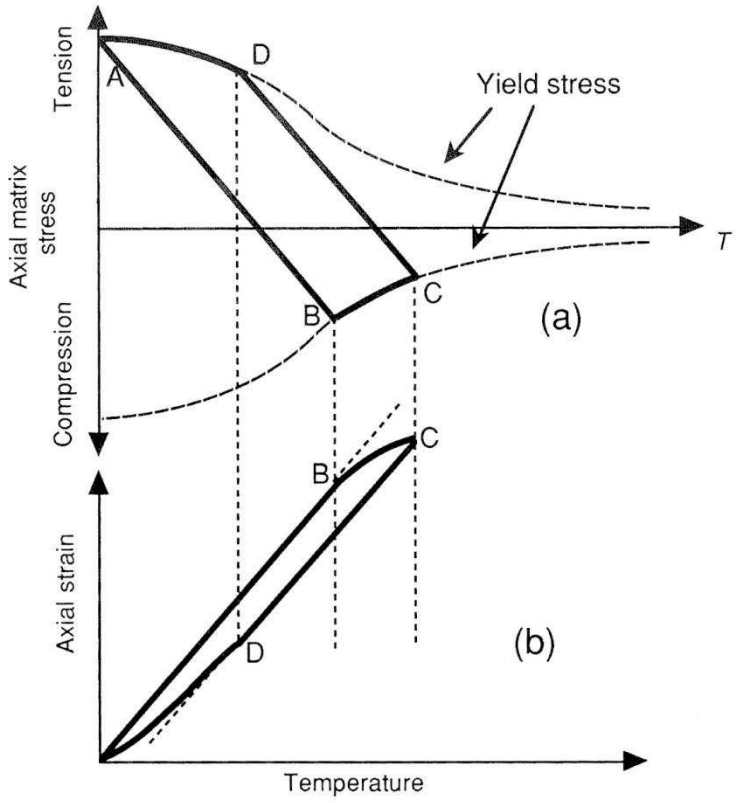

Fig. 2.13. Schematic illustration of the variation in a) matrix stress and b) specimen strain during thermal cycling of an aligned fibre composite [20].

2.5 Creep of MMCs

The high temperature strength and creep resistance of metal matrix composites (MMCs) are determined by the load partition between the phases and/or the presence of insoluble dispersoids distributed within the grains of the matrix [20, 36]. In the case of discontinuously reinforced metals, the load carrying capacity of the reinforcing phase is strongly dependent on its aspect ratio [20, 36]. Thus, the load transfer from the matrix to the

reinforcement is more important for short-fibre reinforced metals than for particle-reinforced metals (PRM), if the same type of reinforcement phase is used, due to the low aspect ratio of the particles (< 3) (see e.g. [12, 37-38]). Furthermore, if the particles are larger than a few micrometres, as it is usually the case in PRM, they cannot act as effective barriers for dislocation glide. In some cases, they can even reduce the creep resistance with respect to the unreinforced matrix [37, 39-43]. On the other hand, the high temperature strength and the creep resistance of PRM can effectively be improved with respect to the unreinforced matrix by the presence of particles in form of dispersoids pinning dislocations [44].

The influence of particle size, particle aspect ratio and processing route on the creep resistance of a 2124 Al-alloy reinforced with 25 vol.% of SiC particles of different sizes was recently reported by Requena et al. [39]. The PRM were produced by powder metallurgy (PM) using different powder blending routes that resulted in different microstructures. The two mixing techniques used were wet blending (WB) and ball milling (BM). The BM PRM exhibited higher creep resistance than the matrix, while the WB route resulted in a decrease of the creep resistance of the PRM with respect to the unreinforced matrix. Moreover, a change in the dominating creep mechanism from viscous drag of dislocations (n = 3) to dislocation climb (n = 5) was observed at ~ 50 MPa for the BM PRM. The n = 5 stress region (> 50 MPa) was characterized by a large apparent creep exponent, which was considered to be due to the presence of a threshold stress σ_{th}. This was rationalized using a creep model developed by Rösler and Arzt [44] and it was interpreted as the stress necessary for the dislocations to undergo a local climbing process over oxide dispersoids introduced during the BM process.

2.6 Synchrotron and Neutron Diffraction for internal stress determination

The major shortcoming of laboratory X-ray diffraction is the low capability of the x-rays to penetrate into the bulk of the material. This leads to alternative complementary techniques as polishing or etching to remove sequentially surface layers allowing the study of the internal stresses below the surface of a material. Corrections must be made to compensate the effect of material removed [32]. Another main limitation is the long acquisition time required. These limitations are overcome by the use of third-generation synchrotron sources and neutron sources (fission and spallation). The high flux of some neutron sources as well as the high brilliance of synchrotron sources allow short acquisition times. Furthermore, neutrons and high energy synchrotron radiation are able to penetrate up to a few cm in structural metals allowing bulk analysis. The gauge volume achievable by synchrotron diffraction is smaller (≤ 1mm^3) than for neutrons (≤ several hundred mm^3) and permits the

study of strain gradients in small regions. On the contrary, the large gauge volume of neutron diffraction can be used, e.g., to avoid the measurement of macrostresses.

Neutron diffraction techniques for strain analysis are divided in two groups:

a) Angle-dispersive neutron diffraction [45]: only used at neutron reactors. A monochromatic beam (i.e. with single wavelength) allows to measure interplanar atomic distances with the θ variation (Fig 2.14 a)). Only a few diffraction peaks can be measured at the same time with this technique (limited by the detector and the material). The atomic distance d of a certain (hkl) plane is calculated as a function of the diffraction angle θ and it is then used to calculate the elastic strain of this plane:

$$d = \frac{\lambda}{2 \cdot \sin\theta} \qquad \varepsilon = \frac{d - d_0}{d_0} = -\cot\theta \cdot (\theta - \theta_0) \quad (2.8)$$

where λ is the wavelength and d_0 and θ_0 are the interplanar distances and diffraction angle of a stress-free reference sample, respectively.

b) Time-of-flight neutron diffraction [46]: the main difference with the angle-dispersive technique is the use of a polychromatic pulsed beam of neutrons generated by a spallation source, where neutrons are produced in pulses containing a continuous spectrum of wavelengths generating a spectra with several diffraction peaks. The time of flight t that the neutrons need to go from their source to the detector is measured. The interplanar distance d and the strain ε for a certain (hkl) plane are calculated as follows:

$$d = \frac{\lambda}{2 \cdot \sin\theta} = \frac{h \cdot t}{2 \cdot m \cdot L \cdot \sin\theta} \qquad \varepsilon = \frac{d - d_0}{d_0} = \frac{t - t_0}{t_0} \quad (2.9)$$

where m is the mass of the neutron, L is the total flight path and t and t_0 are the time of flight of neutrons diffracted by a certain (hkl) plane in the investigated material and in the stress-free reference sample, respectively.

Synchrotron diffraction techniques are also divided in two groups:

a) Angle-dispersive synchrotron diffraction [47]: similar technique to the angle-dispersive neutron diffraction. A monochromatic high energy beam allows to obtain low θ values (< 10°) and the complete Debye-Scherrer rings can be recorded with a 2D planar detector located behind the sample in a transmission geometry mode (see Fig 2.14 b)). Interplanar distance d and strain ε are calculated with

$$d = \frac{\lambda}{2 \cdot \sin\theta} \qquad \varepsilon = \frac{d - d_0}{d_0} = -\cot\theta \cdot (\theta - \theta_0) \quad (2.10)$$

as a function of diffraction angle θ.

b) Energy-dispersive synchrotron diffraction [48-50]: a white beam allows to measure the energy of the diffracted photons and consequently the interplanar atomic distance. Complete diffraction spectra (within the energy range of the polychromatic beam) can be acquired by this technique (see Fig 2.14 c)). The interplanar distance d and the strain ε for a certain (hkl) plane are given by:

$$d = \frac{h \cdot c}{2 \cdot \sin\theta} \cdot \frac{1}{E} \qquad \varepsilon = \frac{d - d_0}{d_0} = \frac{E_0 - E}{E} \qquad (2.11)$$

where h is the Planck´s constant, c is the speed of light and E and E_0 are the energy of the photons diffracted by a certain (hkl) plane of the investigated material and the stress-free reference sample, respectively.

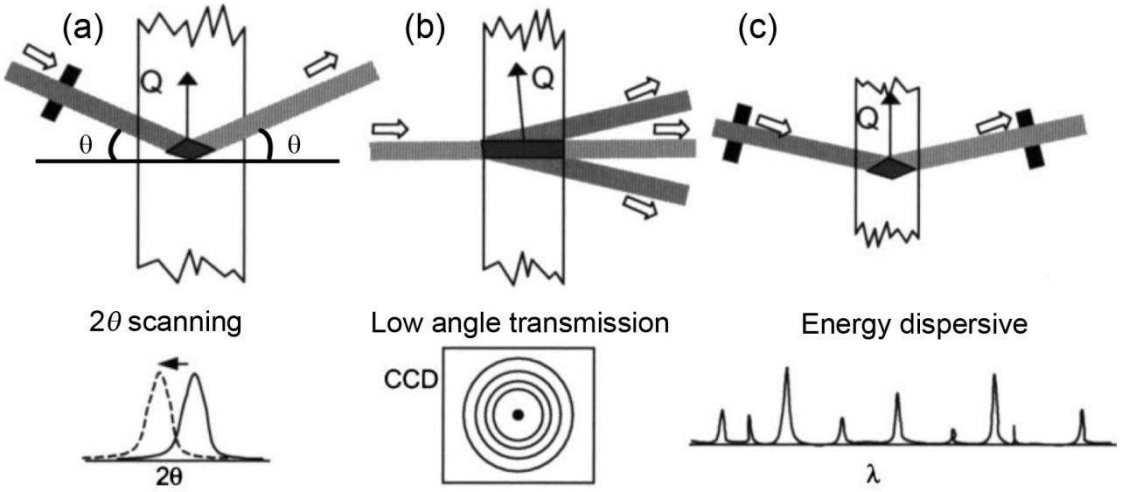

Fig 2.14. Schematic diagrams showing three different strain measurements geometries [51] a) Angle-dispersive neutron diffraction b) Angle-dispersive synchrotron diffraction c) Energy-dispersive synchrotron diffraction.

The choice of one of these techniques depends on four factors:

1) Microstructure of the material: grain size plays an important role since good statistics are required to achieve a representative value of the strain. Gauge volume limitations are ≤ 1 mm^3 for synchrotron measurements and up to several hundred mm^3 for neutron diffraction.
2) Time resolution: depending on the phenomena involved during the experiment, acquisition times of one second or less can be required. For this purpose synchrotron radiation is an ideal tool because of the high brilliance of the third generation sources [52]. Neutron diffraction, even with the highest neutron flux, requires acquisition times of a few minutes.

3) Spatial resolution: when local strains measurements are necessary or for high-resolution strain mapping, the possibility of using a small gauge volume can be an advantage [53].
4) Type of stresses: gauge volume size similar to the studied sample results in equilibrated macrostresses and only microstresses are measured. On the contrary, a gauge volume smaller than the sample size provokes superimposed effects of macrostresses and microstresses. This is useful when, for instance, a macrostress profile is required.

2.7 Motivation of the work

2.7.1 Load partition in multiphase lightweight metals at high temperature

A first review of internal stresses using neutron diffraction in metal matrix composites was given by Withers [54] in 1995. At this time, the third generation synchrotron sources became available to general users. Since then, several studies have been carried out to determine the internal stresses in heterogeneous lightweight metals, mostly MMCs under different load and thermal conditions. An overview of relevant works published since 1995 dealing with this topic and was reported by Requena et al. [55], where facility, material, d_0, acquisition time, year, remarks on experimental procedure and main results are indicated. Main conclusions that can be drawn from previous works are:

1. Publication number based on neutron measurements is still larger than for synchrotron simply because the third generation synchrotron sources became available later. Nevertheless, works with synchrotron diffraction have increased significantly during last years.

2. Heat-treated monolithic unreinforced matrices and matrix powders are the most common choice for d_0 stress-free reference. When these methods do not work, other methods, independent of the d_0, have been proposed [56-57].

3. There is a lack of works dealing with in situ experiments since the high flux and short acquisition time required to follow time-dependent processes can not be provided by many facilities in the world. During synchrotron diffraction measurements, achieved acquisition times can be ≤ 1 s, while for neutron diffraction are a few minutes.

There is still a significant lack of in situ high temperature experiments aiming at studying and complementing load partition analysis in:

- Previous works carried out at RT.

- High temperature tests analyzed either macroscopically or from the materials' internal architecture point of view.

The analysis of the load partition between the Al matrix and eutectic Si is an attractive problem in near eutectic cast AlSi alloys that has been studied at RT [12]. The 3D structure of eutectic Si in the as cast condition can be substantially modified by solution treatment, disintegrating the Si networks into individual rounded and elongated particles with a lower load carrying capability [12]. Similar analysis at high temperature is still a pending task.

Al_2O_3 short fibres can be used to improve the strength of near eutectic cast AlSi alloys [58-63]. Since the production method of these composites raises the costs, the introduction of rigid aluminides instead of ceramic short fibres is an alternative solution. Particularly, Ni and Cu aluminides introduce phases able to carry load, becoming interesting for aluminium piston alloys because of their stability at high temperature. Recent works [64-67] propose that the main strengthening mechanism of Al-Si piston alloys at high temperature is given by the load carrying capability of the hybrid 3D interpenetrating multiphase networks of Si and aluminides. Furthermore, the disintegration and spheroidization during solution treatment of the eutectic 3D network of Si is highly supressed by the presence of these aluminides. The quantification of the load transfer from the Al matrix to the hybrid 3D structures of rigid phases during loading at high temperature by means of in situ bulk diffraction methods can be used to verify the hypothesis given in [64-67].

Particle reinforced aluminium alloys have been extensively studied in terms of high temperature strength and creep [68-70] but comparison of different processing routes has received less attention. Wet blending and ball milling are two blending routes used in powder metallurgy that generate different microstructures and consequently different mechanical responses. The creep resistance of PM Al-alloys reinforced with SiC particles blent by wet blending and ball milling was studied in [39, 87]. The load partition between the Al matrix and the reinforcement as well as the influence of oxide dispersoids during thermal cycling complement the previous work comparing the effects of both processing microstructures on creep resistance.

Poletti et al. [71-72] characterized Ti662 alloys produced by powder metallurgy and ingot metallurgy in terms of compression behavior at high temperatures. Moreover, these works showed that ceramic TiC particles can improve the strength of the alloys even at high temperatures [72]. This strengthening was mainly attributed to the diffusion of interstitial C from the TiC particle into the α-phase. The load partition between α- and β-phases in Ti alloys at RT has been reported in some works (for α, α+β and β alloys) [73-77]. A further step

is the study of this load partition at high temperatures. The load transfer study will complement and clarify previous works.

2.7.2 Microstructure evolution in Ti-based alloys at high temperature

The analysis of the Debye-Scherrer rings can be a powerful tool to study the evolution of the microstructure during deformation of metals [78]. Since the short acquisition times of the synchrotron can be below 1 s, it is possible to follow and describe, in some cases, physical mechanisms (e.g., dynamic recovery, dynamic recrystallization, grain rotation, subgrain formation) during in situ tests. Some of the main representative results for different metals, including α- and β-phase in TiAl alloys are presented in [78]. The α-phase showed grain rotation during high temperature compressive deformation of TiAl alloys, while the β-phase suffered subgrain formation. Dynamic recovery was also observed during the in situ experiment. The in situ comparison of microstructure evolution for unreinforced and reinforced Ti662 alloys is still a pending task which complements the load partition study.

2.8 Hypothesis

Problem 1:

The creep resistance and internal stresses generated during thermal cycling of Powder metallurgy particle reinforced aluminium alloys is affected by the particles blending route.

Hypothesis: The presence of sub-μm oxide dispersoids generated during powder blending determines the load carrying capacity and stress relaxation behaviour at high temperatures. Neutron diffraction can be used to study this hypothesis and correlate microstructure, especially particle size, with high temperature strength.

Problem 2:

Load partition during compression tests of Al-based alloys at high temperature. An AlSi12 and aluminium piston alloys, undergoing different solution treatments are compared with their respective as cast conditions. The presence of the aluminides in the aluminium piston alloy modifies the load born by the Si.

Hypotheses:

- In AlSi12, 3D interconnected Si network disintegrates with ST. The load carrying capability of Si decreases compared with the as cast condition.

- In aluminium piston alloys, Ni and Cu aluminides prevent the 3D disintegration of the Si network and build themselves interconnected structures. The connectivity of the eutectic Si and aluminides is not lost during solution treatment, resulting in similar stresses carried by the 3D rigid structures.

Synchrotron diffraction is the appropriate diffraction tool to follow in situ the strains in Si because the short acquisition rates achieved by this bulk diffraction technique. Si strains are correlated with the internal architecture of the alloys after different solution treatments.

Problem 3:

The high temperature strength of the Ti662 alloys is affected by their processing route and the presence of TiC particles. Simultaneously to the strain study, the microstructural evolution can be correlated in situ with the macroscopic stress-strain curve and the internal microstructure to determine plastic deformation mechanisms.

Hypotheses:

α- and β-phases may deform plastically with different mechanisms. Furthermore, these phases bear different load portions depending on the metallurgy process and the presence of TiC particles. Synchrotron diffraction is the selected tool to evaluate the load partition and correlate the results with their internal architecture. Identically to the Al alloys, short acquisition times of ~ 1 s are required.

3 Experimental

3.1 Unreinforced lightweight alloys

Two unreinforced Al alloys and one unreinforced Ti alloy were studied during the development of this work. Their chemical compositions, processing routes, thermal treatments and microstructures are detailed below.

3.1.1 AlSi12 alloy

An AlSi12 alloy was produced by squeeze casting at Leichtmetallkompetenzzentrum Ranshofen (Austria) [79] and delivered in step blocks with 33 cm of height and 11 cm of width (Fig. 3.1). Step thickness ranged from 15 mm at the bottom to 2 mm in the upper part. The chemical composition is shown in Table 3.1 [64].

Alloy	Si	Ni	Fe	Mn	Al
AlSi12	11.17	0.006	0.07	<0.001	Bal.

Table 3.1. Chemical composition of the AlSi12 alloy (wt.%) [64].

Sections 1 and 2 of the step block showed identical microstructures in previous studies [80] and are namely investigated during the in situ compression tests. The alloy was studied in as cast (AC) condition and after solution treatments (ST) at 500°C during 1 h and 4 h. All the samples were artificially overaged during 100 h at 300°C with subsequent air cooling in order to stabilize the Si precipitates.

The conventional metallography steps applied to different AlSi12 samples are detailed in [80]. Fig. 3.2 shows light optical micrographs (LOM) of the AlSi12 alloy in different conditions, i.e., AC, 1 h and 4 h ST. The Si in the AC condition exhibits a highly interconnected 3-D lamellar structure [12] although they are seen as needles in the micrograph (Fig. 3.2 a)). The Al matrix encloses the eutectic structure of lamellar Si. The different ST times result in loss of the interconnectivity, showing isolated and rounded Si particles with the Al matrix surrounding the eutectic Si (Fig. 3.2 b) and c)). These particles are similar to short-fibre-like structures [12].

3.1.2 Aluminium piston alloy

An AlSi10Cu6Ni2 piston alloy (see Fig. 3.3), hereafter 1062, was fabricated in the form of pistons by Kolbenschmidt [81] by gravity die casting [1]. Its chemical composition is shown in Table 3.2.

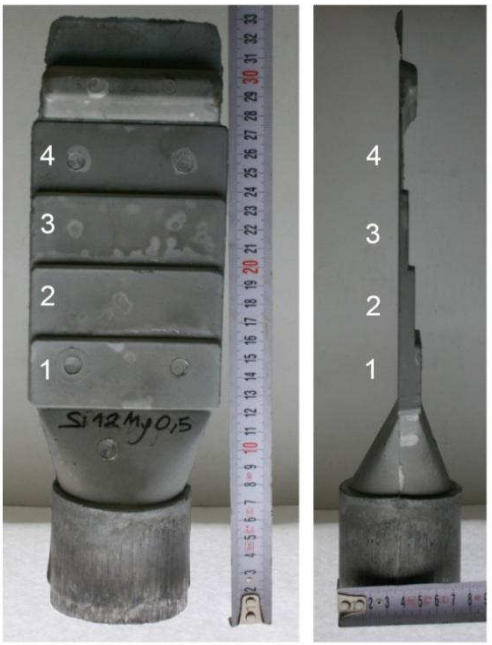

Fig. 3.1. AlSi12 step block produced by squeeze casting. Steps 1 and 2 correspond to the regions investigated.

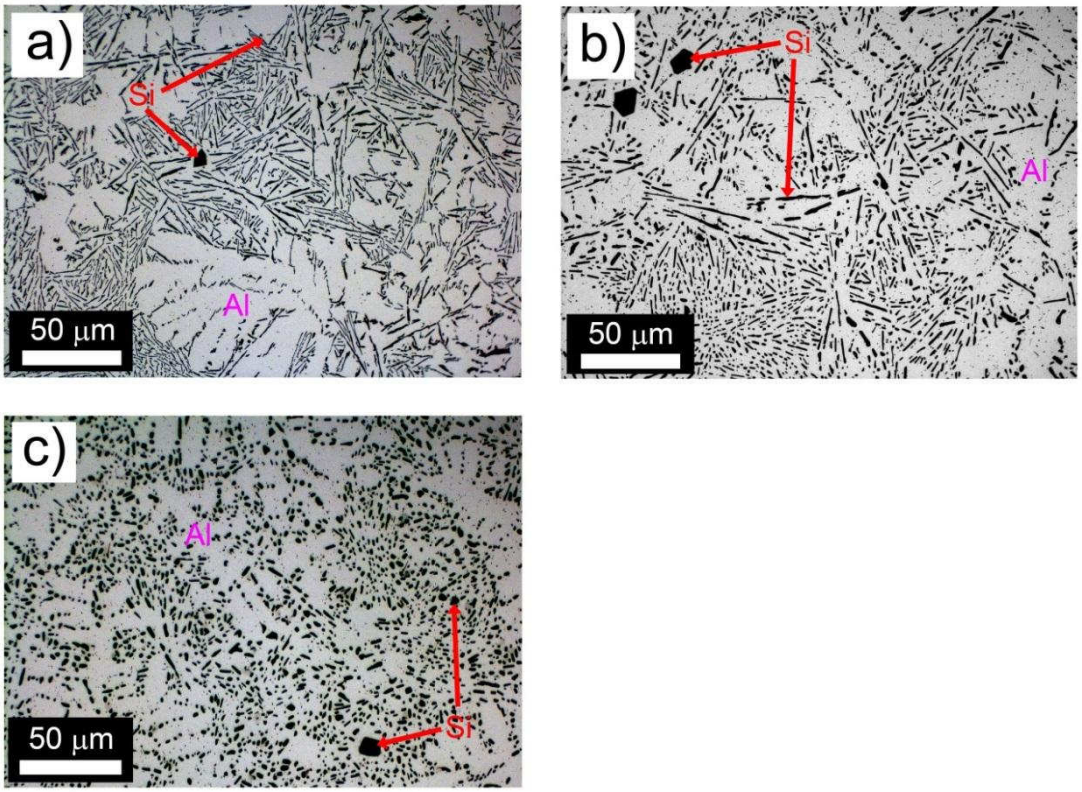

Fig. 3.2. LOM of the AlSi12 alloy showing the eutectic Si, primary Si in a) AC condition, b) 1 h ST and c) 4 h ST.

Alloy	Si	Fe	Cu	Mn	Mg	Ni
1062	11.44	0.34	5.31	0.22	0.25	1.88

Table 3.2. Chemical composition of the 1062 alloy (wt.%).

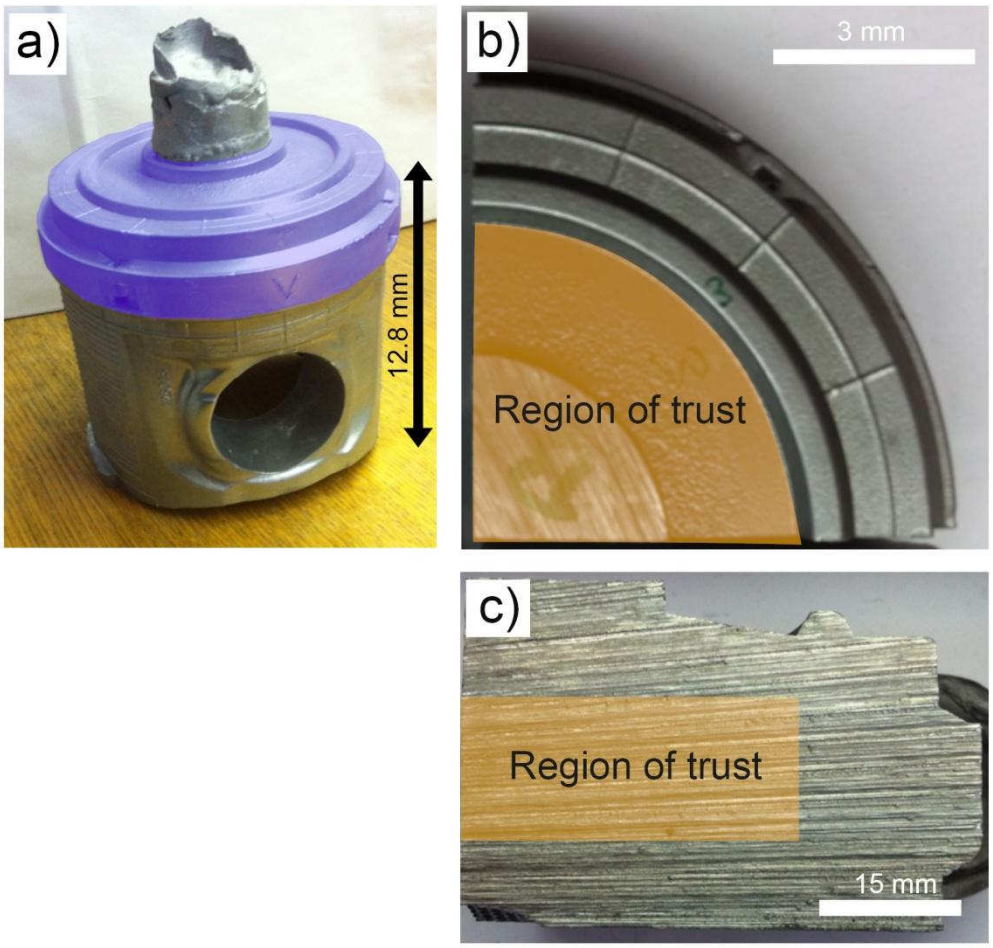

Fig. 3.3. a) General view of the 1062 piston alloy. The Initial investigated volume is painted in violet, b) and c) are the zenithal and frontal view of a quarter of the piston. The region of trust is indicated in orange.

A previous investigation [82], comparing microstructures and hardness from different regions of the upper part (violet volume in Fig. 3.3 a)), revealed a region of trust, indicated in Fig. 3.3 b) and c), where microstructure and mechanical properties are homogeneous. Therefore, samples were taken from this region. In addition to the AC condition, ST of 1 h and 4 h at 500 °C were carried out with subsequent overageing (included the AC condition) at 300°C during 100 h to stabilize precipitates. The samples were cooled down in air. Fig. 3.4 a), b) and c) show light optical micrographs corresponding to the AC, 1 h and 4 h ST conditions, respectively. α-Al, primary and eutectic Si and different aluminides with irregular shape can be identified. Contiguity between Si and the different aluminides can be observed for all conditions. The AC platelet-like structure of Si is seen as needles in the 2D micrographs. The Si and the aluminides form a 3D network embedded in the α-Al matrix [67]. The ST provokes a slight spheroidization of the highly interconnected Si-aluminides 3-D structure, where platelet-like structures and coarse primary Si (Fig. 3.4 a)) become more rounded (Fig. 3.4 b)

and c)). The interconnectivity and the morphology of the 3-D structure during ST are highly preserved.

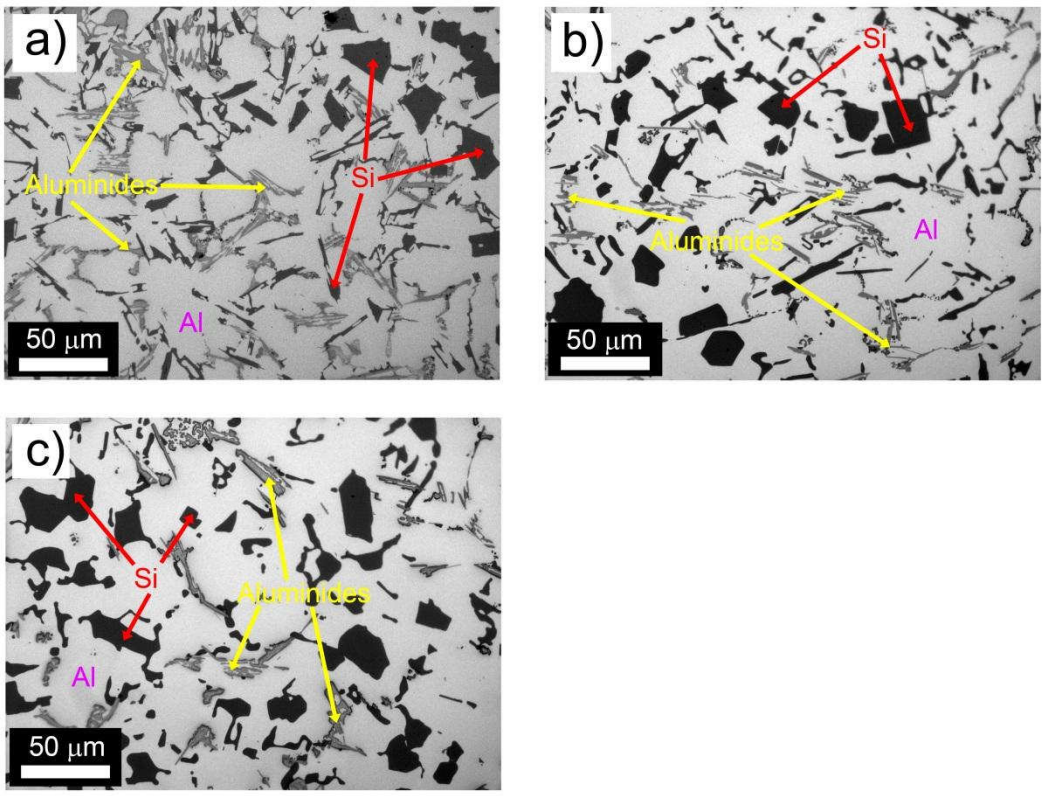

Fig. 3.4. Light optical micrographs of the 1062 piston alloy showing the eutectic Si, primary Si and aluminides in a) AC condition , b) 1 h ST and c) 4 h ST.

3.1.3 Unreinforced Titanium alloy

A Ti-6Al-6V-2Sn alloy (Ti662 hereafter) [71, 83] produced by two different processing routes was investigated:

- Powder metallurgy (PM) with a Dynamet (Cold-Hot Isostatic Pressing) method [83]. The processing steps include:
  1) Blending of powders and ceramic particles in case of composites.
  2) Cold Isostatic Pressing (CIP): the mixed powers are pressed at room temperature using a hydrostatic pressure vessel, obtaining a "green" preform.
  3) Sintering: the "green preform" is transferred into a vacuum furnace with controlled heating and cooling rates.
  4) Hot Isostatic Pressing (HIP): the closing of small pores produce full density and improves mechanical properties of the material.
- Ingot metallurgy (IM) with subsequent cogging (forging) at temperatures just below the beta transus temperature (< 945°C) with the purpose of breaking the cast

structure to obtain a fine-grained wrought billet according to the AMS 4979 specification, summarized in [83].

A schematic transversal sample cut from the billet to observe the microstructure in the IM Ti alloy is shown in Fig. 3.5. Cogging and hot compression directions are indicated together with the observed metallographic surface. SEM (scanning electron microscope) micrographs were acquired to study the microstructure at the beginning of the high temperature tensile tests for both processing routes. For this purpose, samples with length of 10 mm and square section of 4 mm were subjected to isothermal heat treatments at 650°C and 750°C during 30 min in argon atmosphere to avoid oxidation. The same holding times were used during the in situ synchrotron experiments before the tensile tests started. A subsequent quenching in water was carried out to freeze the microstructures. Resulting microstructures for the different temperatures and processing routes can be seen in Fig. 3.6. The Ti662 PM alloy consists of randomly oriented α-lamellae embedded in prior β-grains [71] (see Fig. 3.6 a) and b)). The α-lamellae are thinner at 750°C, increasing the fraction of β-phase. On the other hand, the Ti662 IM (Fig. 3.6 c) and d)) is characterized by primary α-chains oriented in the cogging direction (pre-forging process) showing a globular structure surrounded by a fine β-grain structure [71] (see Fig. 3.5). At 650°C the distribution of secondary α-needles within the β-phase can also be observed. Most of the α-needles are dissolved at 750°C (Fig. 3.6 e) and f)). The β-transus temperature is 945°C [71] and the β volume fraction at different temperatures, taken from the equilibrium phase diagram, is ~ 30 vol.% at 650°C and ~ 35 vol.% at 750°C [3].

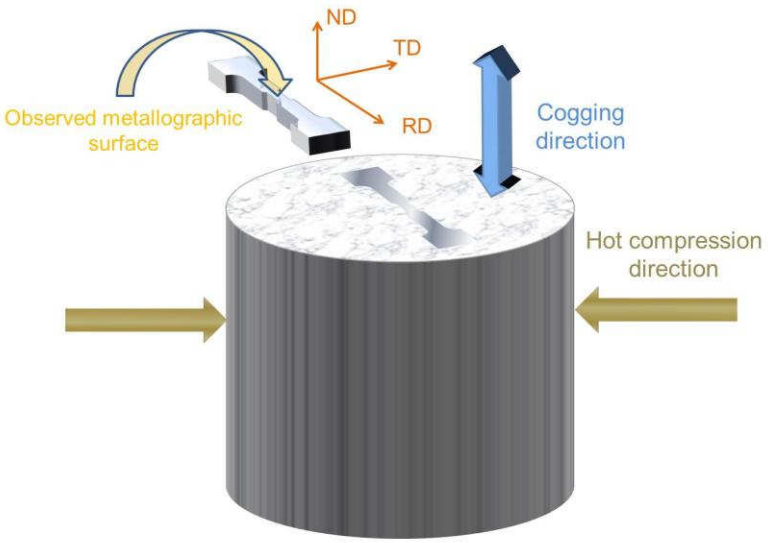

Fig. 3.5. Transversal sample cut selected to observe the microstructure and for the in situ diffraction experiments during tensile deformation. Directions of cogging and hot compression are also indicated.

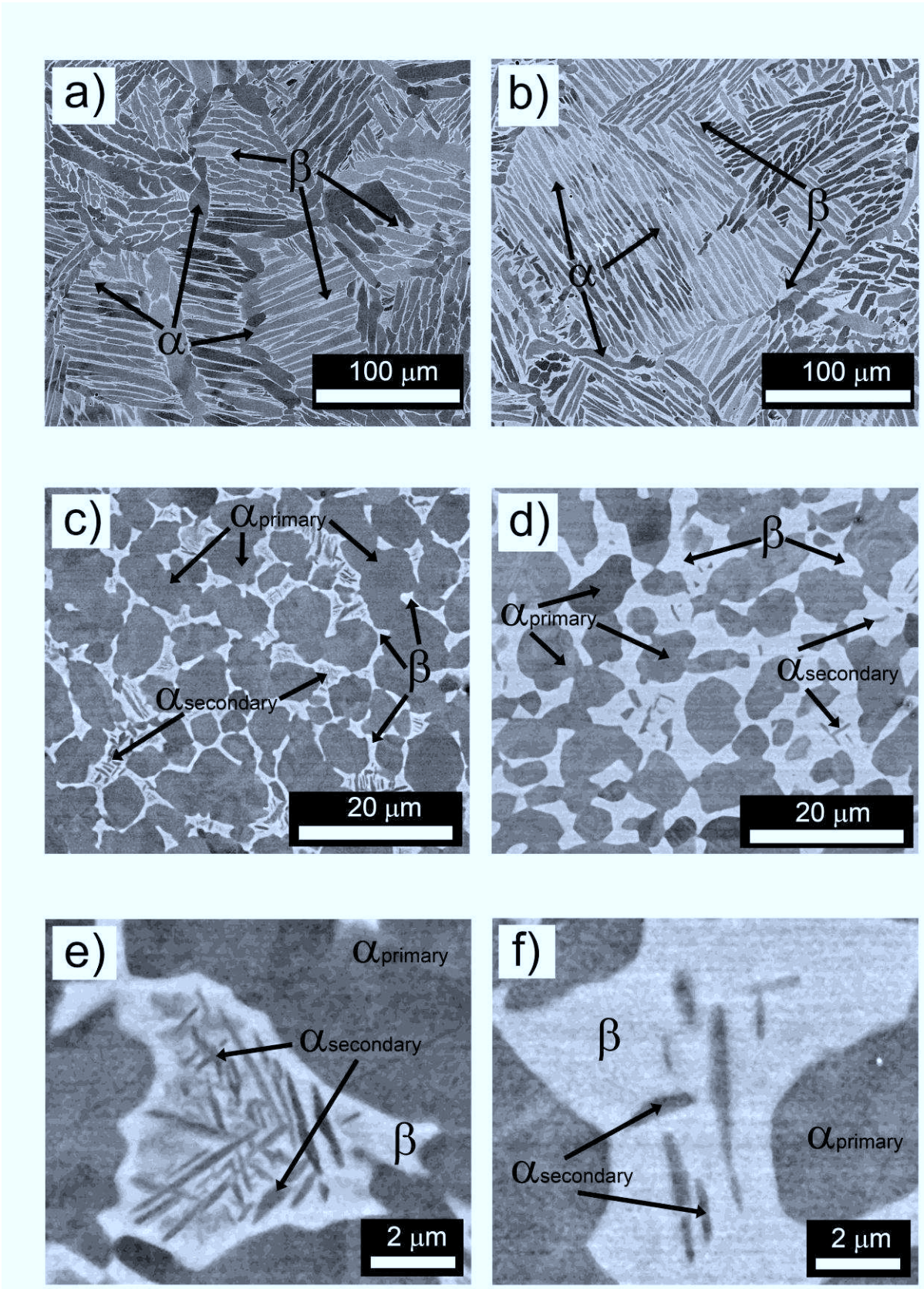

Fig. 3.6. SEM micrographs of the frozen microstructures: a) Ti662 PM at 650°C, b) Ti662 PM at 750°C, c) Ti662 IM at 650°C, d) Ti662 IM at 750°C, e) detail of α-secondary in Ti662 IM at 650°C, f) detail of α-secondary in Ti662 IM at 750°C.

3.2 Particle Reinforced Lightweight Alloys

3.2.1 Particle reinforced aluminium alloys

An AW6061 Al-Alloy (AlMg1SiCu) and an AW2124 Al-alloy (AlCu4Mg) reinforced with 25 vol% of SiC particles were produced at CENIM, Madrid [84]. The former was produced by one PM route and the latter by two PM routes (explained below). The 2124 and 6061 powders, with particle sizes < 75 µm, were provided by Alpoco [85], while the SiC powders were provided by ESK [86]. SiC powders < 20 µm with an initial particle size distribution as indicated in [39, 87] were used. The SiC particles are irregular in shape and sharp edged.

The blending of the powders was carried out using two different routes:

a) Wet blending: this is a low energy blending technique in which the powders were mixed within liquid cyclohexane (C_6H_{12}) for 24 h. After blending, the cyclohexane was evaporated and the powders were dried.

b) Ball milling: a planetary milling device with a ratio of steel-balls-to-material of 7:1 without process agent control was used to blend the powders with a speed of 200 rpm for 4 h. Unreinforced matrix powders were also mixed using this technique.

After blending, the powders of all the materials were cold compacted in an Al tube for subsequent hot extrusion at 450 °C. A die with a diameter of 11.8 mm was used achieving a deformation ratio (billet/bar) of 14:1. Extruded bars of the 2124 powder without being subjected to ball milling were also produced.

All the materials were solution treated at 495 °C for 20 min with subsequent water quenching and overaging at 300 °C for 2 h to stabilize precipitates (T7 condition).

Hereafter, the materials will be called 2124, 6061, BM 2124, BM 2124/SiC/25p/<20µm, WB 2124/SiC/25p/<20µm and WB 6061/SiC/25p/<25 µm.

A thorough microstructural analysis of the investigated materials was presented in [39, 87]. The microstructural differences between the WB and BM PRM can be seen in the light optical micrographs (LOM) in Fig. 3.7. The WB 2124 (Fig. 3.7 a) and b)) and WB 6061 composites (Fig. 3.7 e) and f)) present a monomodal SiC particle size distribution. On the other hand, the SiC particles are fractured during BM resulting in the presence of sub-µm SiC particles leading to a bimodal particle size distribution (Fig. 3.7 c) and d)). The detailed statistical analysis of the particle size distribution that demonstrates their monomodal and bimodal nature for the WB and BM composites, respectively, can be found in [87], while these are summarized in [39] for the 2124 composites.

The SiC particles in WB PRMs maintain their sharp edges, whereas those of the BM PRMs are more rounded. The BM PRM exhibits some particle-free zones elongated in the direction of extrusion, which result from particle-free matrix grains deformed in the hot extrusion process.

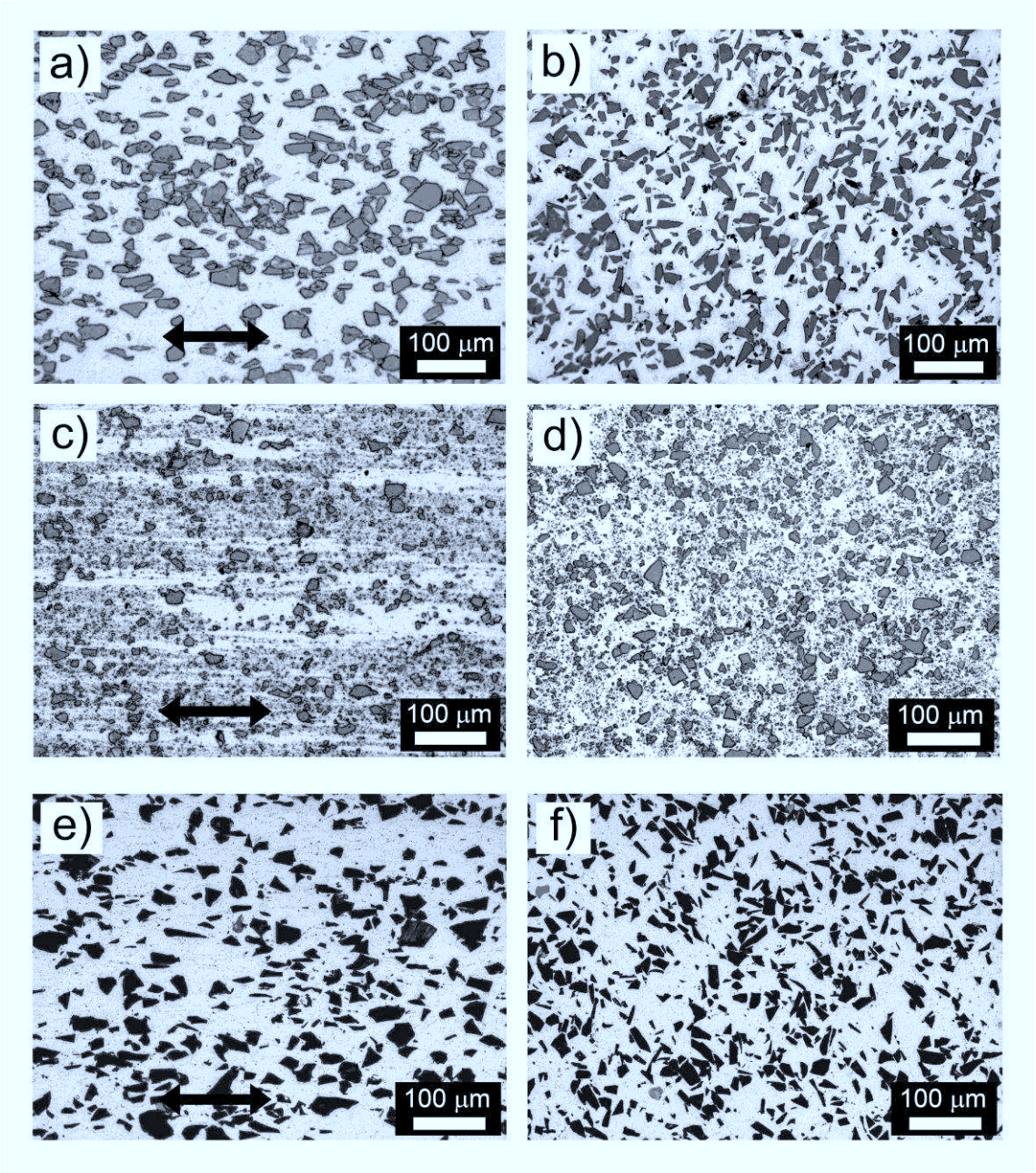

Fig. 3.7. LOM of the microstructure of a) WB 2124/SiC/25p/<20µm, plane parallel to the extrusion direction, b) WB 2124/SiC/25p/<20µm, plane perpendicular to the extrusion direction, c) BM 2124/SiC/25p/<20µm, plane parallel to the extrusion direction, d) BM 2124/SiC/25p/<20µm, plane perpendicular to the extrusion direction, e) WB 6061/SiC/25p/<20µm, plane parallel to the extrusion direction, WB 6061/SiC/25p/<20µm, plane perpendicular to the extrusion direction. The arrows mark the extrusion direction.

3.2.2 Particle reinforced titanium alloys

A Ti662 alloy reinforced with two different volume fractions of TiC particles, i.e. 12 vol.% and 20 vol.%, was produced. Hereafter, these materials will be called Ti662/TiC/12p and Ti662/TiC/20p. The materials were produced by PM by the Dynamet method (see 3.1.3) [83].

SEM micrographs of the composites are shown in Fig. 3.8 with different magnifications. The internal structure reveals the presence of α-lamellae (dark grey) embedded in prior β-grains (light grey). α-lamellae are smaller than in the Ti662 matrix (Fig. 3.6 a) and b)). TiC particles are non-homogeneously distributed and agglomerate decorating the original Ti alloy powder grains. Furthermore, some pores (black) can be distinguished, in a larger concentration for the alloy with 20 vol.% reinforcement. These pores are located within the clusters of the TiC particles.

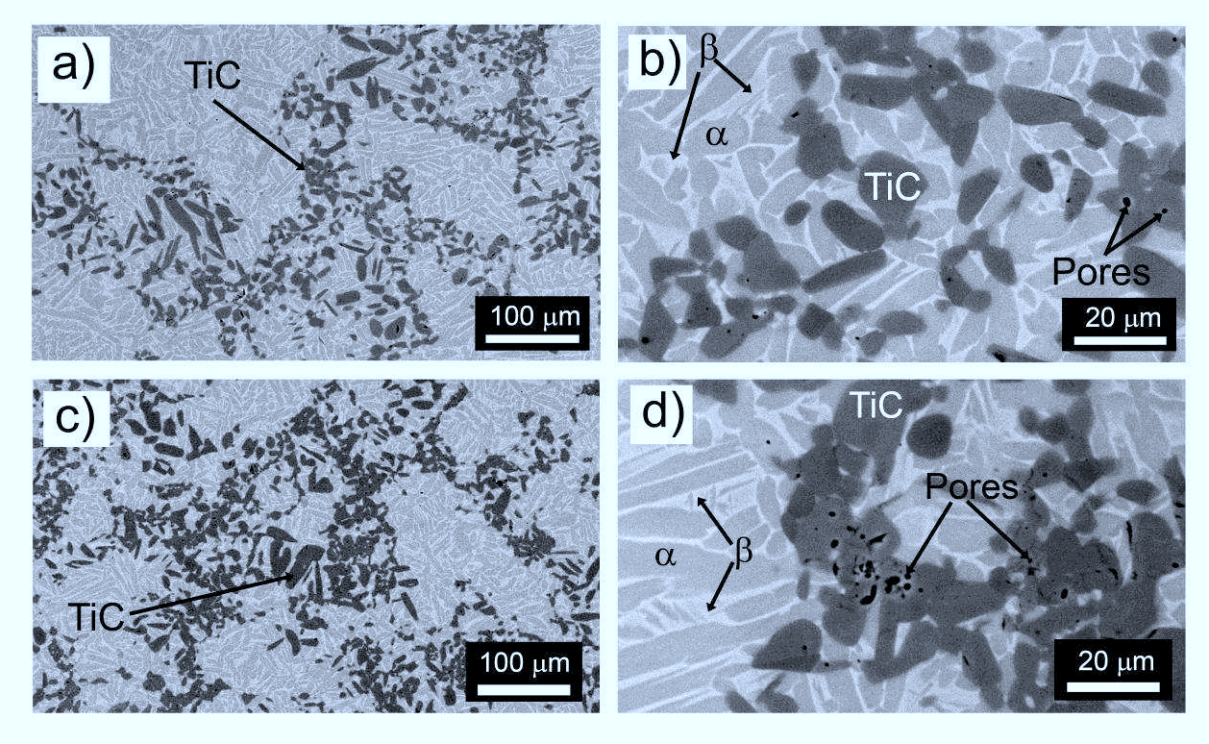

Fig. 3.8. SEM images with different magnifications of a) and b) Ti662PM/TiC/12p and c) and d) Ti662PM/TiC/20p. α-lamellae and the β-phase can be seen. Colonies of TiC particles with pores within the cluster can also be distinguished. TiC particles decorate the original Ti alloy powder grains.

3.3 Diffraction experiments

3.3.1 Neutron Diffraction

In situ neutron diffraction experiments were carried out for the particle reinforced Al-alloys at the neutron beamline STRESS-SPEC [88] of the reactor source of the

Forschungs–Neutronenquelle Heinz Maier-Leibnitz (FRM II) in Garching, Germany, using a Mirrotron MK-300-1 - Gas mixture 3 bar ^{3}He + 2 bar CF_4 area detector. A wavelength λ = 1.67 Å was used to acquire simultaneously the (311) and the (202) diffraction peaks of Al and SiC, respectively. The distance between these two reflections is between ~ 6.6° and ~ 7.3° (depending on the temperature) and, therefore, the area detector was positioned so that its centre was at 2θ = 82.5° with a 2θ range of approximately 10°, i.e. 82.5° ± 5°. A general setup of the experiment can be seen in Fig. 3.9 where the principal parameters for in situ neutron diffraction are indicated.

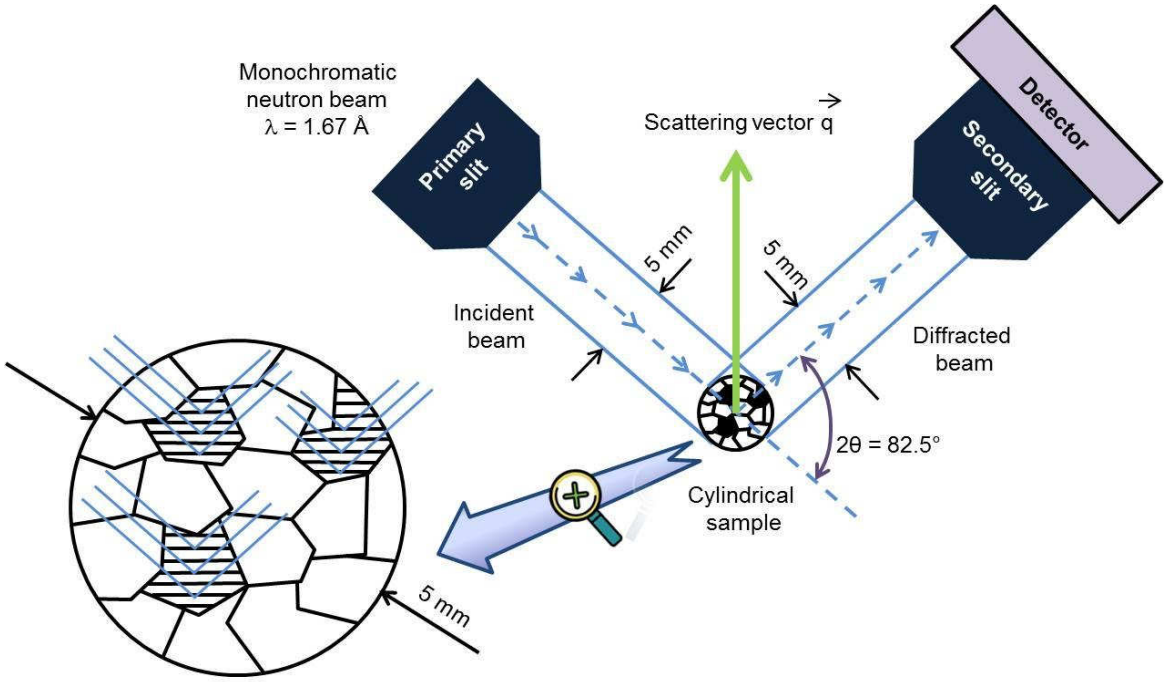

Fig. 3.9. Schematic view of the experimental setup used to carry out the in situ neutron diffraction experiments. The gauge volume contained the whole sample.

The Al-particle reinforced materials were mounted inside the lamp furnace shown in Fig. 3.10 and subjected to the temperature profile shown schematically in Fig. 3.11. The heating rate was about 1 K/s, while the cooling rate was about 0.5 K/s. The black squares show the temperatures at which diffraction measurements were carried out. The acquisition time was 200 s per point. Isothermal treatments of 35 min for the 2124 WB and 30 min for the 2124 BM and the 6061 WB were carried out at 230 ºC in the third temperature cycle to evaluate the time dependence of eventual stress relaxation at this temperature. Volume averaged thermally induced strains were measured in the directions longitudinal and orthogonal to the extrusion direction using two cylindrical samples machined by spark erosion with a length of 5 mm and a diameter of 5 mm and with the length axis oriented in the directions parallel and normal to extrusion, respectively, as shown in Fig. 3.12. A gauge volume of approximately 5 × 5 × 5 mm^3, containing the whole sample, was defined by

primary and secondary slits. The use of a gauge volume that covers the whole sample (see Fig. 3.9) was necessary to avoid the measurement of macro-stresses. A gauge volume slightly larger than that of the sample leads to a shift of the diffraction peaks (see e.g. [89]). To minimize this problem all the samples were positioned in the centre of the beam before starting the thermal cycling experiments. This was done scanning each sample moving them stepwise perpendicular and parallel to the beam direction. The position of each sample was then chosen as that for which the intensity of the diffraction peaks was the highest.

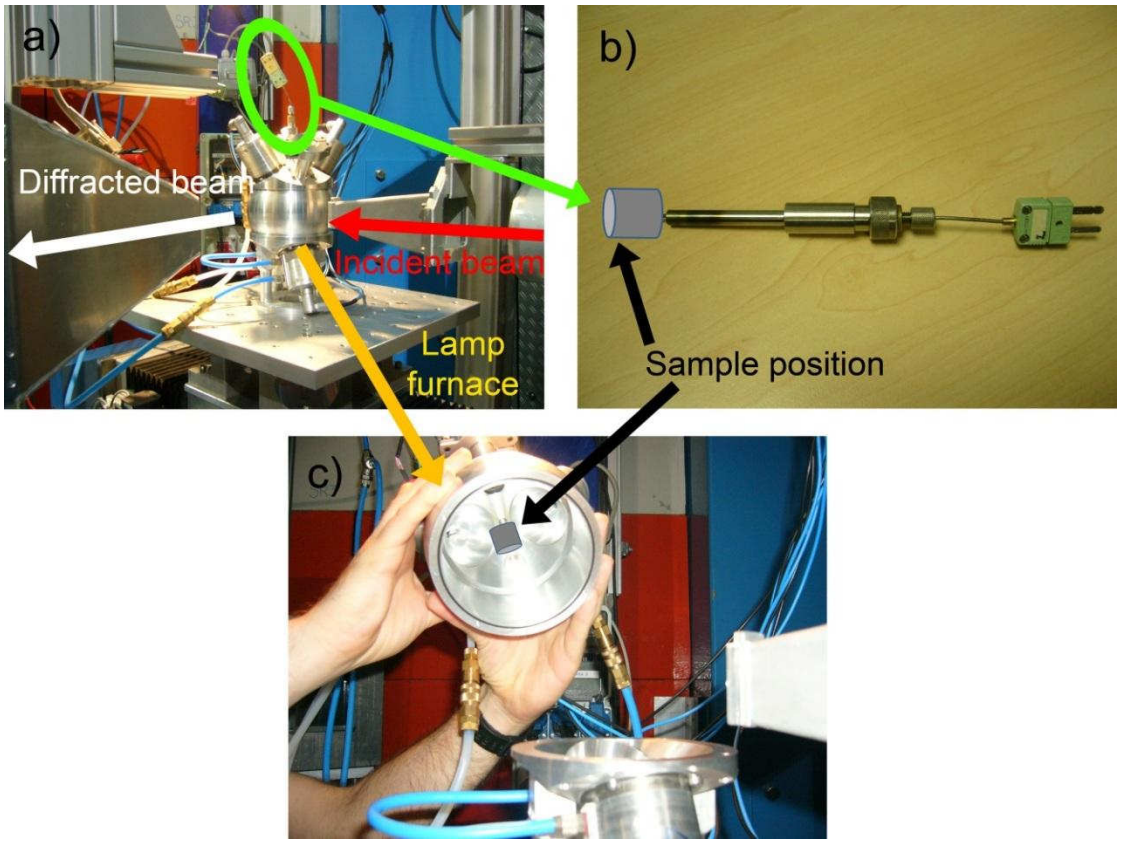

Fig. 3.10. a) Experimental setup at STRESS-SPEC beamline at FRM II. In b) and c) the lamp furnace and the internal location of the sample are indicated.

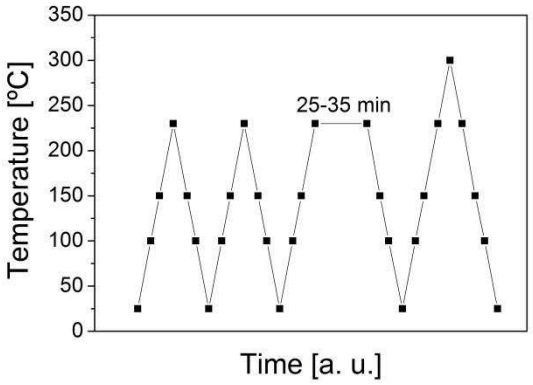

Fig. 3.11. Thermal cycling applied to the WB and BM PRM, showing the different temperatures at which diffraction measurements were carried out (black squares).

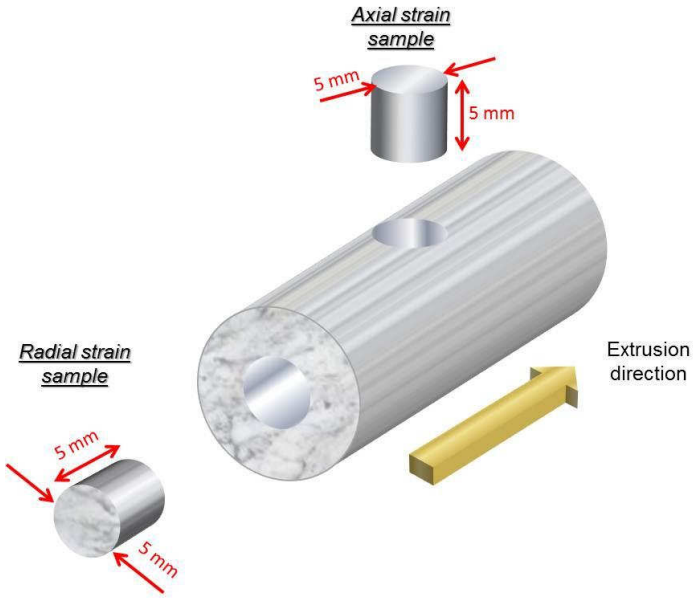

Fig. 3.12. Samples of the PM materials machined by spark erosion with length and diameter of 5 mm and axis oriented parallel (axial) and orthogonal (radial) to the extrusion direction, respectively.

3.3.2 Synchrotron Diffraction

In situ tensile tests

The in situ high energy angle dispersive X-ray diffraction studies were performed in transmission geometry. Volume averaged thermal and elastic strains were measured. The simultaneous acquisition of different Debye-Scherrer rings for the same phase allowed the study of crystallographic anisotropies.

Tensile tests during diffraction of Ti662 IM, Ti662PM, Ti662/TiC/12p and Ti662/TiC/20p were carried out at the ID15B beamline of the European Synchrotron Radiation Facilities (ESRF), Grenoble, France [90]. A monochromatic beam with E = 87.5 KeV (λ = 0.14175 Å) and primary slits of 0.3 × 0.3 mm^2 allowed acquisition times of 0.7 sec/frame with a gauge volume of 0.3 × 0.3 × 1.5 mm^3 located within the bulk of the sample. Debye-Scherrer rings corresponding to the crystallographic planes of the different phases were collected in a two-dimensional image plate Pixium detector with dimensions of 2640 (h) x 1920 (v) pixels and pixel size of 154 x 154 μm^2. A sample-detector distance of 1043 mm was used and LaB6 powders in a capillary were used for position and instrumental broadening calibration. The ESRF supplied a screw driven Instron electro-thermomechanical tester (ETMT) [78, 91] for the tensile tests. The load was applied in steps so that the tensile test was not a continuous process and stress relaxation between loading steps was expected because of the high temperatures. The strain rate was 0.001 s^{-1} and the temperatures selected for the tensile tests were 650, 750°C and 850°C. Prior to the beginning of the tensile tests, the samples were held during 30 min at the selected temperature in order to relax possible macro

and micro residual stresses generated during the heating and to stabilize the microstructure. The heating was performed by DC passing through the sample, controlling the temperature with a type R thermocouple. The Ti samples with central cross section of 1.5 × 2 mm^2 (see Fig. 3.13 a)) were protected by argon atmosphere to avoid oxidation. The short central sample gauge length (5 mm) hindered the use of extensometers. Therefore, the stiffness of the machine is involved in the macrostrain although it is assumed to play a small role and the strain in the centre of the sample is considered equivalent to the global sample strain. A schematic view of the experimental setup at the ESRF is shown in Fig. 3.14. Fig. 3.15 shows a detailed schematic view of the incident and diffracted beams. The beam covers the total thickness of the sample, i.e., 1.5 mm. The beam was positioned at the centre of the sample below the thermocouple. The experimental setup is shown in Fig. 3.16, while a detail of the chamber with the sample mounted can be seen in Fig. 3.17.

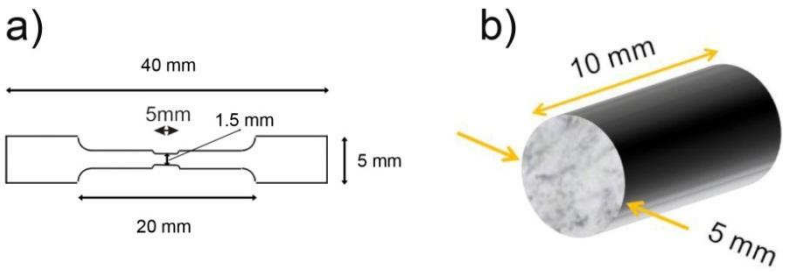

Fig. 3.13. Schematic view of a) the modified "dogbone" sample geometry for the tensile tests of the Ti-based materials and b) cylindrical sample geometry for compression tests of the cast Al alloys.

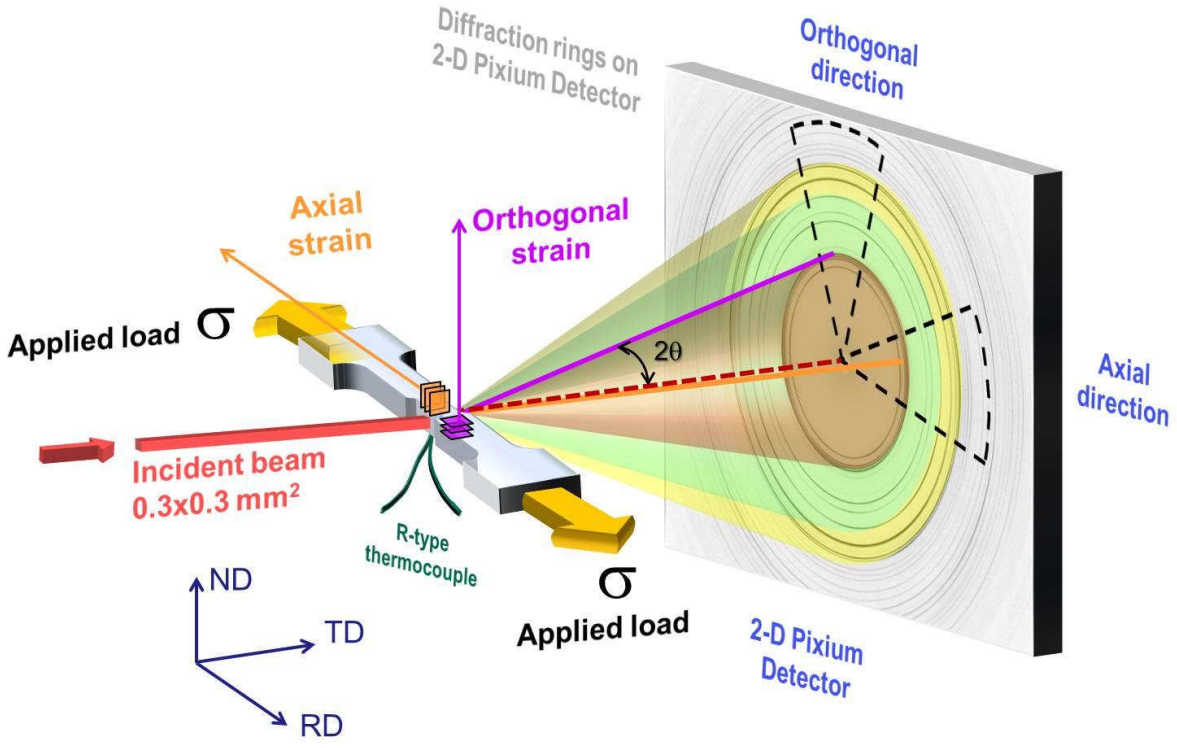

Fig. 3.14. Schematic view of the experimental setup at the ESRF.

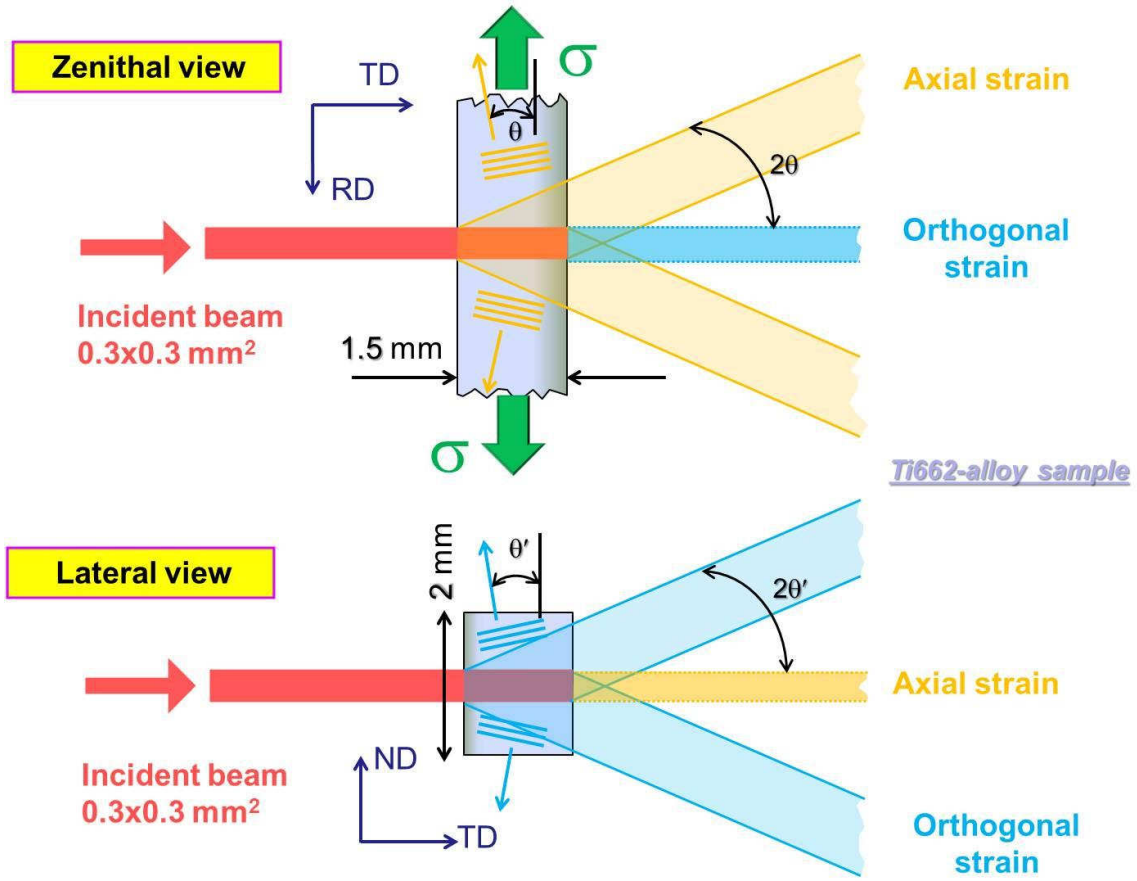

Fig. 3.15. Schematic zenithal and lateral views of the in situ synchrotron diffraction experiments at ID15B at the ESRF.

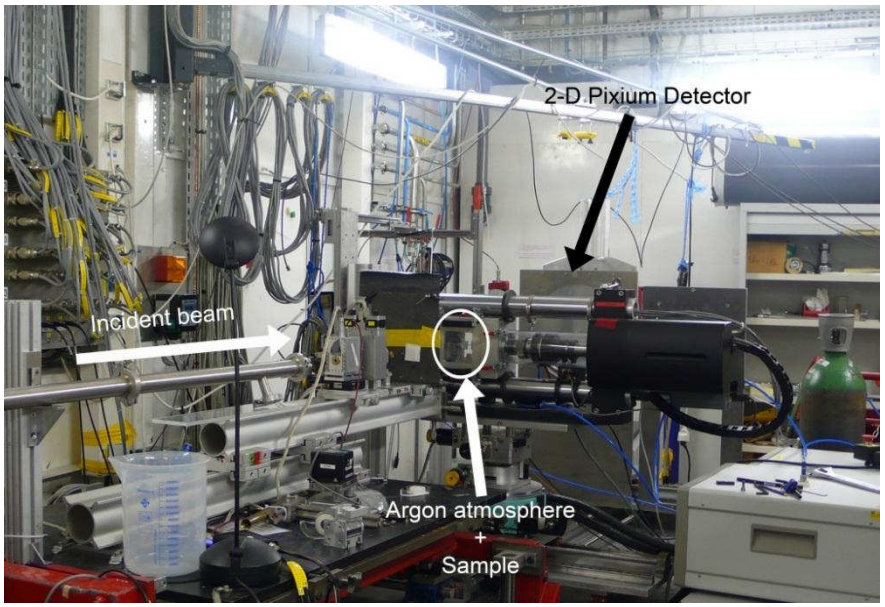

Fig. 3.16. Experimental setup at ID15B at the ESRF.

In situ compression tests

The AlSi12 and 1062 alloys were subjected to compression tests at the GKSS Engineering Materials Science Beamline Harwi-II [92-93] at DESY, Hamburg. The monochromatic beam supplied E = 100 keV, i.e., λ = 0.12407 Å with aperture slits

of 1 × 1 mm^2. The acquisition time was set up to 4 s/frame and the images were collected in a 2-D mar555 flat panel detector, with 2560 and 3072 pixels in the horizontal and vertical directions, respectively, and pixel size 139 × 139 μm^2 (see Fig. 3.18). The sample-detector distance was set to 1534 mm and a capillary of LaB_6 powders was used to calibrate the sample-detector distance and instrumental broadening. Cylindrical samples with length of 10 mm and diameter of 5 mm were cut by spark erosion (Fig. 3.13 b)). A schematic view of the general setup can be seen in Fig. 3.19. Fig. 3.20 shows the zenithal and lateral views of the previous figure. The experimental setup can be observed in Fig. 3.21. The beam was located at 3.5 mm from one side of the sample and in the centre of axial axis of the sample, giving rise to a gauge volume of ~ 1 × 1 × 5 mm^3. The samples were compressed with a Bähr dilatometer DIL 805 (see Fig. 3.21 and Fig. 3.22) with an induction heating system. The heating rate of 300 K/min and the temperatures were monitored by a type K thermocouple. The samples were compressed right after reaching the test temperature with a strain rate of 0.001 s^{-1}. The compression temperature was 300°C for both the AlSi12 and 1062 alloys.

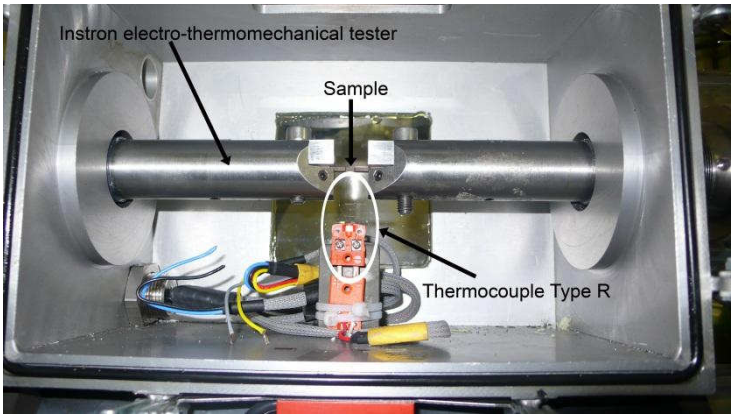

Fig. 3.17. Detail of the experimental setup at ID15B at the ESRF.

Fig. 3.18. Picture of the 2-D mar555 detector used at Harwi-II. A beam stop to avoid detector damage owing the high brilliance of the beam can be seen.

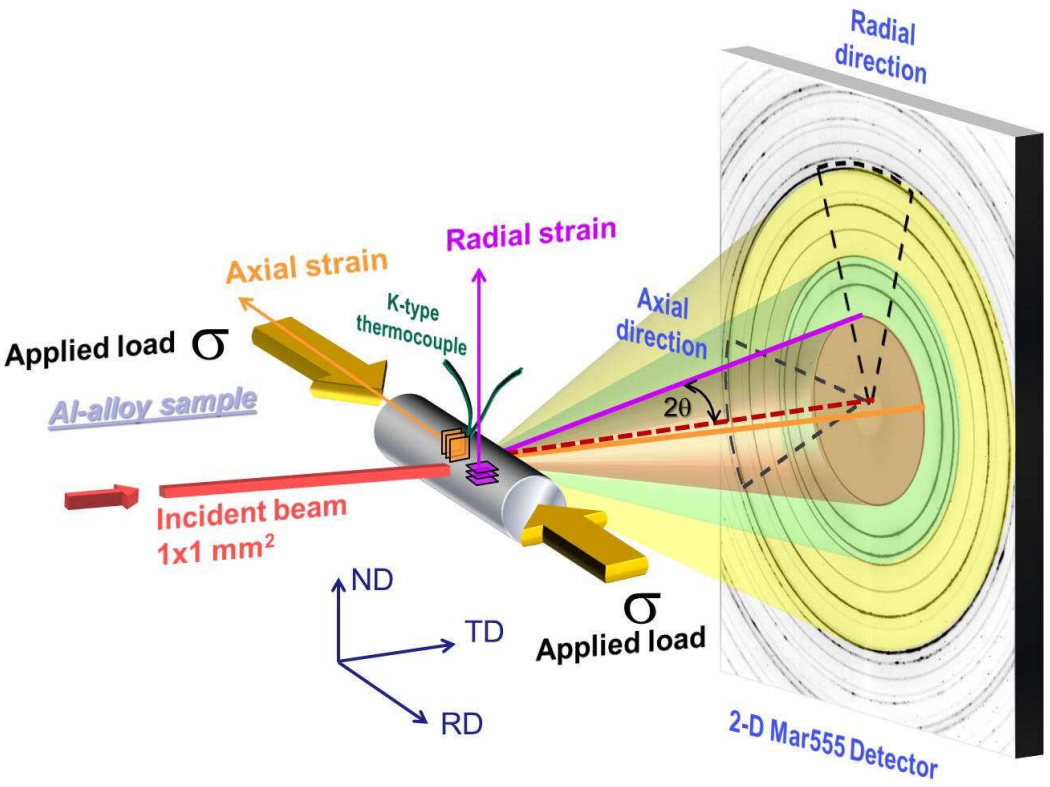

Fig. 3.19. Schematic view of the experimental setup at Harwi-II.

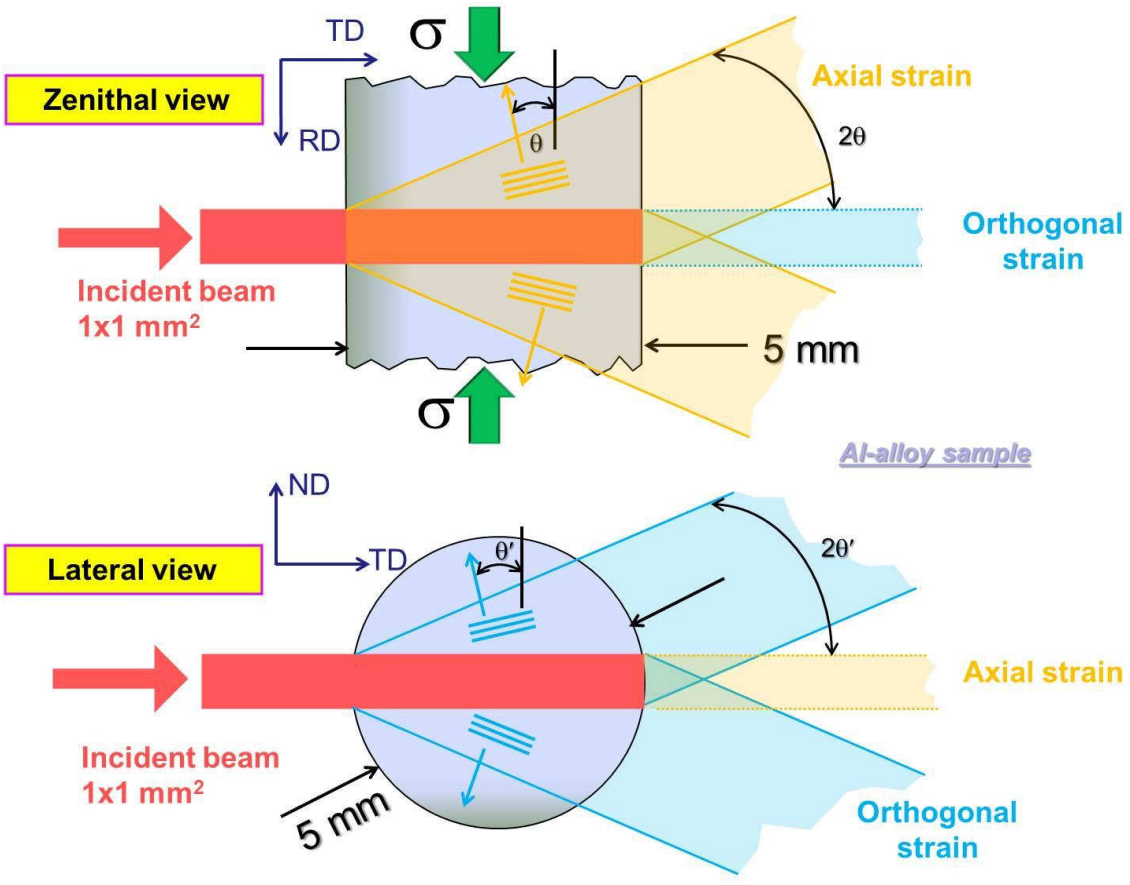

Fig. 3.20. Zenithal and lateral views of the setup at Harwi-II.

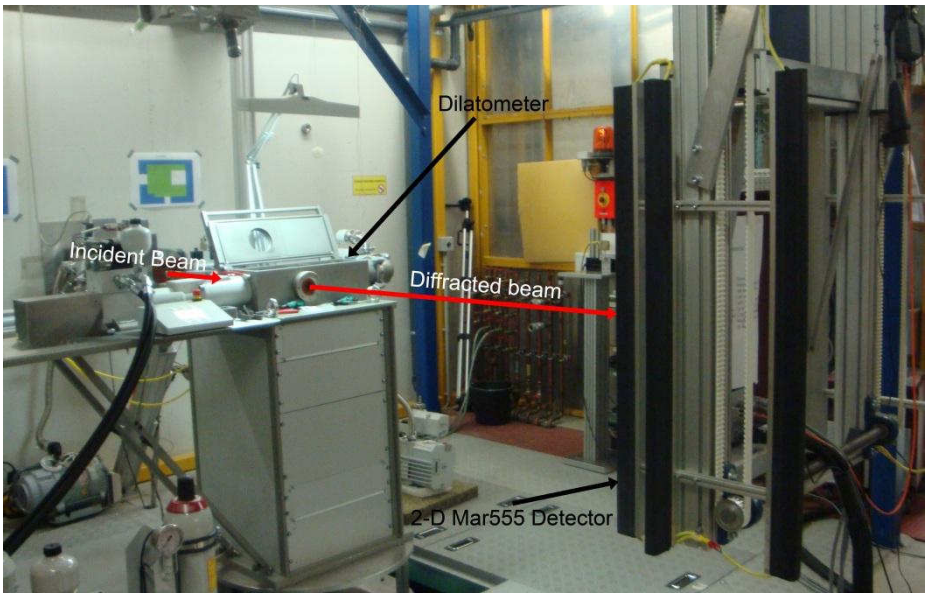

Fig. 3.21. Experimental setup at Harwi-II at DESY.

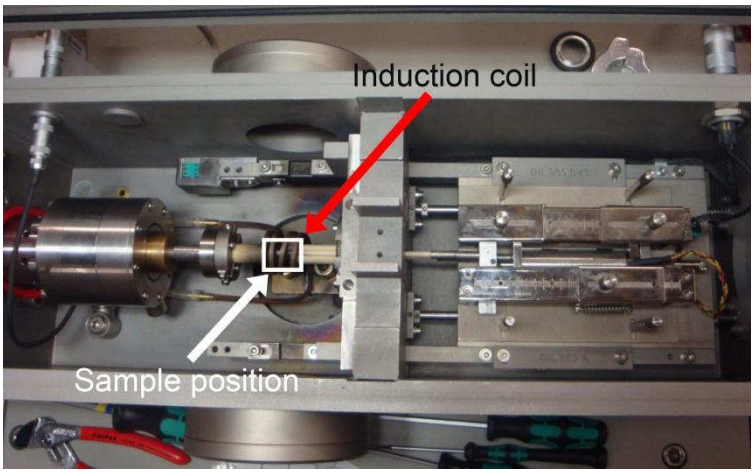

Fig. 3.22. Detail of the experimental setup at Harwi-II. The chamber of the Bähr Dilatometer with the induction coil can be observed. The sample is located inside the coil.

3.4 Strain and Stress calculation

3.4.1 Diffractograms

A typical neutron diffraction image of Al-PRMs can be seen in Fig. 3.23 a) where the Al and SiC Debye-Scherrer rings are identified. The software StressTex-Calculator [94] was used to integrate the images and the obtained neutron diffractograms were fitted with a simple Gaussian function for the peaks and a 3rd degree polynomial for the background. A typical diffractogram is showed in Fig. 3.23 b).

The 2-D images acquired during the synchrotron diffraction experiments were integrated using the software Fit2D [95]. Sectors of 10° and their symmetric were selected for the Ti-based materials for the axial and orthogonal directions. This angle is the minimum angle to obtain a high peak-to-background intensity ratio in the diffractogram. The diffraction

peaks were fitted with a simple Voigtian function. Images corresponding to the unreinforced and reinforced Ti alloys are shown in Fig. 3.24 a) and b), respectively, where crystallographic planes of α-Ti, β-Ti and TiC are identified together with the circular sectors corresponding to the axial and orthogonal directions. Characteristic diffractograms integrated with Fit2D are shown in Fig. 3.25. The investigated 2θ range was ~ [3° - 7.3°].

Characteristic 2-D diffraction images for the AlSi12 and 1062 cast Al alloys are shown in Fig. 3.26 a) and b), respectively, while diffractograms integrated are presented in Fig. 3.27. The right side of the detector was disregarded due to the low quality of the diffracted signal on this portion because of the line broadening originated by the monochromator on this side together with large pixel size of the detector. The methodology to process the diffractograms was similar to that described for the Ti alloys although only the region between 82.5° and 277.5° is considered and the selected sectors for strain determination have 15°. Integrated sectors for axial and radial direction are colored over the Debye-Scherrer rings in Fig. 3.26. The α-Al matrix, Si and Al_7Cu_4Ni and Al_2Cu phases are identified (the intermetallic phases are only present in the 1062 alloy). The investigated 2θ range was ~ [1.5° - 6°].

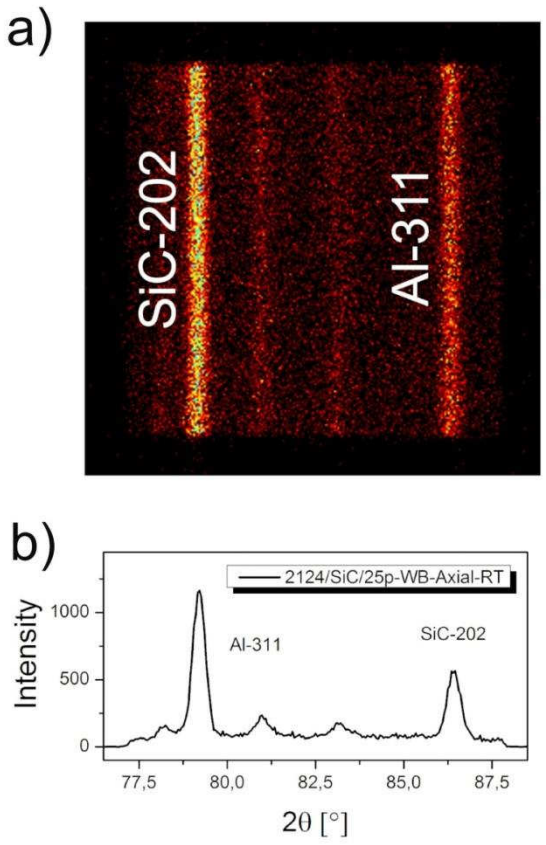

Fig. 3.23. a) Section of the Debye-Scherrer rings acquired during the in situ neutron diffraction experiments, b) diffractogram obtained by integration for 2124/SiC/25p WB in axial direction at RT.

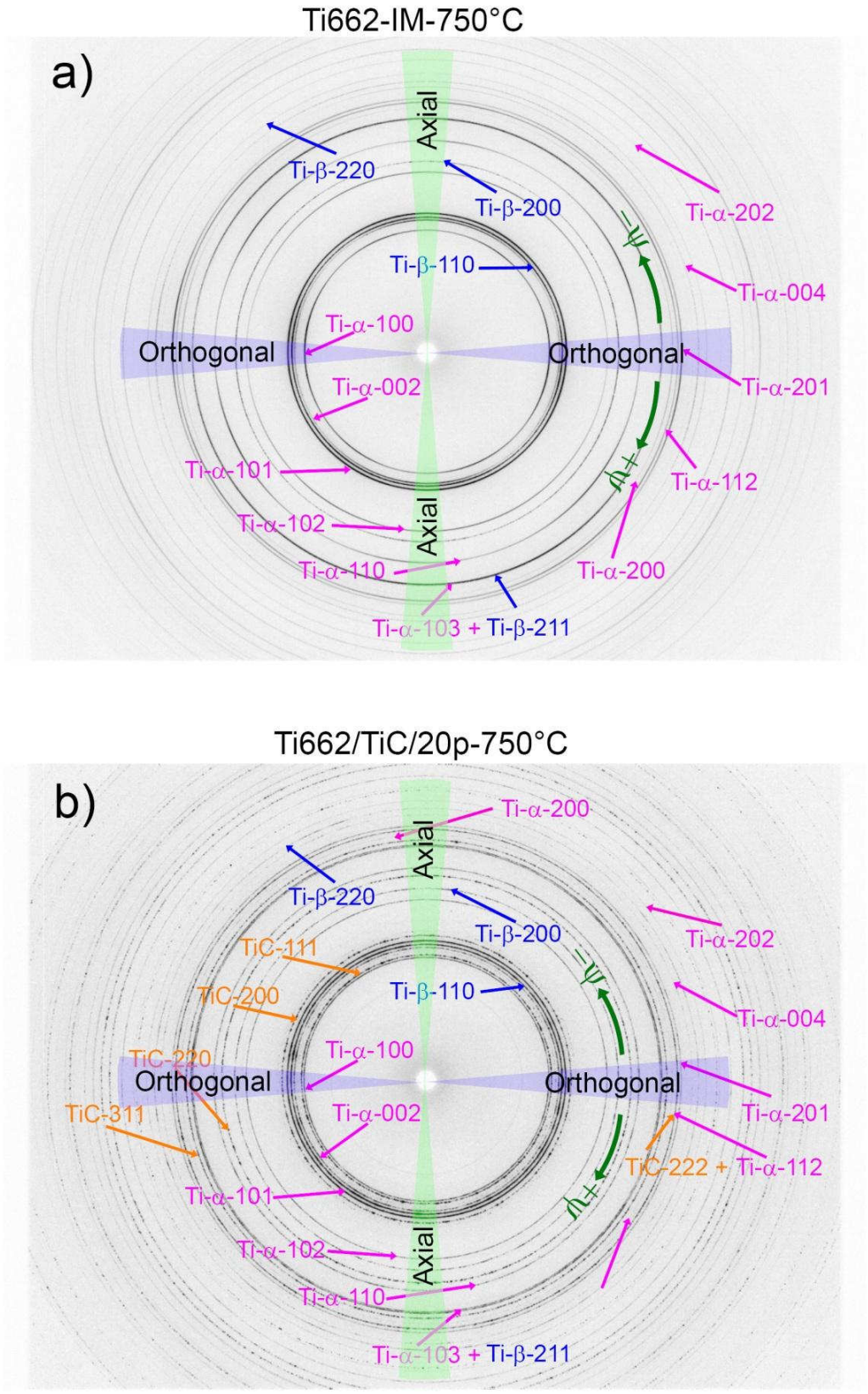

Fig. 3.24. Debye-Scherrer rings at 750°C with some crystallographic planes of α, β and TiC phases identified: a) unreinforced Ti662 alloy and b) TiC particle reinforced Ti662 alloy.

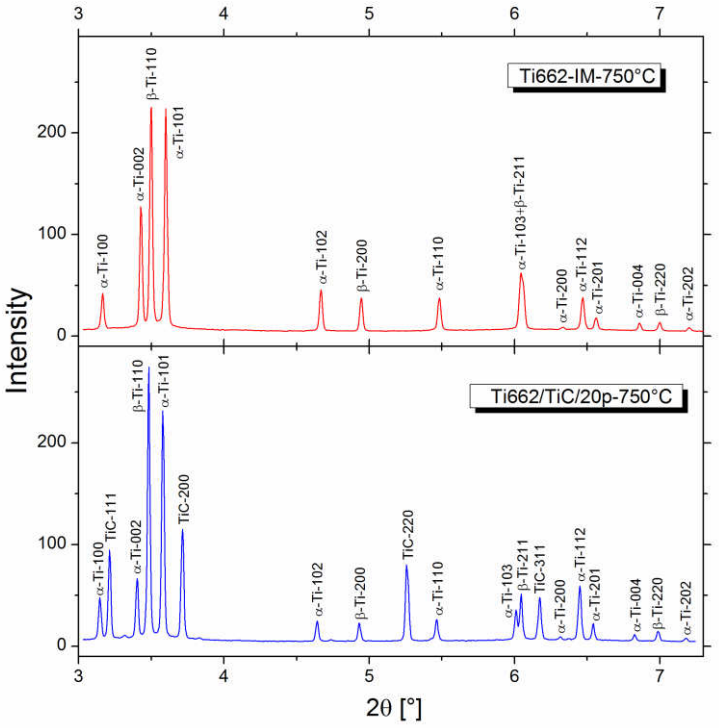

Fig. 3.25. Diffractograms of unreinforced (upper) and reinforced (bottom) Ti662 alloy at 750°C integrated in the axial direction.

3.4.2 Determation of the stress-free lattice spacing d_0 in the neutron diffraction experiments

A major limitation of stress analysis in the bulk by lattice diffraction is that, in order to obtain absolute stresses, additional measurements are required to determine the unstrained lattice parameters d_0. In principle, this can be accomplished by investigating a stress-free reference sample using the same diffraction set-up. In the present study, 2124, 6061 and SiC powders as well as bulk extruded matrix samples with and without ball milling, all of them after the same thermal treatment (T7), were evaluated to be used as the stress-free reference d_0. These samples were heated up with the same heating rate used for the composites. The powders were canned in vanadium containers of the same size of the samples: length = 5 mm and diameter = 5 mm. Vanadium is nearly invisible in neutron diffraction experiments because of its negligible absorption.

3.4.3 Determination of the stress-free lattice spacing d_0 in the synchrotron diffraction experiments: $sin^2\psi$ method

The reference d_0 was calculated using the $\sin^2\psi$ method proposed by Hauk et al. [96]. The interplanar distance (d) is determined as a function of $\sin^2\psi$ for the different externally applied loads. In the elastic regime a set of straight lines is obtained, one for each external load. The intersection of these lines gives the corresponding stress-free lattice spacing d_0.

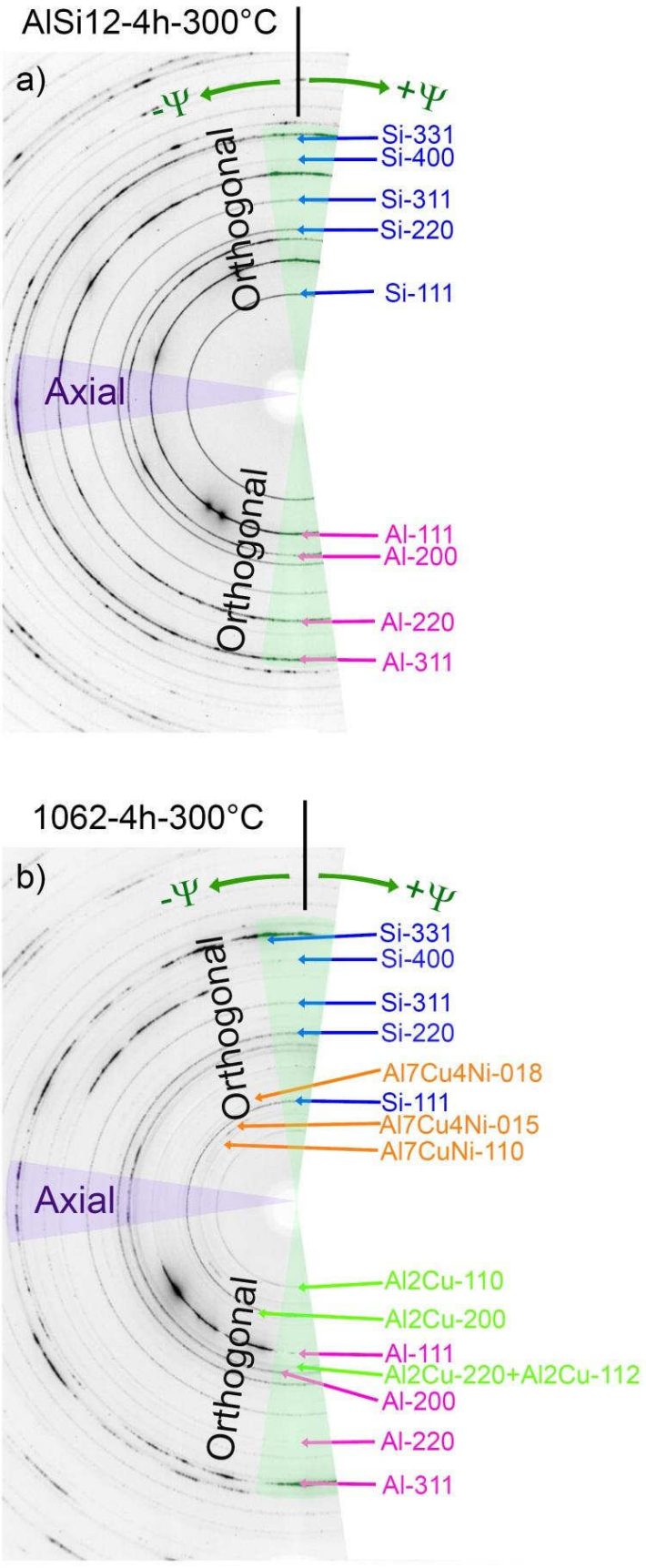

Fig. 3.26. Debye-Scherrer rings at 300°C with some crystallographic planes of different phases indicated in a) the AlSi12 alloy and b) 1062 alloy.

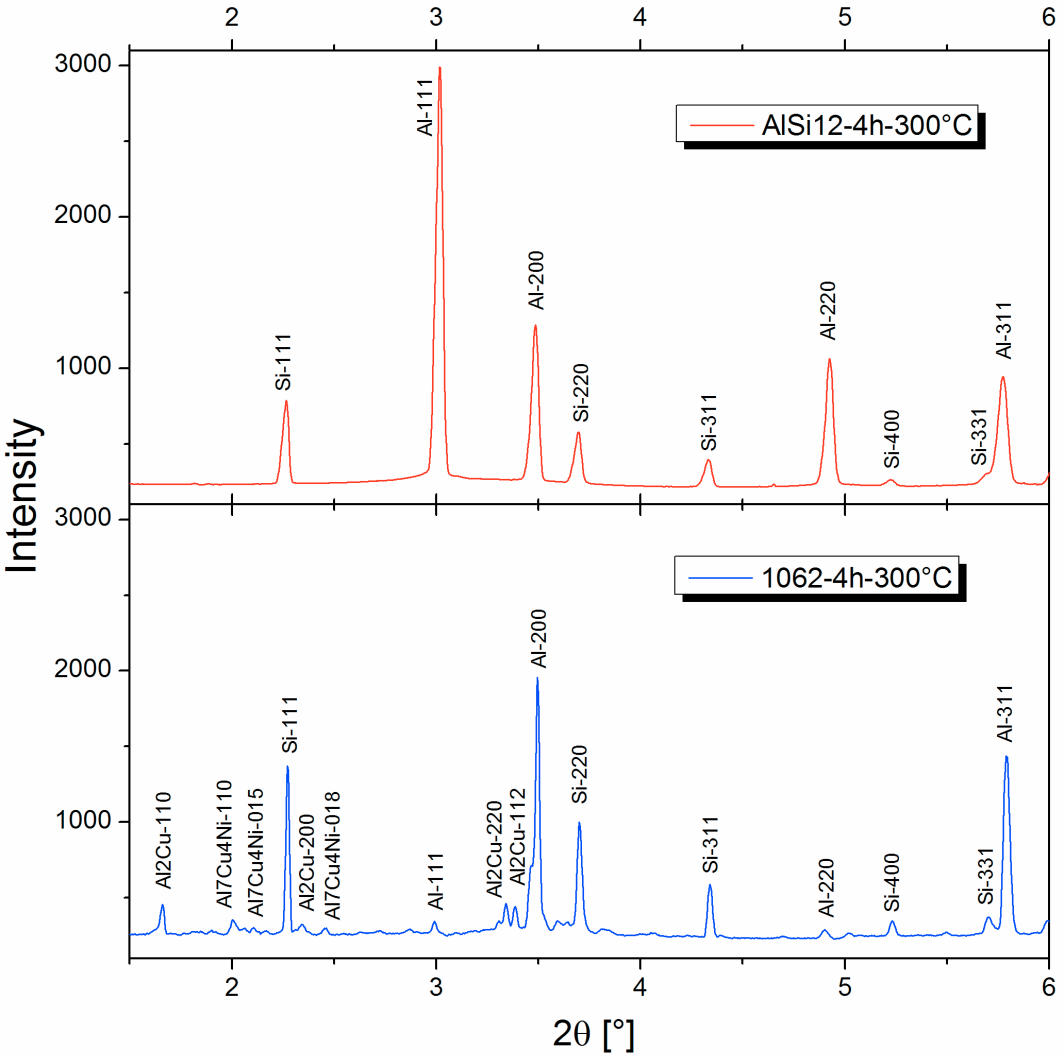

Fig. 3.27. Diffractograms of the AlSi12 and 1062 alloys in the axial direction.

3.4.4 Strain calculation

The elastic strains in the principal directions *i*, for both the neutron and synchrotron diffraction experiments, can be calculated by the shift of the position of the diffraction peak of the considered *{hkl}* plane by:

$$\varepsilon_i = \frac{d-d_0}{d_0} = -(\theta - \theta_0)\cot^{-1}\theta_0 \qquad (3.1)$$

where d and d_0 are the interplanar distances for the stressed and the stress-free condition, respectively, evaluated with the Bragg's law. The strain errors were calculated propagating the errors obtained by fitting of the diffractograms [45].

3.4.5 Stress calculation

The principal stresses in the individual phases in the principal directions *i* are related to the principal elastic strains via the Hooke's law (see e.g. [97]):

$$\sigma_i = \frac{E}{1+\nu}\varepsilon_i + \frac{E}{(1+\nu)(1-2\nu)}\left(\sum_{j=1}^{3}\varepsilon_j\right) \qquad (3.2)$$

where E and ν are the Young's modulus and the Poisson's ratio of the corresponding $\{hkl\}$ planes of the phase considered.

For the cylindrical samples, a cylindrical stress symmetry was assumed, with σ_1 being the principal stress in the direction of the length of the sample (hereafter axial direction) (see Fig. 3.12 and Fig. 3.13 b). The other two principal stresses are assumed to be equal, i.e., $\sigma_2 = \sigma_3$ in the radial direction of the sample.

A cylindrical stress symmetry was also assumed for the modified "dogbone" sample geometry (Fig. 3.13 a) in the Ti alloys with σ_1 being the principal stress in the RD direction (length of the sample - see Fig. 3.5). The other two principal stresses are assumed to be equal, i.e., $\sigma_2 = \sigma_3$ (ND and TD - see Fig. 3.5).

The plane-specific Young's modulus at room temperature (RT) were considered to compute the stresses in the SiC, Si, α-Ti, TiC and Al phases: $E_{SiC(202)}$ = 421.7 GPa, $E_{Si(311)}$ = *159.2 GPa*, $E_{\alpha\text{-}Ti(103)}$ = 120.8 GPa, $E_{TiC(311)}$ = 450.6 GPa, $E_{Al(311)}$ = 69.4 GPa and Poisson's ratio $\nu_{(202)}$ = 0.166, $\nu_{(311)}$ = 0.229, $\nu_{(103)}$ = 0.307, $\nu_{(311)}$ = 0.189 and $\nu_{(311)}$ = *0.35* for SiC, Si, α-Ti, TiC and Al, respectively. These values were calculated using the software by Wern [98] based on the Kröner model. The elastic constants were assumed constant from RT up to 300ºC for SiC and Si. In the case of Al and TiC, $\nu_{Al(311)}$ and $\nu_{TiC(311)}$ were considered to be constant throughout the whole temperature range, whereas for the Young Modulus $E_{Al(311)}$ and $E_{TiC(311)}$, the temperature dependence of the macroscopic Young's modulus of the alloy was used [65,67,87,99,100]. The temperature dependence of the macroscopic Young´s modulus and Poisson´s ratio was used for the α-Ti phase [8]. The lack of plane-specific constants for the β-Ti phase leads to use macroscopic values for the β-(211) plane, where a linear dependence was assumed from RT up to 1000°C [101-102].

3.5 Microstructure evolution

The evolution of the Debye-Scherrer rings acquired during the in situ synchrotron diffraction experiments was analyzed as explained in [78].The steps followed are shown in Fig. 3.28:

1) The diffraction images are stacked sequentially using ImageJ [103] (Fig. 3.28 a).

2) One crystallographic plane is selected for individual analysis. The diffraction ring corresponding to the selected plane is transformed into Cartesian coordinates using a polar

transformation [104]. This results in a 3-D volume where the 3 axis correspond to the azimuthal angle, strain and width (2θ) of the diffraction ring (Fig. 3.28 b).

3) The 3D volume is summed and projected over the strain-ψ plane. The final representation corresponds to the evolution during deformation of grains oriented matching the Ewald's sphere (Fig. 3.28 c).

3.6 Rietveld Analysis (synchrotron diffraction experiments)

A least-squares Rietveld refinement was carried out for the quantitative and texture analysis using the software MAUD [105]. The original images from 2-D Pixium and mar555 detectors were converted into Tiff files with Fit2D. MAUD integrates a software module of ImageJ that allows the integration of Tiff float images (32 bits) to obtain the diffractograms. The Debye-Scherrer rings were integrated every 10° and 15° for Ti and Al alloys, obtaining the diffractograms corresponding to the different azimuthal angles.

The instrumental broadening was calculated with scans of LaB_6 powders. Peak fitting with background functions of up to 4 degree polynomials and pseudo-Voigt functions for the peak shape were imposed to the diffractograms. Additionally, the anisotropic crystallite size of Popa was chosen for the diffractograms corresponding to the alloys and an isotropic model for the LaB_6 powders [106]. The orientation distribution function (ODF) was determined with an E-WIMV algorithm, derived from WIMV (Williams-Imhof-Matthies-Vines) [107-109]. The intensity of the Ti alloys was integrated over 360° while the cast Al alloys were integrated from Ψ=90° to Ψ=270°.

3.7 Electron microscopy and Electron Back Scattering Diffraction

Scanning electron microscopy (SEM) and electron backscattering diffraction (EBSD) were performed with a FEI Quanta 200 Field Emission Gun SEM microscope (FEG-SEM) located at the USTEM (Vienna University of Technology).

3.8 Experimental Summary

The different alloys with the type of sample, tests, temperatures, diffraction methods and gauge volumes are summarized in Table 3.3.

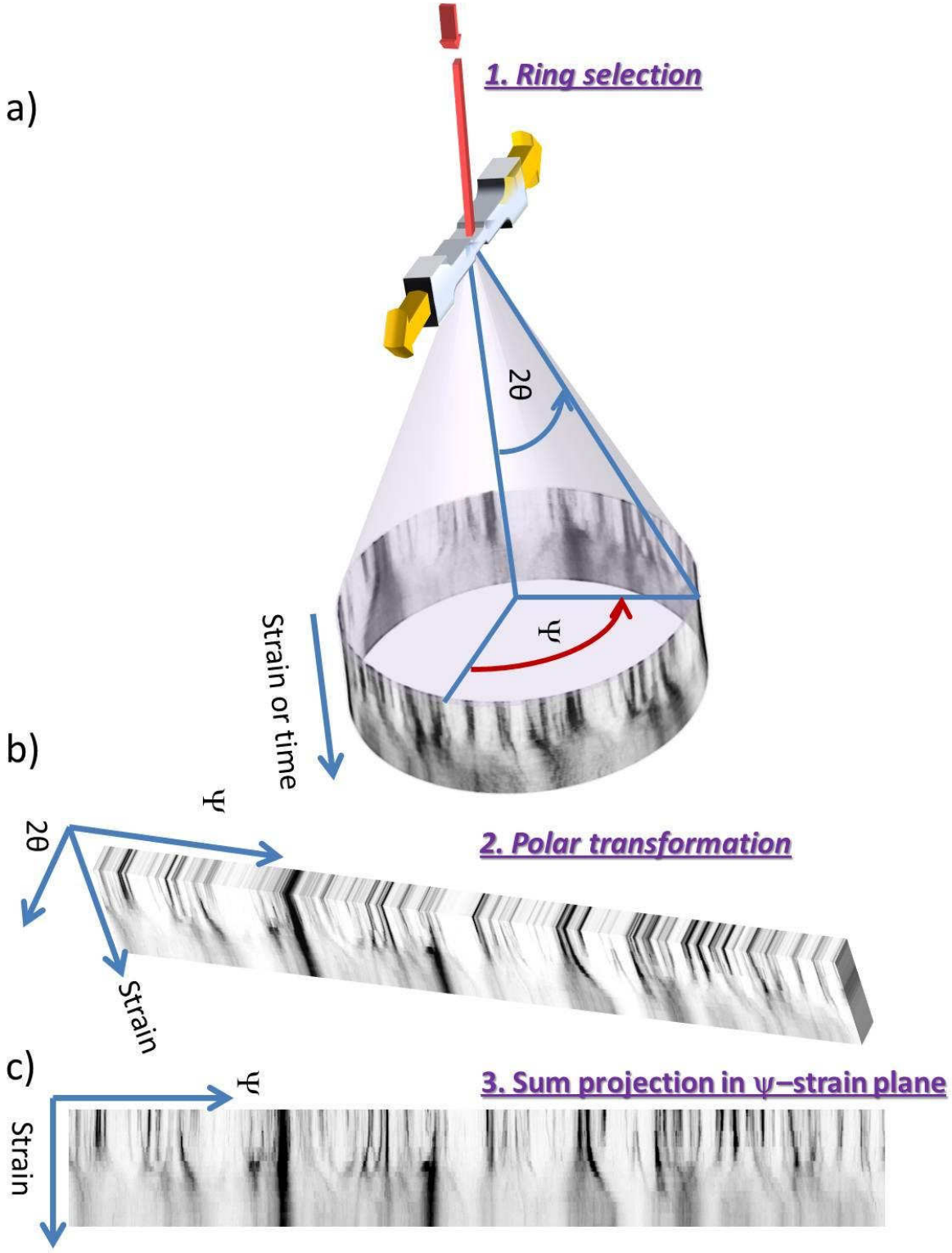

Fig. 3.28. Schematic representation of the procedure applied to follow the evolution of the diffractograms during deformation.

Alloy	Sample	Test	Temperatures	Diffraction Metthod	Gauge Volume
AlSi12	Cylindrical Ø = 5 mm length = 10 mm	Compression	300°C	Synchrotron	1x1x5mm^3
1062	Cylindrical Ø = 5 mm length = 10 mm	Compression	300°C	Synchrotron	1x1x5mm^3
Ti662	Square section (modified dogbone) 1.5x2mm²	Tensile	650°C 750°C	Synchrotron	0.3x0.3x1.5 mm^3
2124/SiC/25p<20	Cylindrical Ø = 5mm length = 5 mm	Thermal cycling	[RT-300°C]	Neutron	5x5x5 mm^3
6061/SiC/25p<20	Cylindrical Ø = 5mm length = 5 mm	Thermal cycling	[RT-300°C]	Neutron	5x5x5 mm^3
Ti662/TiC/12p	Square section (modified dogbone) 1.5x2mm²	Tensile	750°C 850°C	Synchrotron	0.3x0.3x1.5mm^3
Ti662/TiC/20p	Square section (modified dogbone) 1.5x2mm²	Tensile	750°C 850°C	Synchrotron	0.3x0.3x1.5mm^3

Table 3.3. Summary of materials and experiments.

4 Results

4.1 Unreinforced lightweight alloys

The following sections present the results obtained for all the investigated multiphase lightweight metallic materials.

4.1.1 AlSi12 alloy

The compression tests were carried out at 300°C and the resulting true-stress vs. true-strain curves for different ST conditions are shown in Fig. 4.1. The AC condition exhibits the highest strength with ~ 71 MPa and decreases to ~ 56 MPa during softening. The 1h and 4h conditions show maximum strengths of ~ 50 MPa and ~ 43 MPa, respectively. Both ST conditions slightly soften to ~ 44 MPa for the1h ST and to ~ 40 MPa for the 4h ST.

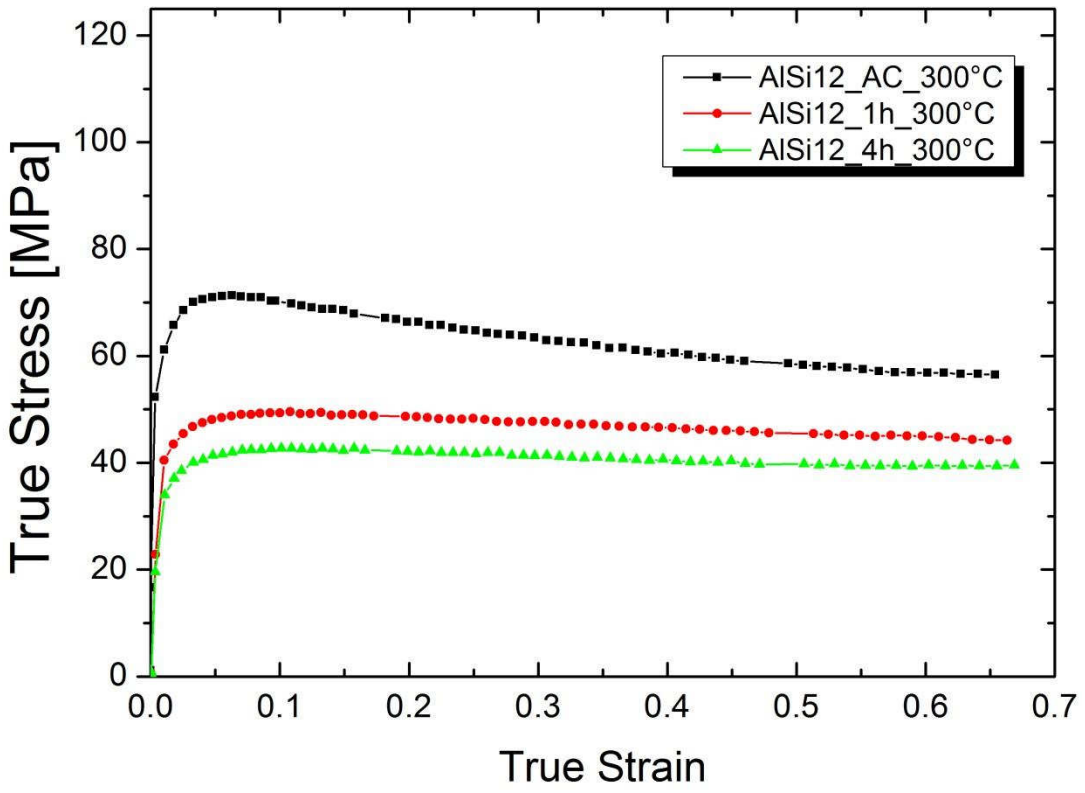

Fig. 4.1. True-stress vs. true-strain curves obtained during compression tests at 300°C for AlSi12 alloy with different solution treatment times at 500°C.

The beginning of the compression tests was selected as stress-free interplanar distance d_0 and used for the elastic strain evaluation of the corresponding crystallographic plane of Si (as commented in 3.4.3). The Al phase, owing to the poor grain statistics within the gauge volume, did not show realistic strain evolution.

Fig. 4.2 shows the elastic strain evolution during compression for different Si-planes of the AlSi12 alloy upon different ST, i.e., AC (left), 1 h ST (centre) and 4 h ST (right).

The Si-reflections show maximum axial strains of ~ - 2 × 10^{-3}, ~ - 1 × 10^{-3} and ~ - 0.8 × 10^{-3} for the AC condition, 1h and 4h ST, respectively. The radial direction strains reflect the Poisson's effect that result in positive strain values. Subsequently, the axial strains evolve similarly to the macroscopic curves, with the highest softening in the AC condition and the lowest in the 1h ST.

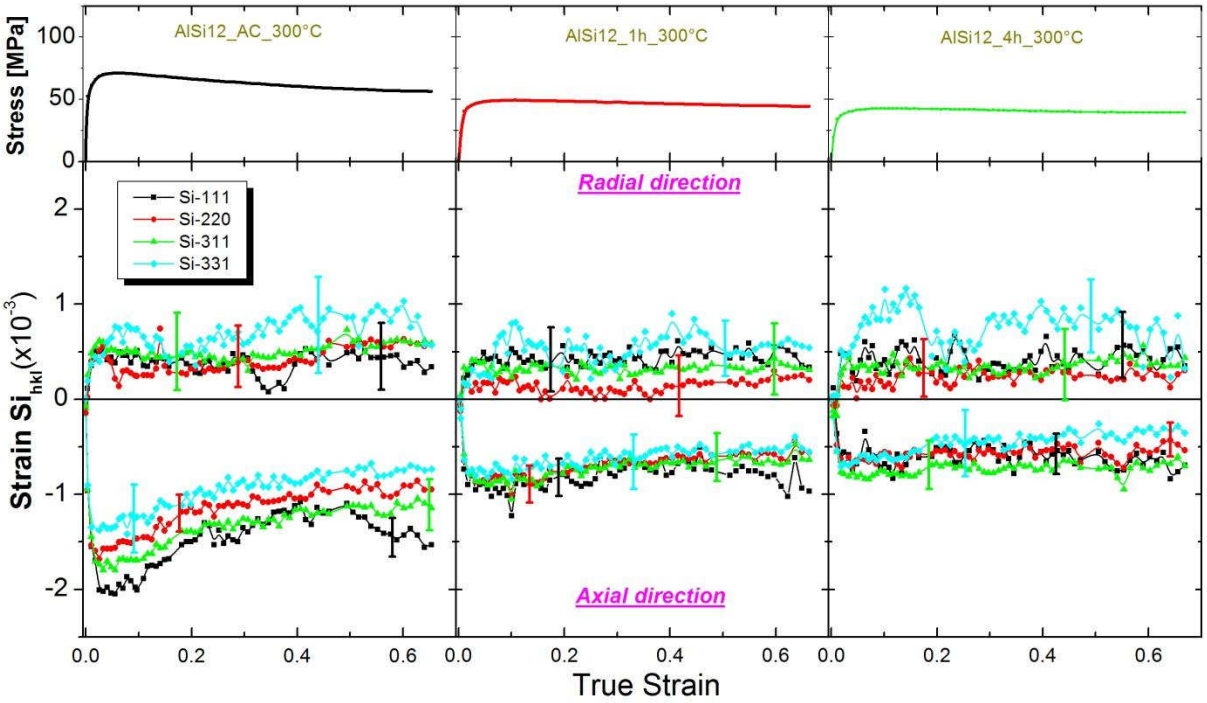

Fig. 4.2. Lattice strain evolution during compression at 300°C for the Si-phase in the axial (negative) and radial directions (positive): AC (left), 1h ST (centre) and 4h ST (right). Typical error bars are indicated.

4.1.2 AlSi piston alloy

The true-stress vs. true-strain curves for the 1062 alloy at 300°C are shown in Fig. 4.3. The AC condition exhibits the highest strength, i.e., ~ 110 MPa with subsequent softening until a true strain of ~ 0.3, when the stress is similar to the to ST conditions. The 1h and 4 h ST conditions show a maximum strength of ~ 106 MPa, followed by softening down to ~ 75 MPa at the end of the test.

An initial stress-free condition for all phases is also assumed, i.e., the strains are considered zero at the beginning of the compression tests. Similarly to the AlSi12 alloy, the Al-phase shows unreliable strains due to the coarse grains from the casting process.

Fig. 4.4 shows the elastic strain evolution at 300°C for different Si-reflections of the 1062 alloy: AC (left), 1 h ST (centre) and 4 h ST (right). The Si-reflections for the AC condition have a maximum strain of ~ - 1.9 × 10^{-3} while for the ST conditions is ~ -1.5 × 10^{-3}.

Subsequently, the strains decrease with similar softening slopes for all conditions. The radial direction strains reveal the Poisson's effect that results in positive strain values.

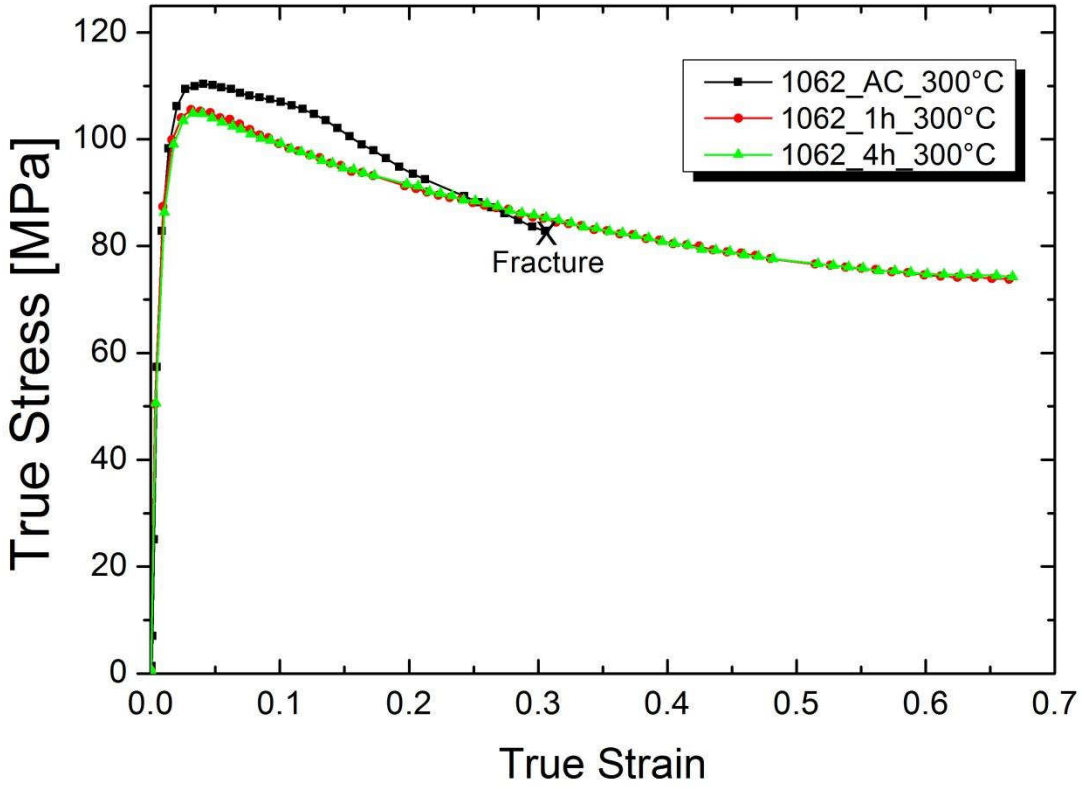

Fig. 4.3. True-stress vs. true-strain curves obtained during compression tests at 300°C for the 1062 alloy after different solution treatment times at 500°C.

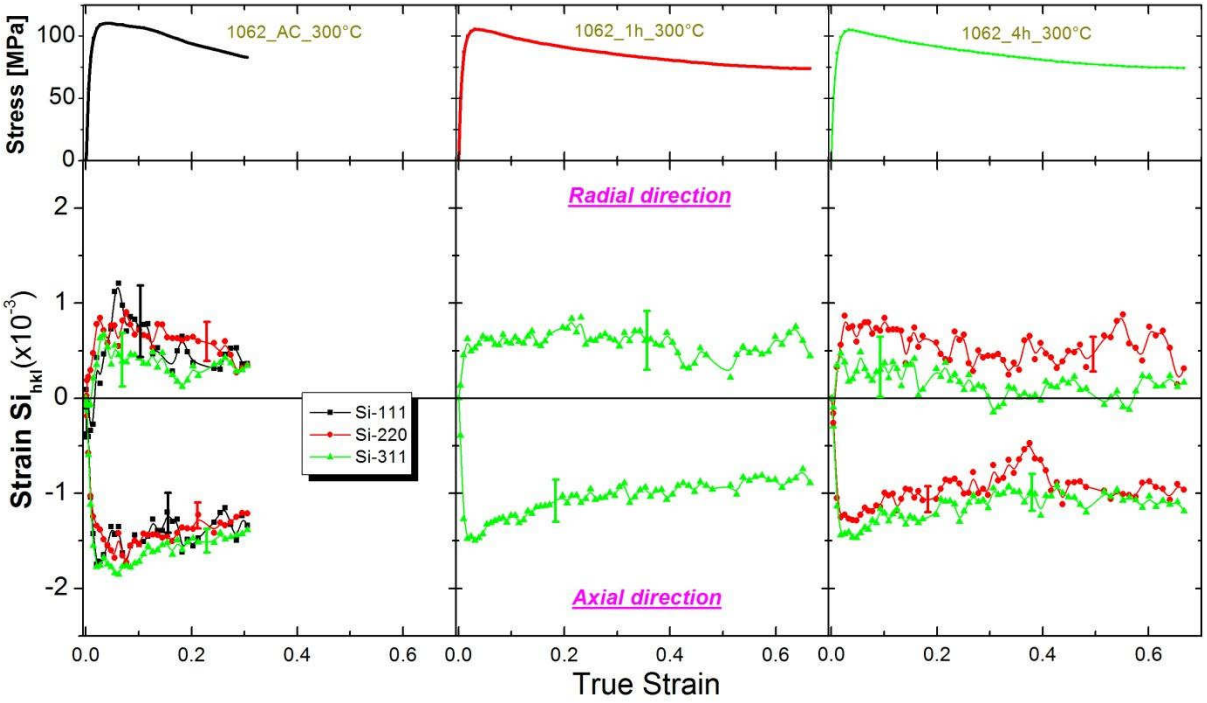

Fig. 4.4. Lattice strain evolution during compression at 300°C for the Si-phase in the axial (negative) and radial directions (positive): AC (left), 1h ST (centre) and 4h ST (right). Typical error bars are indicated.

The Al_2Cu-phase (Fig. 4.5) develops maximum strains of ~ - 2 × 10^{-3} in the axial direction for the AC and 1h ST conditions and ~ - 1.5 × 10^{-3} for 4h ST. For all conditions, the axial strains are abruptly reduced to ~ - 1 × 10^{-3} at true strain ~ 0.1, remaining then practically constant. In the radial direction, the AC condition behaves similarly to the axial direction but with positive strains. The ST conditions have a constant radial strains close to 0 MPa from the beginning of the compression.

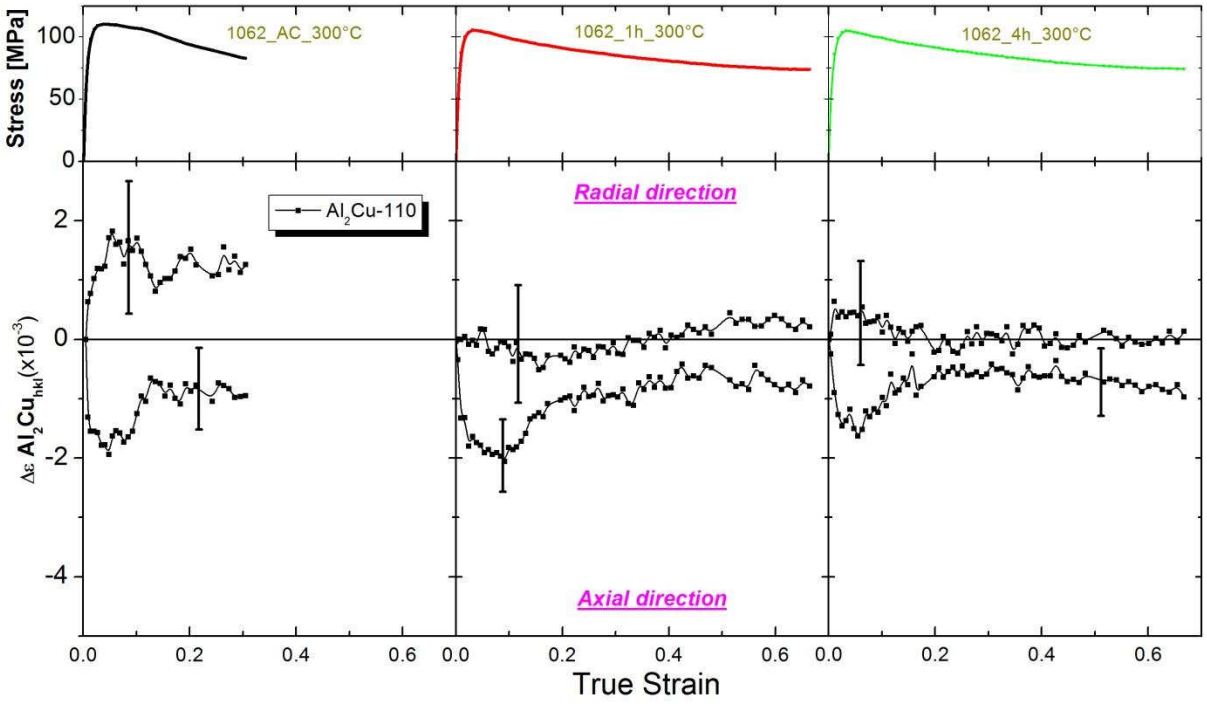

Fig. 4.5. Lattice strain evolution during compression at 300°C for the Al_2Cu-phase in the axial and radial directions: AC (left), 1h ST (centre) and 4h ST (right). Typical error bars are indicated.

4.1.3 Unreinforced Ti662 alloys

The different tensile tests carried out with the unreinforced titanium alloys are shown in Fig. 4.6. The x-axis corresponds to the engineering macroscopic strain and the y-axis to the engineering stress. The IM alloy shows less softening than the PM alloy. At 650°C, the IM exhibits higher strength than the PM material, while this behaviour is inverted at 750°C. The strain to failure of the PM material is significantly smaller than for the IM alloy. The maximum strain shown for the IM alloys is 0.15 since Rietveld refinements show constant vol.% of α- and β-phases up to this value, with subsequent local temperature increase.

Fig. 4.7 shows the *d* vs. $\sin^2 \psi$ plots (see 3.4.3) for the α-100 reflection at 650°C for the IM (left) and PM (right) alloys. The plots corresponding to other α-reflections (α-002, α-101 α-102, α-110, α-103, α-112 and α-201) are shown in the Appendix. The images acquired with the 2D-Pixium detector were rotated 90° counterclockwise. Therefore,

$\sin^2 \psi = 0$ corresponds to the orthogonal direction and $\sin^2 \psi = 1$ to the axial or load direction. The R^2 values of the linear fits are also indicated. The IM shows R^2 values close to 1 for all crystallographic planes while for the PM is close to 0 at the beginning of test, increasing progressively with the external load. Only linear fits with $R^2 \geq \sim 0.8$ are shown. Fig. 4.8 shows similar behaviour at 750°C for the α-100 reflection as that observed for IM and PM at 650°C.

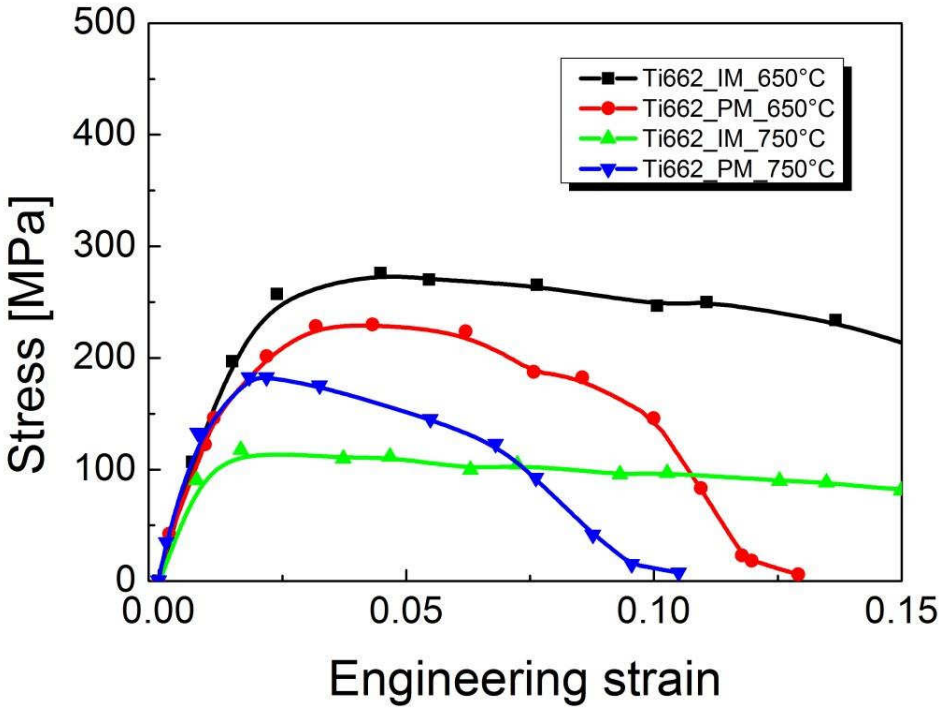

Fig. 4.6. Engineering stress vs. strain curves for the unreinforced Ti662 alloys under tensile loading at 650°C and 750°C.

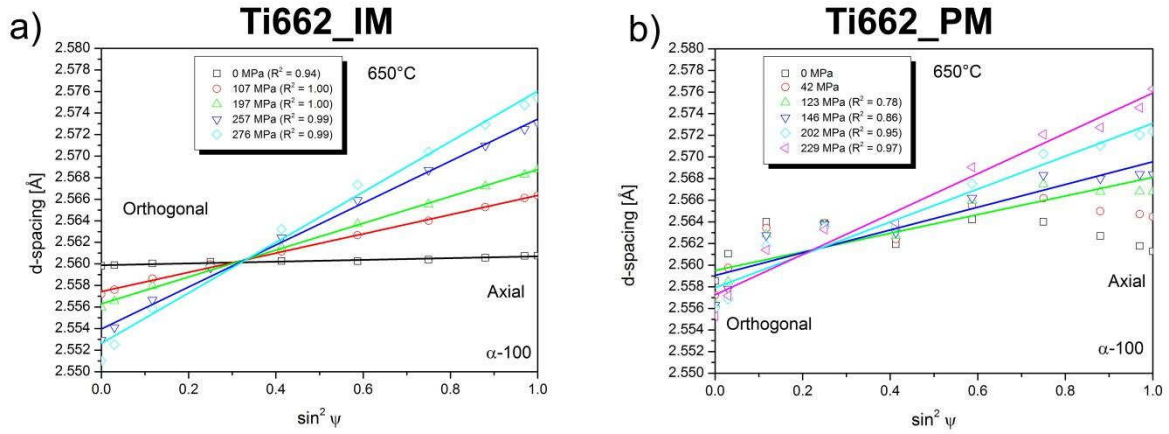

Fig. 4.7. *d* vs $\sin^2 \psi$ plots with the linear fits at different stresses for the α-100 Ti reflection at 650°C: a) Ti662 IM alloy b) Ti662 PM alloy. R^2 values are also indicated.

d vs. $\sin^2 \psi$ plots for β-reflections show similar behaviour for the IM alloy to that observed for the α-reflections at both temperatures, i.e. linear fits with $R^2 \geq 0.8$. On the contrary, the R^2 values for the PM alloy show values ≤ 0.8 at the beginning of the test owing

to the poor grain statistics within the gauge volume. In order to compare both alloys and temperatures, the *d* value obtained at the beginning of the tensile tests was chosen as d_0 for the β-reflections. This results in a β-strain analysis from an incremental point of view.

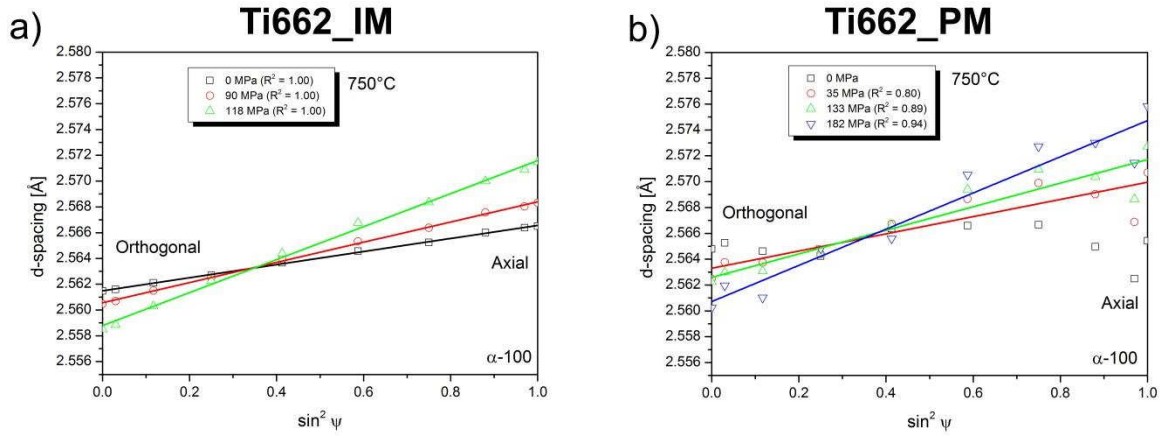

Fig. 4.8. *d* vs $\sin^2 \psi$ plots with the linear fits at different stresses for the α-100 Ti reflection at 750°C: a) Ti662 IM alloy b) Ti662 PM alloy. R^2 values are also indicated.

In Table 4.1 are included the different d_0 used for the α-strain evaluation, which are only those reflections that show a strain evolution with applied load. The intersection of the linear fits in the *d* vs. $\sin^2 \psi$ plots was selected as stress-free interplanar distance d_0 and used for the elastic strain evaluation of the corresponding crystallographic plane.

(hkl)	Ti662_IM_650°C	Ti662_PM_650°C	Ti662_IM_750°C	Ti662_PM_750°C
α-100	2.5604±0.0003	2.5621±0.0011	2.5634±0.0000	2.5652±0.0008
α-002	2.3638±0.0005	X	2.3674±0.0005	X
α-101	2.2515±0.0002	2.2536±0.0005	2.2541±0.0000	2.2553±0.0005
α-102	1.7367±0.0000	1.7397±0.0004	1.7390±0.0000	1.7408±0.0006
α-110	1.4782±0.0000	1.4797±0.0007	1.4797±0.0003	1.4809±0.0000
α-103	1.3417±0.0002	1.3441±0.0003	1.3441±0.0005	1.3449±0.0003
α-112	1.2533±0.0001	1.2547±0.0005	1.2548±0.0000	1.2555±0.0000
α-201	X	1.2366±0.0002	1.2371±0.0000	1.2378±0.0000

Table 4.1. d_0 values [Å] obtained for different α-reflections of the unreinforced Ti662 alloys at different temperatures.

The elastic strains in the α-phase in axial (top) and orthogonal (bottom) directions are shown in Fig. 4.9 for both production routes. Similar plots are shown in Fig. 4.10 for the β-phase. For every plot, the diagrams at the top correspond to the engineering stress-strain curves. Only the phase strains with errors allowing a sensible analysis are shown. For readability, the error bar is indicated as an upper limit that corresponds to the crystallographic plane with identical colour.

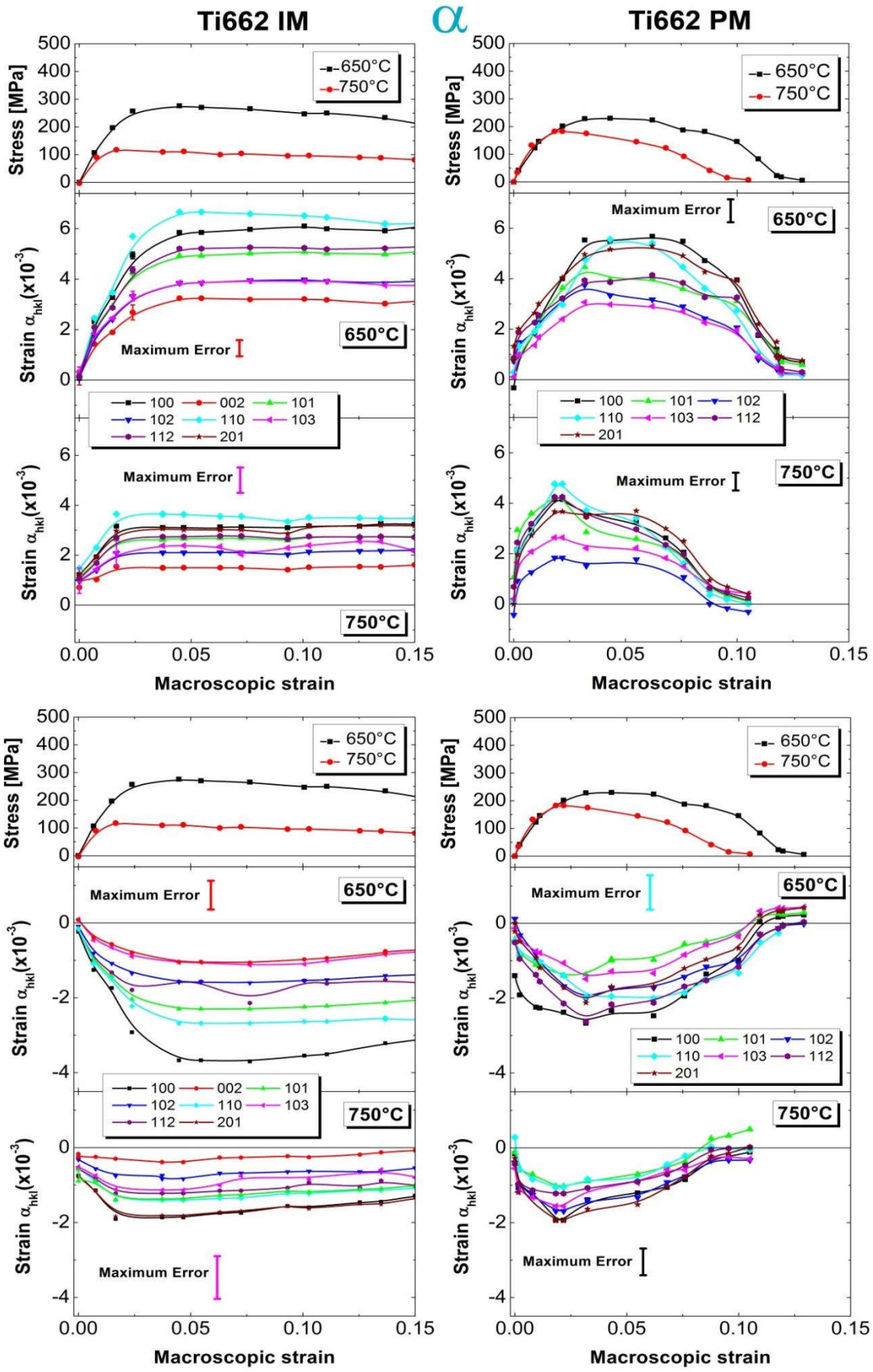

Fig. 4.9. α-lattice strain evolution in the longitudinal (upper) and orthogonal directions (bottom) during tensile loading of the IM (left) and PM (right) alloys.

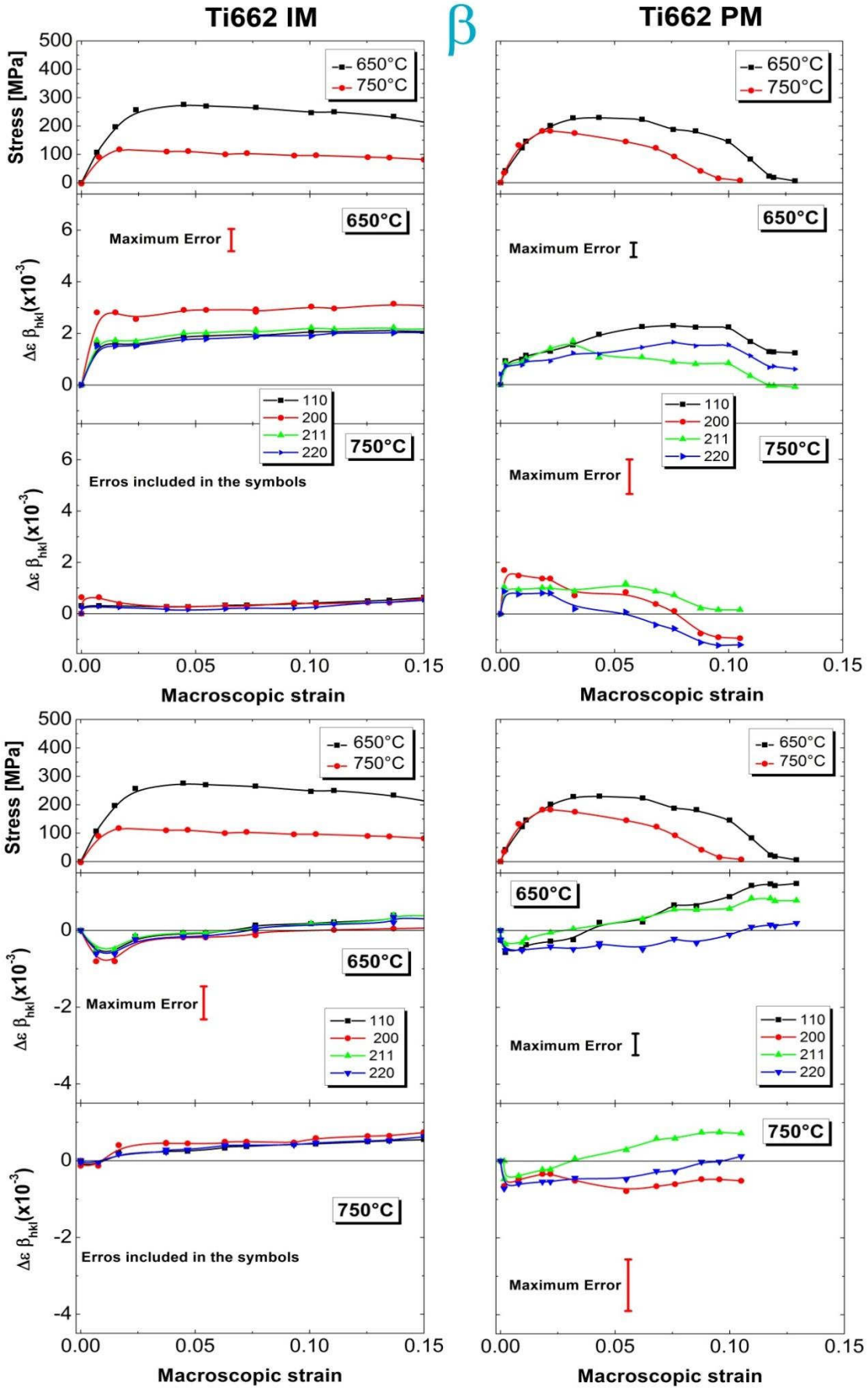

Fig. 4.10. β-lattice strain evolution in the longitudinal (upper) and orthogonal directions (bottom) during tensile loading of the IM (left) and PM (right) alloys.

The initial axial strains in the α-phase of the IM material are ~ 0 and ~ 1 – 1.5 × 10^{-3} at 650°C and 750°C, respectively. The values for the PM are close to zero for both temperatures.

At 650°C, the α-strains in the IM alloy reproduce the strain hardening behaviour of the macroscopic stress-strain curve until the maximum external stress is reached at ~ 250 MPa, i.e., ε ~ 0.03. The α-strains remain practically constant for macrostrains ε > 0.03. At 750°C, the α-strains show an increase with approx. constant slope as deformation proceeds until yielding a maximum at a macrostrain of ~ 0.02. The maximum strain sequence in increasing order is α-002, α-102 and α-103, α-101 and α-112, α-201 (not shown at 650°C), α-100 and finally α-110 with 6.5 × 10^{-3} and 3.5 × 10^{-3} at 650°C and 750°, respectively.

The PM alloy shows an increase of α-strain until a maximum is reached at macrostrains of ~ 0.03 and ~ 0.02 at 650°C and 750°C, respectively. These coincide with the strains at which the maximum strength of the material is reached. Above this macrostrain, the α-strains reproduce the strain softening behaviour exhibited by the macroscopic stress-strain curves. The *hkl* sequence of maximum strains is practically the same as for the IM alloy. Final strains are at the same level of the initial strains and close to 0 for both temperatures.

In the orthogonal direction all the strains are negative during deformation owing to the Poisson's effect, reaching the highest values at maximum external stress. A slight strain softening can be observed for some α-planes of the IM alloy.

The β-phase (Fig. 4.10) in the IM and PM materials plastifies in the early stages of the experiment, i.e., below ~ 100 MPa for the IM alloy and ~ 50 MPa for the PM material at both temperatures. Subsequently to the plastification at 650°, the IM alloy exhibits constant behaviour in the axial direction with Δε < 1 × 10^{-3} for the considered β-planes. At 750°C, Δε is the same for all reflections, i.e., ~ 0.5 × 10^{-3}.

The PM alloy shows larger Δε scattering for different reflections than the IM material because of the poor statistics of the β-phase in the diffraction images.

Fig. 4.11 shows Debye-Scherrer rings obtained for the IM alloy at 650°C as an assembly of four sectors with different external loads. The reflections are indicated in Fig. 3.24. On the right, the engineering stress vs. strain curve is depicted to correlate possible changes in the rings with the external stress applied. The initial rings are continuous from the beginning of the tensile test. Furthermore, the intensity shows a heterogeneous distribution but, in some cases, symmetry along individual rings can be seen. For instance, α-110, at azimuthal angles of ~ 45°, ~ 135° and ~ 225° and ~ 315° exhibits an intensity maximum,

involving this arc ± 10°. Fig. 4.12 shows the Debye-Scherrer rings corresponding to the IM alloy at 750°C, with features similar to 650°C.

Significant changes are observed for the PM alloy at 650°C (Fig. 4.13). The initial rings for all α- and β-reflections are discontinuous reflecting the large grain size of the alloy (Fig. 4.13 a)). Further evolution of the tensile deformation leads to a homogenization of the intensity distribution along individual diffraction rings, becoming finally practically continuous at 183 MPa (Fig. 4.13 c)). The PM alloy undergoes similar behaviour at 750°C (Fig. 4.14).

Three α- and two β-reflections are shown in Fig. 4.15 to Fig. 4.16 to analyze the microstructural evolution during tensile deformation. The macroscopic engineering stress vs. strain curves are also plotted. Azimuthal angles $\psi = 90°$ and $\psi = 270°$ correspond to the axial (A) direction, while $\psi = 0°$, $\psi = 180°$ and $\psi = 360°$ to the orthogonal (O) direction. Only the results for the PM material are shown since the small grain size of the IM material does not allow identifying the evolution of individual diffraction spots during deformation (continuous Debye-Scherrer rings).

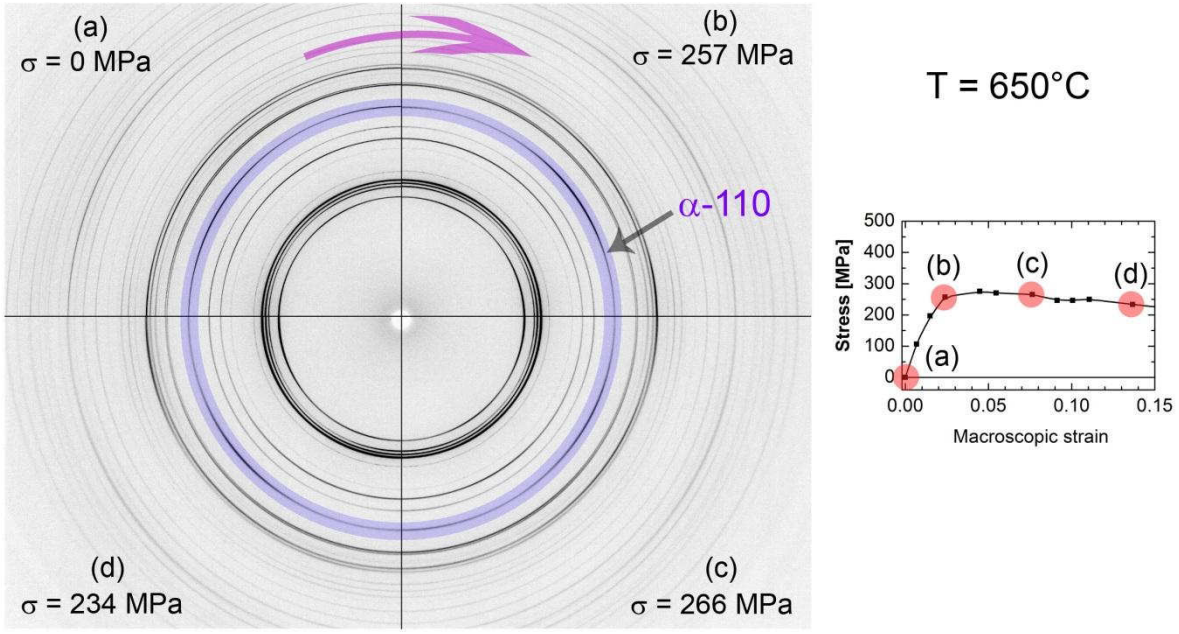

Fig. 4.11. Representative sections of the diffraction rings acquired during the in situ tensile tests for the IM alloy at 650°C. Corresponding α- and β-planes are indexed in Fig. 3.24 a). On the right, the macroscopic stress vs. strain curve is plotted. The red circles correspond to the loads for which the rings sectors are depicted.

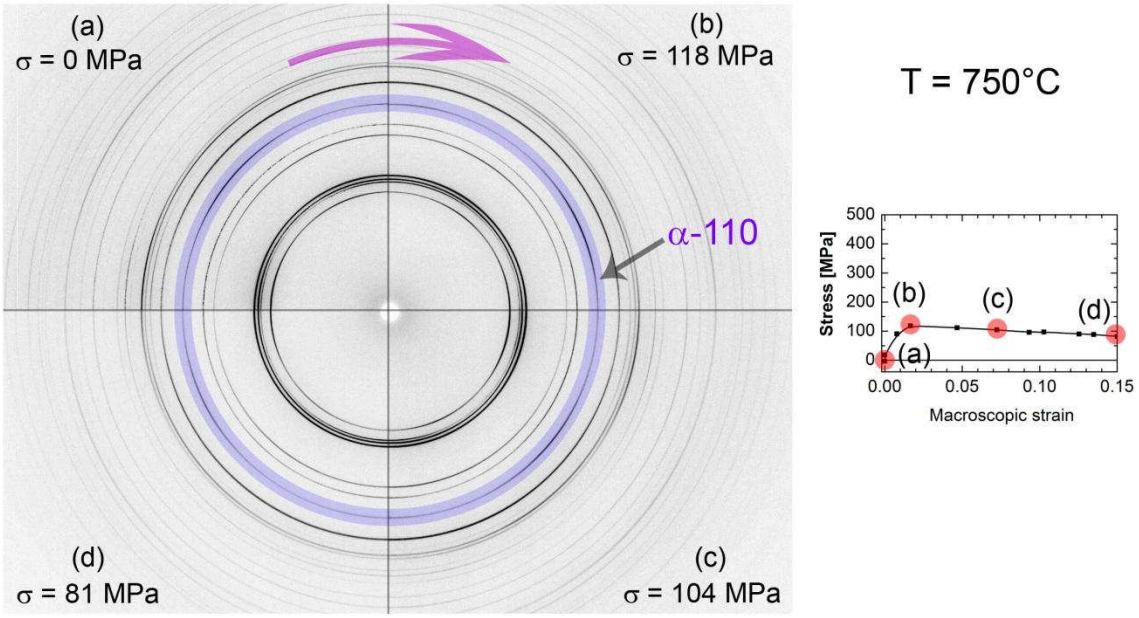

Fig. 4.12. Representative sections of the diffraction rings acquired during the in situ tensile tests for the IM alloy at 750°C. Corresponding α- and β-planes are indexed in Fig. 3.24 a). On the right, the macroscopic stress vs. strain curve is plotted. The red circles correspond to the loads for which the rings sectors are depicted.

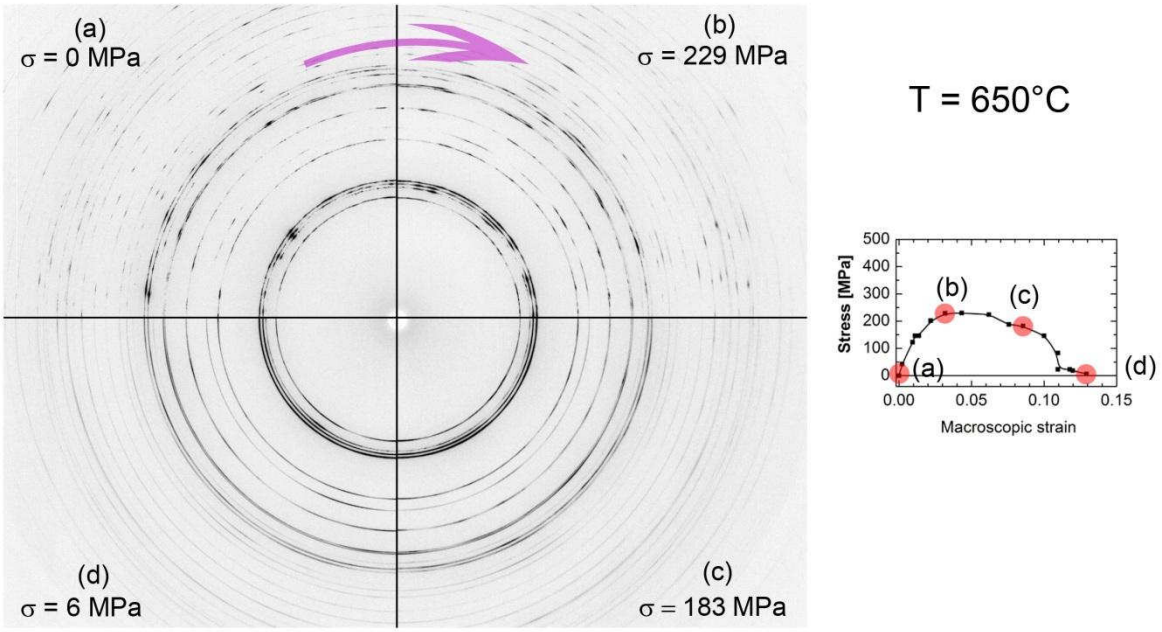

Fig. 4.13. Representative sections of the diffraction rings acquired during the in situ tensile tests for the PM alloy at 650°C. Corresponding α- and β-planes are indexed in Fig. 3.24 a). On the right, the macroscopic stress vs. strain curve is plotted. The red circles correspond to the loads for which the rings sectors are depicted.

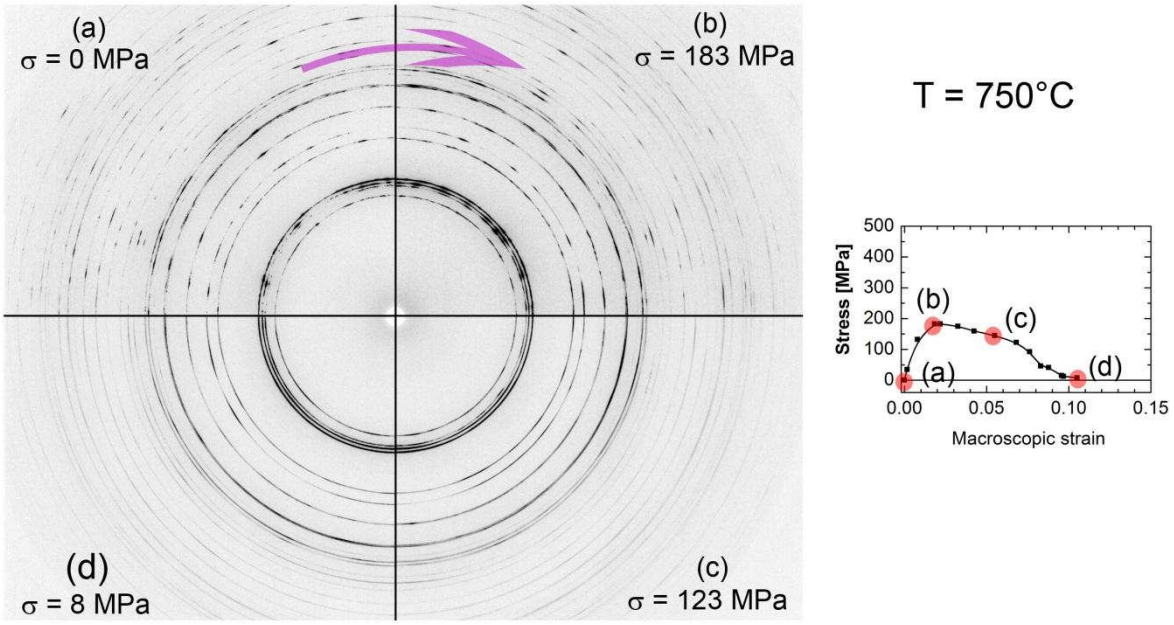

Fig. 4.14. Representative sections of the diffraction rings acquired during the in situ tensile tests for the PM alloy at 750°C. Corresponding α- and β-planes are indexed in Fig. 3.24 a). On the right, the macroscopic stress vs. strain curve is plotted. The red circles correspond to the loads for which the rings sectors are depicted.

Fig. 4.15 shows the evolution of the PM alloy during deformation at 650°C. The initial pattern, where only some diffraction spots are visible, is the origin of the evolution of high intensity narrow regions (in dark) as deformation advances. These bands remain vertical and constant in width for all the α- and β-planes until the maximum macroscopic stress is reached at ~ 230 MPa, i.e., $\varepsilon = 0.03$. Above $\varepsilon = 0.03$, some of the α-bands change the azimuthal angles with no apparent preferred orientation resulting in the inclined bands seen in Fig. 4.15. Furthermore, the diffraction bands become wider and, as a consequence, the intensity distribution becomes more homogeneous along Ψ. The diffraction bands start to newly take their vertical orientation for $\varepsilon > \sim 0.09$ indicating that no significant further evolution takes place above this strain. At the end of the experiment, the intensity is more continuously distributed along Ψ. The bands corresponding to the β-planes spread changing their spotty distribution into a pattern with more homogeneous intensity distribution along Ψ for $\varepsilon > 0.03$. Identically to the α-planes, this process is active until $\varepsilon \sim 0.09$. This analysis is also applicable for the in situ tensile test at 750°C (Fig. 4.16), where also a strain of ~ 0.03 provokes the activation of the processes.

The intensity evolution as a function of Ψ is shown in Fig. 4.17 to Fig. 4.18 at four different strains for the IM alloy. Additionally, on the right bottom, the engineering stress vs. strain curve is plotted with the coloured circles indicating the corresponding stress/strain intensity curve. Clear texture can be observed at beginning of the tests for both temperatures.

The maxima remain in the same position as deformation advances but the intensity curves become more clearly defined after the strain at which maximum stress reached is surpassed.

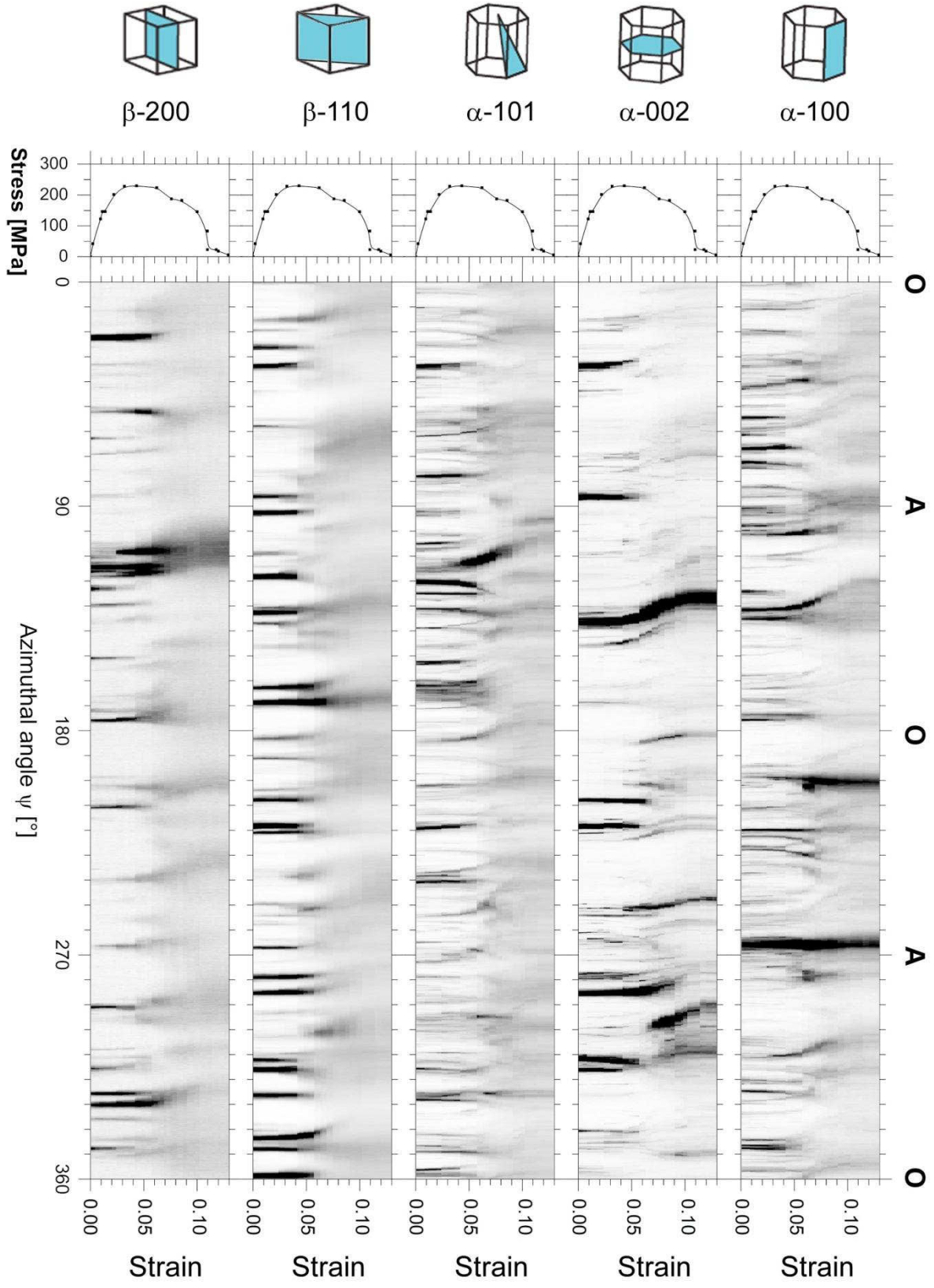

Fig. 4.15. AS-plots for three α- and two β-reflections of the PM alloy at 650°C. The azimuthal angle is indicated at the bottom and axial (A) and orthogonal (O) directions at the top. The plot on the left side corresponds to the macroscopic stress vs. strain curve.

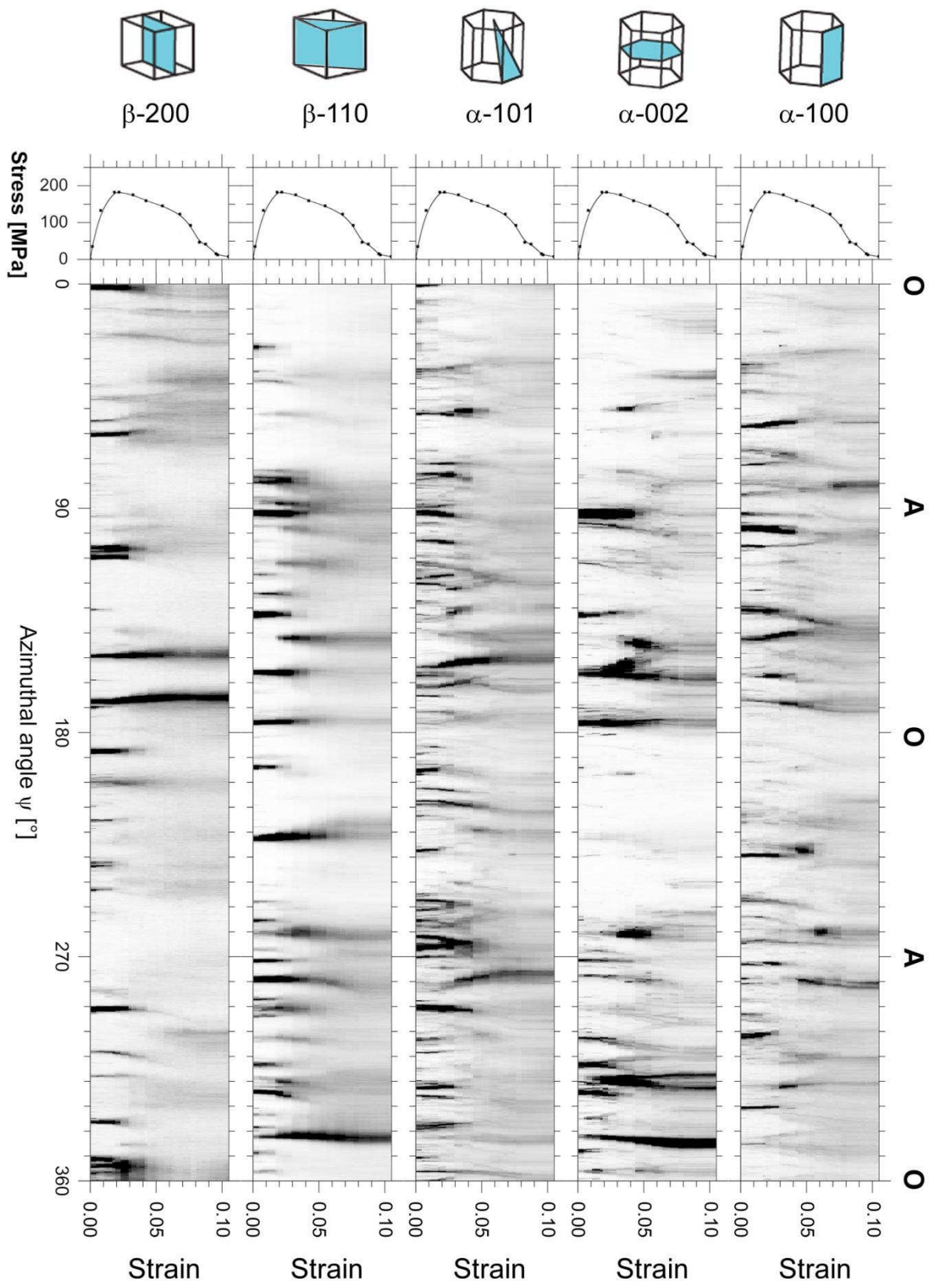

Fig. 4.16. AS-plots for three α- and two β-reflections of the PM alloy at 750°C. The azimuthal angle is indicated at the bottom and axial (A) and orthogonal (O) directions at the top. The plot on the left side corresponds to the macroscopic stress vs. strain curve.

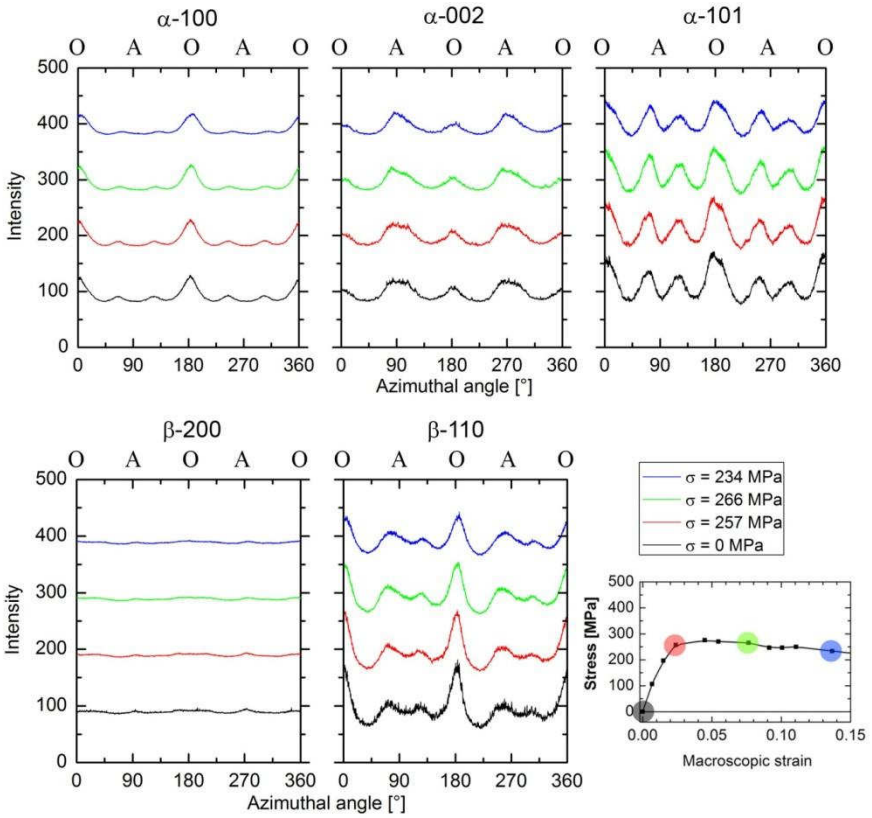

Fig. 4.17. Evolution of the intensity with strain for the IM alloy at 650°C. Three α- and two β-planes are analyzed. Bottom right is plotted the stress vs. strain curve.

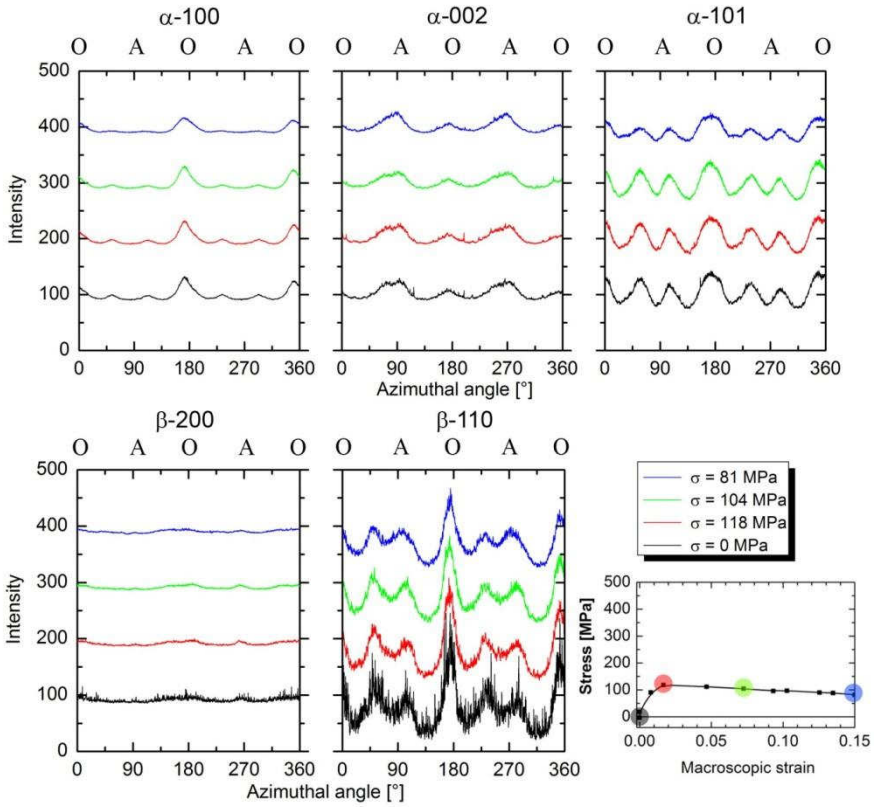

Fig. 4.18. Evolution of the intensity with strain for the IM alloy at 750°C. Three α- and two β-planes are analyzed. Bottom right is plotted the stress vs. strain curve.

The Rietveld analysis using the 2D-images showed R_W (most frequently used agreement factor [110]) ranging from 7.72 % to 10.6 % for the IM alloy. The R_w values for the PM were ≥ 20% for both temperatures, although a reduction was always observed with the progress of deformation. Only at the end of the test at 650°C was possible to obtain a lower value of R_w (%) = 14.2. The diffractograms come always from the same 2D images selected for the intensity evolution curves, i.e., the same stress/strain conditions are analyzed. Fig. 4.19 shows the polar figures orientations referred to the sample axis for the IM alloy. The pole figures are given for the plane perpendicular to the length axis of the sample.

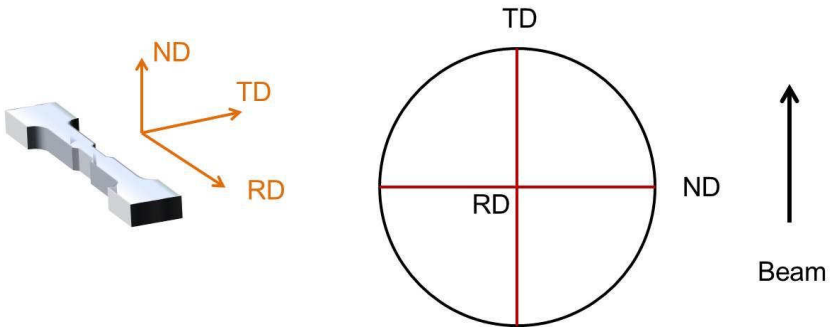

Fig. 4.19. Reconstructed pole figures orientations related to the sample axis.

Fig. 4.20 and Fig. 4.21 present the orientation distribution pole figures. The load direction is perpendicular to these plots and coincides with the radial direction (RD). The right side of these plots shows the logarithmic intensity scale, valid for the α- and β-planes. At 650°C (Fig. 4.20) the initial microstructure (σ = 0 MPa) reveals that α-002 does not lie completely perpendicular in the normal direction and there are also tilted orientation components, although this plane suffers from poor statistics. α-100, oriented orthogonally to the α-002, shows alignments parallel to the normal direction and ~ ± 45° with the transversal direction not completely parallel to the radial direction. β-200 is aligned in parallel, perpendicular (nor completely parallel to the radial direction) and ± 45° to the normal direction. The plastic tensile deformation does not affect significantly the orientation distribution of the α-phase. The β-phase shows that the preferred orientation in the normal direction tends to disappear.

Fig. 4.21 exhibits pole figures for the IM alloy at 750°C. The texture evolution is similar to that observed at 650°C and similar remarks can be applied.

4.1.4 Phase quantification for the unreinforced Ti alloy

Phase quantification is possible using the Rietveld analysis and by metallographic analysis. Using the Rietveld analysis for the IM alloy at 650°C, the vol.% ranged in the

interval [0.77 - 0.79] and [0.21 - 0.23] for the α- and β-phase, respectively. The vol.% for the α-phase was ~ [0.62 - 0.66] and ~ [0.34 - 0.38] for the β-phase at 750°C.

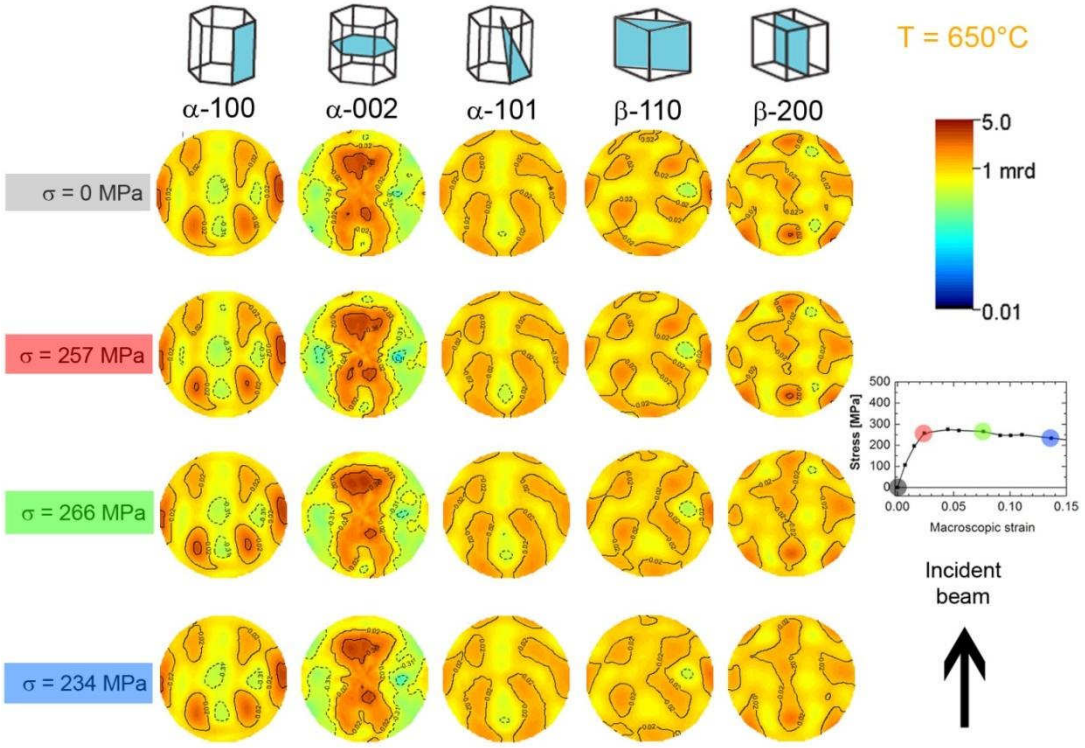

Fig. 4.20. α and β pole figures reconstructed from the in situ synchrotron measurements during different stress values for the IM alloy at 650°C. The load direction is orthogonal to the pole figure plane. The contours are in logarithmic units. The logarithmic scale and the macroscopic stress vs. strain curve are also visible on the right.

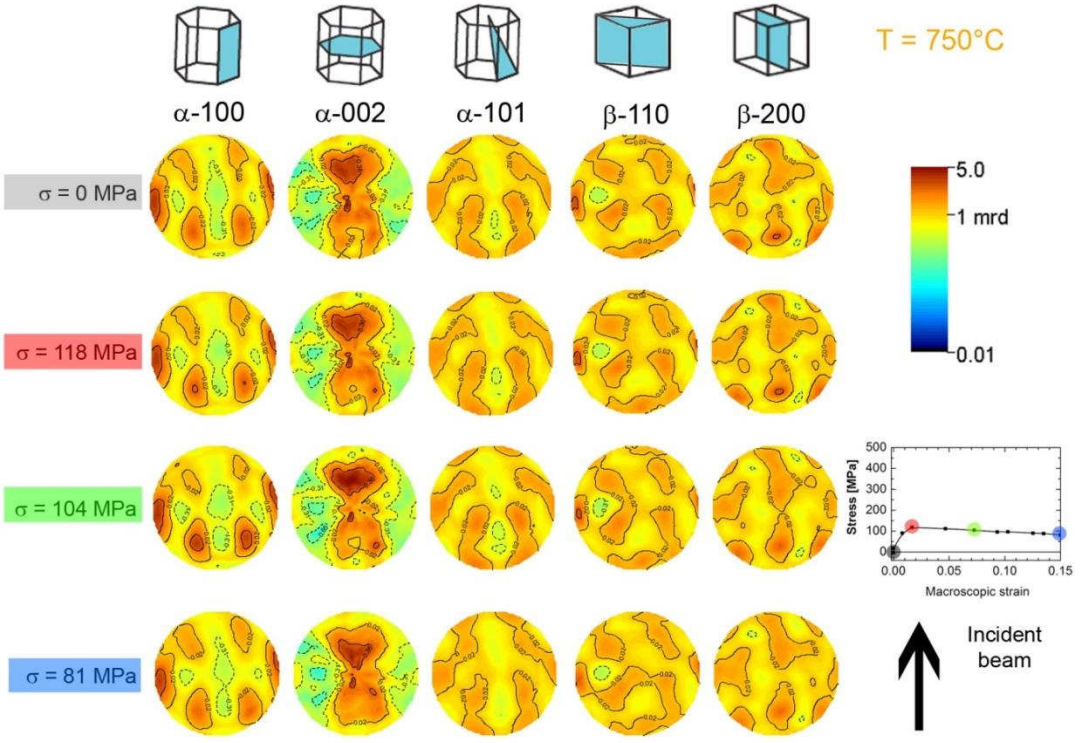

Fig. 4.21. α and β pole figures reconstructed from the in situ synchrotron measurements during different stress values for the IM alloy at 750°C. The load direction is orthogonal to the pole figure plane. The contours are in logarithmic units. The logarithmic scale and macroscopic stress vs. strain curve are also visible on the right.

Phase quantification is also possible using micrographs of the alloys. For this, segmentation of the $\alpha_{primary}$-, $\alpha_{secondary}$- and β-phase was carried out for micrographs obtained by FEG-SEM. Fig. 4.22 a) shows the initial image of the microstructure quenched at 650°C. After the segmentation, the $\alpha_{primary}$ and $\alpha_{secondary}$ can also be separated (see Fig. 4.22 c) and e)). The $\alpha_{primary}$ represents ~ 76 %, $\alpha_{secondary}$ ~ 5 % and β ~ 19 %. At 750°, (see Fig. 4.22 b), d) and f)), the $\alpha_{secondary}$ almost vanishes, showing ~ 1 % with $\alpha_{primary}$ ~ 62% and β ~ 37%.

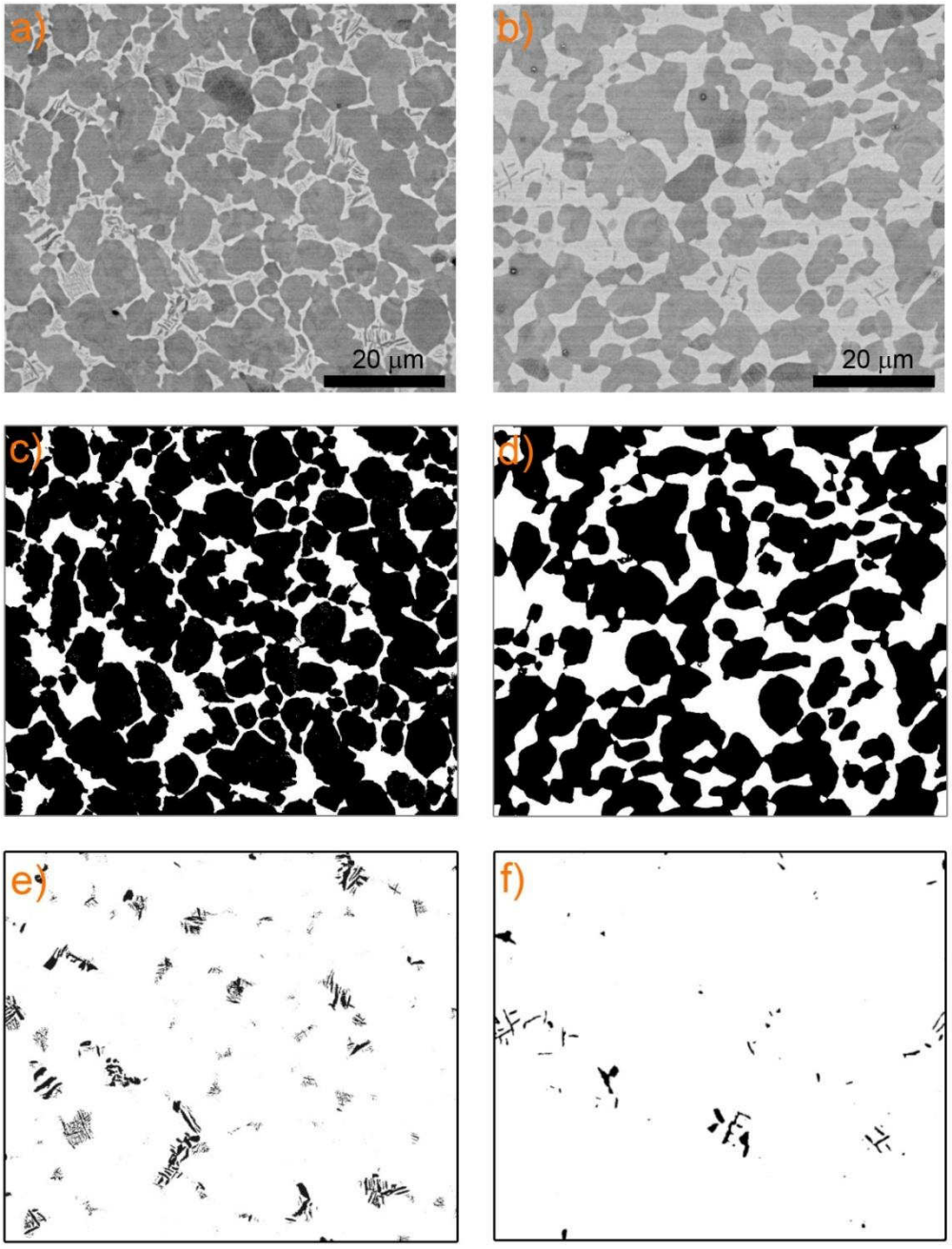

Fig. 4.22. Segmentation of α for the IM alloy: a) and b) show SEM micrographs of the frozen microstructures at 650 and 750°C, respectively. c) and d) show the corresponding segmented $\alpha_{primary}$ (black) and β (white) and e) and f) the segmented $\alpha_{secondary}$ (black).

4.2 Particle Reinforced Lightweight Alloys

4.2.1 Particle reinforced aluminium alloys

Fig. 4.23 a) and Fig. 4.24 a) show the interplanar distances obtained for the $(311)_{Al}$ plane of the different d_0 candidate samples of the 2124 matrix (2124 T7 powders, bulk 2124 T7 and bulk BM 2124 T7), 6061 matrix (6061 T7 powders and bulk 6061 T7) and for the $(202)_{SiC}$ plane of the SiC powders. An isothermal step was applied at 300 ºC for ~ 30 min to analyze the stability of the lattice parameter. There is a marked difference between the 2124 and 6061 powders and their respective bulk samples with (only for the 2124) and without BM (2124 and 6061) both during the heating and the isothermal step. The CTE of the unreinforced matrices and the powders were calculated considering the change of the lattice parameter with temperature during the heating period. Results give 3 - 4 × 10^{-6} K^{-1} and 23 - 27 × 10^{-6} K^{-1} for the SiC powder and the bulk matrix samples, respectively, which are very close to the macroscopic CTE of these materials in the considered temperature range: CTE_{SiC} = 4.7 × 10^{-6} K^{-1} and CTE_{Al} ~ 25 × 10^{-6} K^{-1} [9, 86]. The CTE obtained for the 2124 and 6061 powders is only 16 - 23 x 10^{-6} K^{-1}. This indicates that the matrix powders did not reach the test temperature at the applied heating rate. This can be understood due to the small thermal conductivity of the Al_2O_3 skin of the 2124 and 6061 powders (18 W/mºC [9]). As a consequence, the interplanar distance obtained using the powders does not correspond to the stress-free interplanar distance d_0 at the considered temperature and this disqualifies the 2124 and 6061 powders for this purpose.

There are small differences in the interplanar distance obtained for the bulk samples (< 8 x 10^{-6} strain). However, comparing the microstructure of the matrix of the composites [39, 87], it is clear that the precipitation conditions differ substantially, with a larger volume fraction of dispersoids in the BM composite. Changes in the composition of the matrix due to different precipitation conditions and solute concentration result in different values of stress-free interplanar distances d_0 [97]. Therefore, it is not possible to guarantee that the interplanar distances obtained for the bulk unreinforced matrix samples represent the d_0 for the matrix of the composites. Then, the bulk samples are also disregarded as matrix stress-free reference samples for the stress analysis to avoid misinterpretation of the results.

The SiC powders show reliable CTE values plus they are not affected by compositional changes in the temperature range investigated. Therefore, SiC powders provide adequate d_0 values to calculate the stress evolution during thermal cycling of the SiC phase in the WB and BM composites. For multiphase materials, Withers et al. [111] recommend the

stress calculation in a phase in which the value of d_0 is difficult to estimate, in the present case the Al matrix, by stress balance using the stress calculated for a stable phase, i.e., the SiC particles. This requires that the diffraction gauge volume covers the whole sample to avoid the effect of macro-stresses as well as to have a sufficient volume fraction of the stable phase considered in order to obtain reliable diffraction peaks. Therefore, stress balance was imposed to estimate the stress and strain in the Al matrix at the different temperatures to avoid the introduction of experimental errors due to the uncertainty in the determination of d_0 for the 2124 and 6061 matrices:

$$0 = (1 - f_{SiC})\sigma_{Al}(T) + f_{SiC}\sigma_{SiC}(T) \qquad (4.1)$$

where f_{SiC} is the volume fraction of SiC particles, σ_{Al} and σ_{SiC} are the stresses acting on the Al and SiC phases, respectively.

The d_0 values of the 2124 and 6061 matrices were recalculated using the results obtained from the stress-balance calculations to explore which of the candidate matrix samples (2124 T7 powders, bulk 2124 T7, bulk BM 2124 T7, 6061 T7 powders and bulk 6061 T7) gives closer values. The results are plotted in Fig. 4.23 b) and Fig. 4.24 b) for the 2124 and 6061 matrices, respectively, where only the heating part of Fig. 4.23 a) and Fig. 4.24 a) are included. The recalculated d_0 for the BM and WB 2124 matrix are approximately the same and only those obtained for the BM matrix are shown for clarity. Fig. 4.23 b) and Fig. 4.24 b) show that the d_0 values measured for the bulk sample are very similar to those obtained by stress-balance and the differences should only be taken into account for T > 230°C.

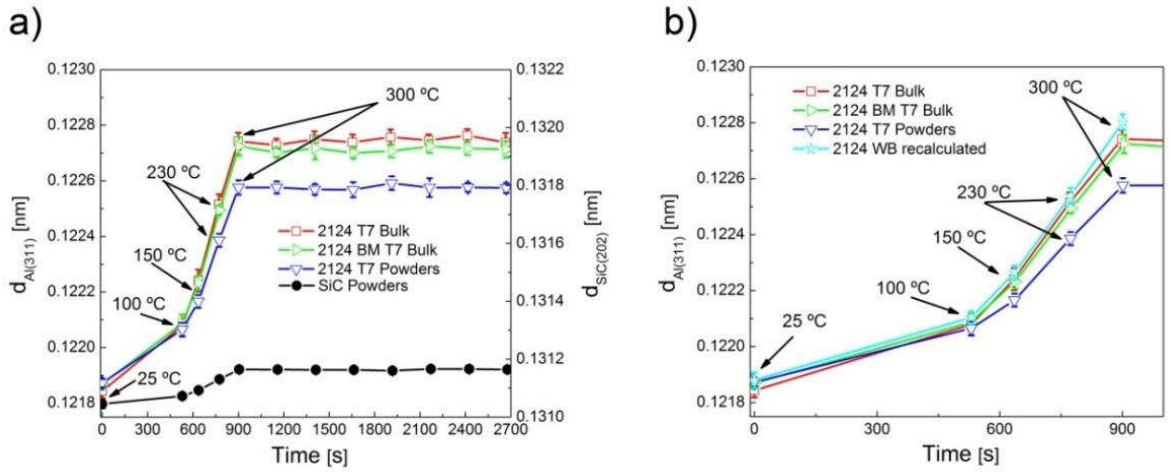

Fig. 4.23. a) Interplanar distances obtained at different temperatures and during isothermal temperature exposure at 300 °C for 2124 bulk and powder samples in T7 condition and for the SiC powders. b) Interplanar distances obtained during heating for the 2124 bulk and powder samples in T7 condition and d_0 for the matrix recalculated using the stress-balance condition (Eq. 4.1).

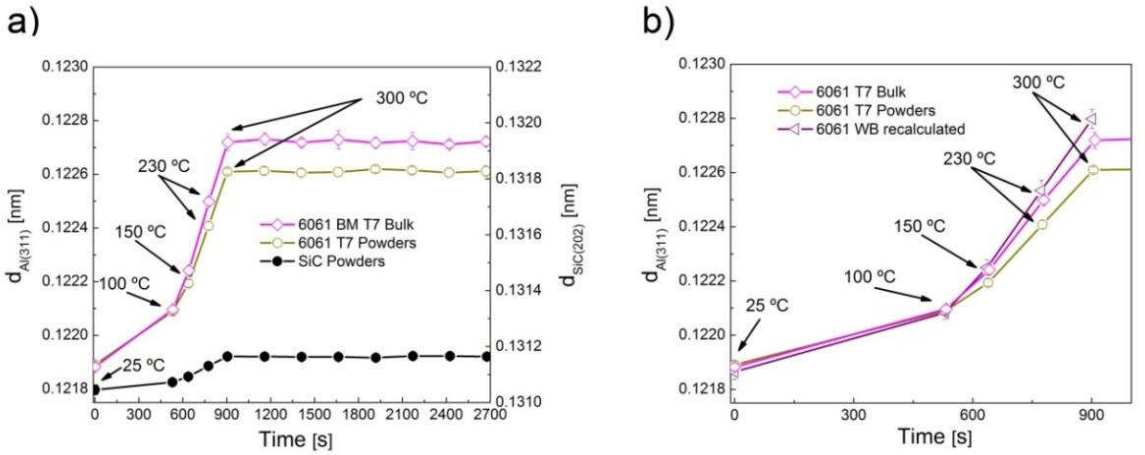

Fig. 4.24. a) Interplanar distances obtained at different temperatures and during isothermal temperature exposure at 300 °C for 6061 bulk and powder samples in T7 condition and for the SiC powders. b) Interplanar distances obtained during heating for the 6061 bulk and powder samples in T7 condition and d_0 for the matrix recalculated using the stress-balance condition (Eq. 4.1)

Fig. 4.25 shows the evolution of the elastic strains obtained for the SiC particles during the in situ diffraction experiments for both the WB and the BM composites. Strains in the axial and radial directions are shown in the top and the bottom diagrams, respectively. The arrows in the diagrams indicate the directions of heating and cooling. The first two thermal cycles from RT to 230 ºC are plotted in the first two diagrams, respectively. The third thermal cycle, also from RT to 230 ºC, shows the same behaviour as the second one and, therefore, it has been omitted to better illustrate the results. The fourth thermal cycle, going from RT to 300 ºC is shown in the 3rd diagram of the figure. The right side of the figure shows the isothermal step carried out at 230 ºC during the third thermal cycle (see Fig. 3.11).

Representative error bars are shown only for one point of each curve to improve the readability of the diagrams. The elastic strains in the SiC phase show negative initial values for both composites indicating that compressive stresses dominate in the SiC particles at RT at the beginning of the experiment, namely after cooling from 300 ºC to RT after the T7 heat treatment. During heating, the strains decrease until a zero strain condition is reached. Above this temperature, the strains become positive indicating an average tensile stress condition. The axial thermal strains in the SiC particles for the BM PRM show a faster increase/decrease with temperature during heating/cooling than the WB composites in both directions and the BM composite in radial direction. As a consequence, the largest thermal strain variations are found for the BM composite in axial direction. The strain at RT at the beginning of the experiment and after the cooling step of each thermal cycle is the same for the corresponding directions of both composites showing that the composites are in the same compressive stress condition after each thermal cycle and that the thermal cycles form a closed loop. Only the

first point at RT of the BM PRM in radial direction seems to be lower (~ - 4 × 10^{-4}) but this may be caused by the larger experimental scatter exhibited by this point.

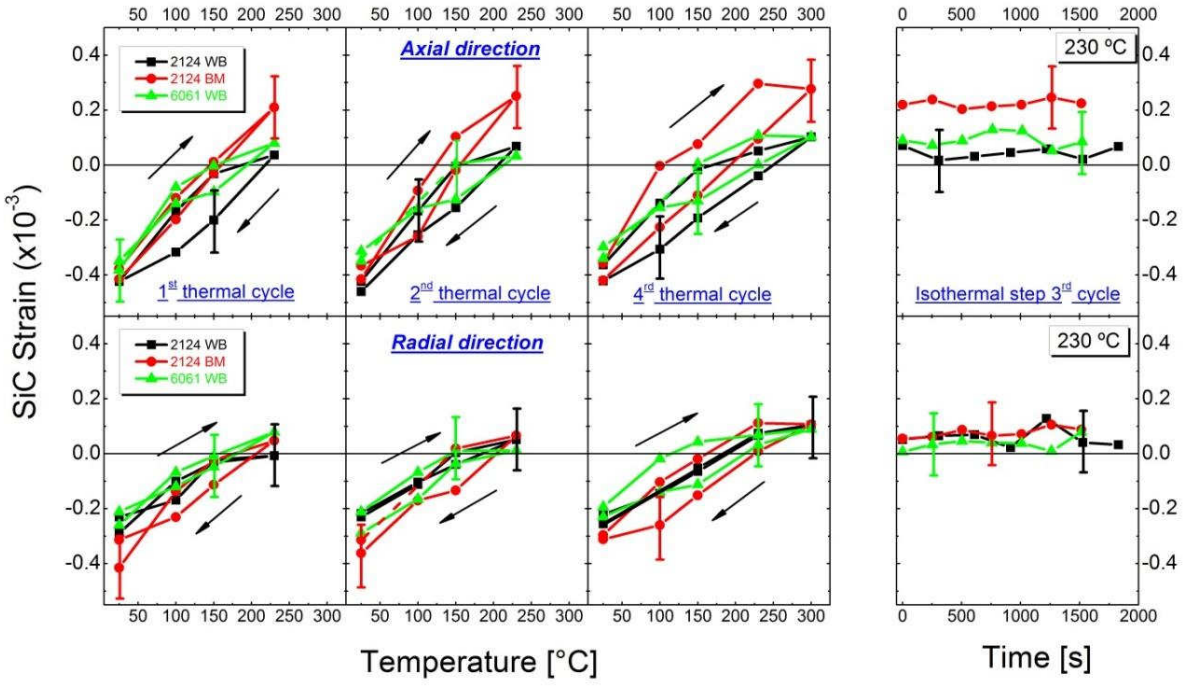

Fig. 4.25. Thermal strains in the SiC phase for the WB and BM PRM in axial and radial directions. The 1st, 2nd and 4th thermal cycles are shown in the first three diagrams, respectively. The isothermal process at 230°C belonging to the 3rd thermal cycle is shown on the right. Typical error bars for every thermal cycle are indicated.

The axial and radial stresses in the SiC phase calculated from the elastic strains (Fig. 4.25) using Eq. (3.2) are shown in Fig. 4.26 a) for the WB and the BM composites. Fig. 4.26 b) shows the stresses in the Al matrix assuming stress balance Eq. (4.1). For the SiC phase, stresses show a qualitative behaviour similar to the elastic strains of Fig. 4.25.

The stresses in the Al phase of all composites show positive initial values indicating that the aluminium matrices present average tensile residual stresses at the beginning of the heating/cooling loop. During heating, stresses decrease, reach zero and then become negative until a maximum compressive stress condition is obtained at 230 ºC. While in the radial direction all composites show a similar behaviour, with a maximum compressive stress ~ - 25 MPa, the maximum compressive stress reached in the axial direction is ~ - 10, - 20 and ~ - 40 - 50 MPa for the WB 2124 and WB 6061, and BM 2124 composites, respectively. These stresses remain roughly constant after heating up to 300 °C and during the isothermal step at 230 °C.

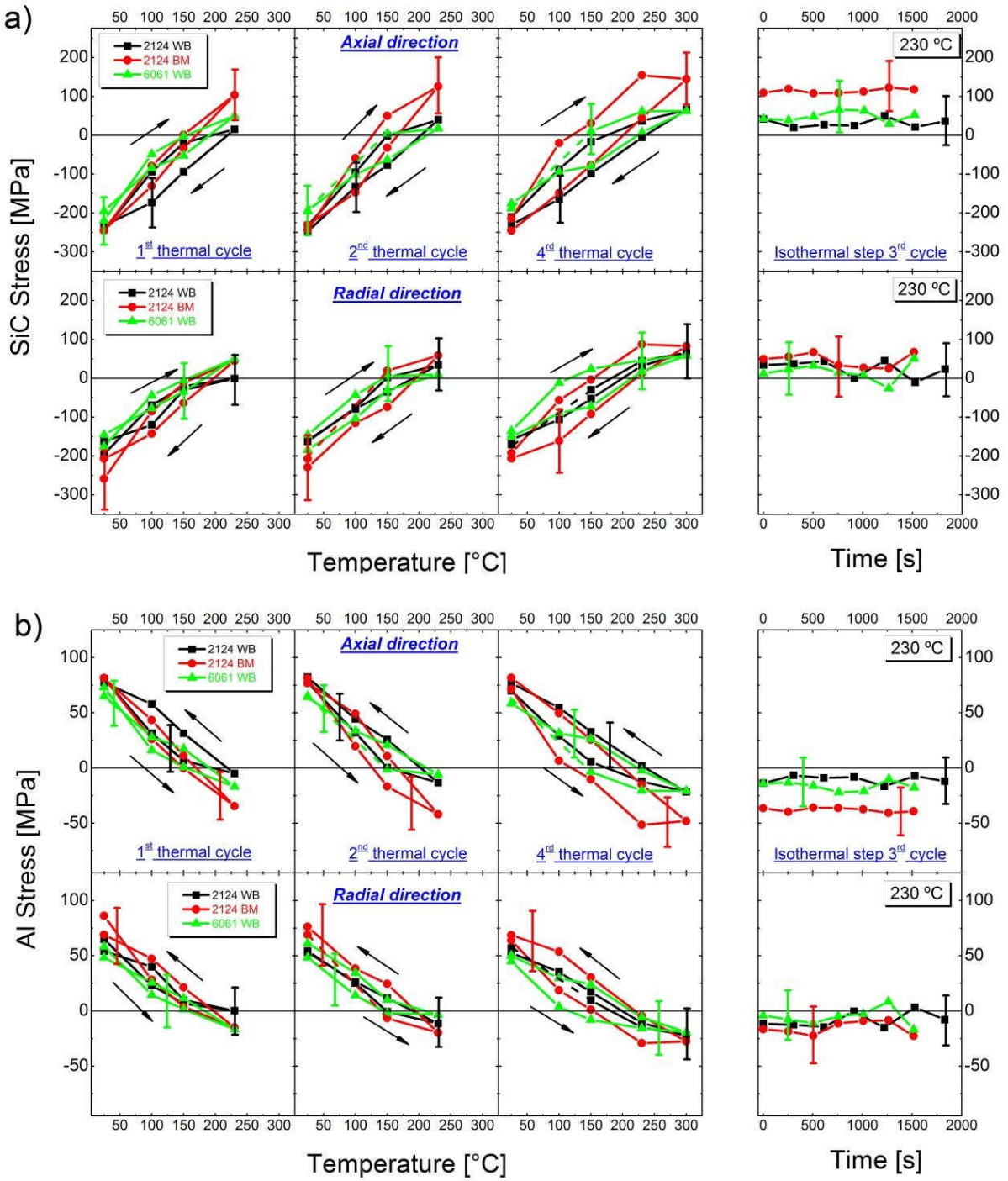

Fig. 4.26. Thermal stresses generated during thermal cycling in the axial and radial directions for all PRM: a) in the SiC particles, and b) in the Al matrix of the 2124 and 6061 alloys.

4.2.2 Particle reinforced titanium alloys

The engineering stress vs. strain curves obtained for the Ti-based PRM are plotted in Fig. 4.27. An initial linear response is observed at 750°C for both composites, followed by a strain hardening period until the maximum stress is reached. Subsequently, softening takes place at 750°C and 850°C. There is no significant difference in strength between the 12 and 20 vol.% PRM, but the PRM with 12 vol.% TiC particles shows ~ 15 - 20% higher ductility.

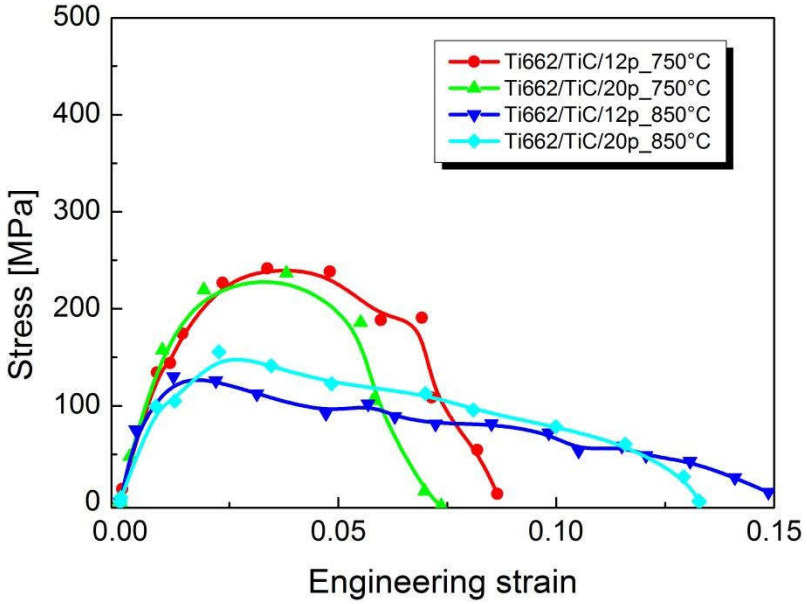

Fig. 4.27. Engineering stress vs. strain curves for Ti662/TiC/12p and Ti662/TiC/20p under tensile loading at 750°C and 850°C.

Similarly to the unreinforced alloys, different d vs. $\sin^2 \psi$ plots were plotted for the α-phase at 750°C to estimate d_0. Fig. 4.28 shows the α-100 plots for both PRM at 750°C. Ti662/TiC/12p is shown on the left and Ti662/TiC/20p on the right. Plots corresponding to α-reflections α-002, α-101 α-102, α-110, α-103, α-112 and α-201 at 750°C are shown in the Appendix. The fast plastification of α-phase at 850°C for both PRM prevents the use of the $\sin^2 \psi$ method and the d-spacing obtained at the beginning of the tensile test is used as d_0. The β- and TiC-phases show either poor fittings (low R^2 values) or large uncertainty in the position of the intersection point for both PRM and temperatures. Therefore, the beginning of the tensile tests was used as d_0 and the strains were studied from an incremental point of view.

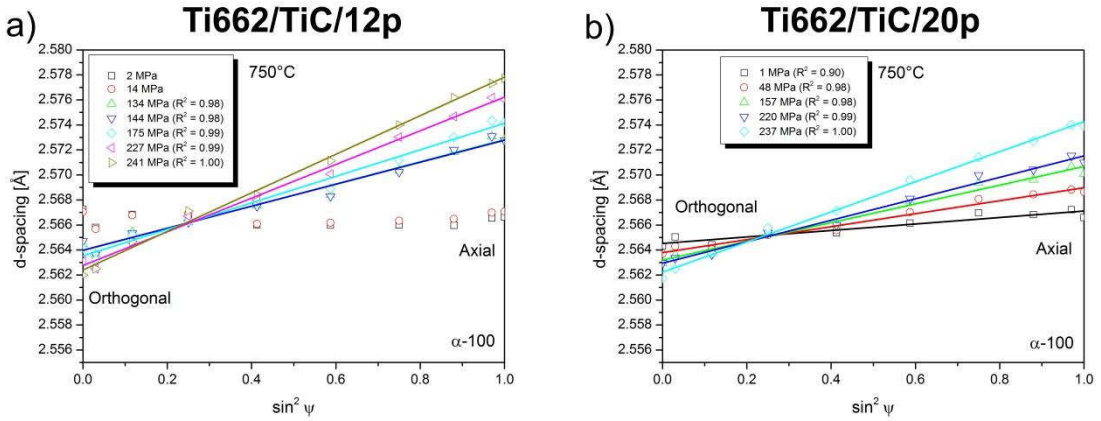

Fig. 4.28. d vs $\sin^2 \psi$ plots with the corresponding linear fits at different tension stresses for the α-100 Ti reflection at 750°C in a) Ti662/TiC/12 and b) Ti662/TiC/20p PM. R^2 values are also indicated.

In Table 4.2 are included the different d_0 used for the α-strain evaluation at 750°C for both PRM. Only those reflections that show a strain evolution with applied load are shown.

The intersection point was selected as stress-free interplanar distance d_0 and used for the elastic strain evaluation of the corresponding crystallographic plane.

(hkl)	Ti662/TiC/12p_750°C	Ti662/TiC/20p_750°C
α-100	2.5663±0.0009	2.5651±0.0005
α-002	2.3747±0.0005	X
α-101	2.2576±0.0004	2.2572±0.0009
α-102	1.7429±0.0000	1.7426±0.0000
α-110	1.4818±0.0007	1.4810±0.0008
α-103	1.3470±0.0002	1.3470±0.0003
α-112	1.2570±0.0002	1.2560±0.0001
α-201	1.2387±0.0000	1.2380±0.0001

Table 4.2. d_0 values determined using the $\sin^2 \Psi$ method for different α-reflections of the reinforced Ti PRM at 750°C.

The elastic strains for the α-, β- and TiC-phases are shown in Fig. 4.29, Fig 4.30 and Fig. 4.31, respectively. The diagrams at the top correspond to the axial, while the diagrams at the bottom to the orthogonal strains. The upper plots for every graph correspond to the engineering stress vs. strain curves for the Ti662/TiC/12p (left) and Ti662/TiC/20p (right). As commented in 4.1.3, and for readability, the error bar corresponds to the maximum error and was obtained for the plane with the same color. Analyzing the initial α-strains in axial direction, a zero initial stress condition is found at 750°C for both PRM. Final strains for α- and β-phases are also in the same level as the initial. Because of the experimental scatter, initial and final strains differ for the TiC. In general and similarly to the unreinforced titanium alloys, α-100 and α-110 show the highest strains, followed by α-101 and α-201 and finally α-103, α-102, α-112 and α-002 in the same level. The sequence for the β-phase is analogous, with the highest strains for β-200 and β-110, β-211 and β-220 in the same range.

At 750°C and for both composites, the α- and TiC-phases take an increasing portion of load until an applied stress of ~ 240 MPa. On the other hand, the β-phase reaches a maximum strain in the early stages of deformation and remains approximately constant with strains between $[0.5 - 1.5] \times 10^{-3}$ for Ti662/TiC/20p and with a slight increment for the other composite, i.e. $[1.5 - 2.5] \times 10^{-3}$. The maximum α-strain obtained for the Ti662/TiC/12p are: α-002, α-102 and α-103 ~ 2.5×10^{-3}, α-110 ~ 4×10^{-3} and ΔTiC ~ $[0.5 - 2] \times 10^{-3}$. And for Ti662/TiC/20p: α-102 and α-103 ~ 2×10^{-3}, α-110 ~ 4×10^{-3} and ΔTiC ~ $[0.5 - 1.5] \times 10^{-3}$, similar to the other composite.

The strains in α- β- and TiC-phases increase simultaneously until an applied stress of ~ 70 MPa for the Ti662/TiC/12p at 850°C. A subsequent increment of the external load does

not provoke changes and the strains remain constant until an external load of ~ 70 MPa is achieved again during strain softening. A progressive reduction of these strains is then observed. Maximum strains are: α-002 ~ 1×10^{-3}, α-110 and α-100 ~ 2.5×10^{-3}, β-reflections ~ [0.5 - 1] $\times 10^{-3}$ and for the TiC ~ 1.5×10^{-3}. The strains for the three phases increase rapidly from the beginning in the Ti662/TiC/20p, with a subsequent reduction of the hardening slope for the α- and TiC-phase until the maximum load, while the β-strains remain constant with β-200 ~ 1.5×10^{-3} and the other β-planes ~ [0.5 - 1] $\times 10^{-3}$.

The orthogonal direction plots are shown at the bottom in Fig. 4.29, Fig 4.30 and Fig. 4.31 for α-, β- and TiC-phase, respectively. The strains are negative for all α- and TiC-planes owing to the Poisson' effect. Final orthogonal strains are similar to the initial state if the experimental scatter is considered. Only the β-phase shows a dissimilar behaviour because remains practically equal to zero (Ti662/TiC/20p) or close (see Ti662/TiC/12p).

Fig. 4.32 shows the Debye-Scherrer diffraction rings for the Ti662/TiC/12p at 750°C. Four sectors are visible and the reflections are indicated in Fig. 3.24 b). The initial image shows slightly discontinuous rings for the α- and β-phases and a "spotty" morphology for the TiC. The rings of the Ti-phases become completely continuous at the end of the test while the TiC rings remain dotted. Similar behaviour undergoes the Ti662/TiC/12p at 850°C (see Fig. 4.33) and the Ti662/TiC/20p at both temperatures (Fig. 4.34 and Fig. 4.35).

The α-100, α-002, α-101 and β-200, β-110 are selected to study their microstructural evolution during deformation. The Ti662/TiC/12p plots at 750°C are shown in Fig. 4.36. The initial pattern shows some diffracted spots for the α- and β-phases. During the pseudo elastic regime (up to ~ 230 MPa), these spots evolve as vertical bands for the α- and β-phases. Above 230 MPa, the α-bands move slightly to the right or left sides, changing the azimuthal angles with no apparent preferred orientation, and spreading in some cases, resulting in a final pattern where most of the high intensity points vanish. The diffraction bands corresponding to the β-planes, above 230 MPa, spread rapidly changing the semi-continuous distribution to a homogeneous pattern. These results are applicable for the Ti662/TiC/20p (Fig. 4.37) at 750°C and for the tests at 850°C (Fig. 4.38 and Fig. 4.39).

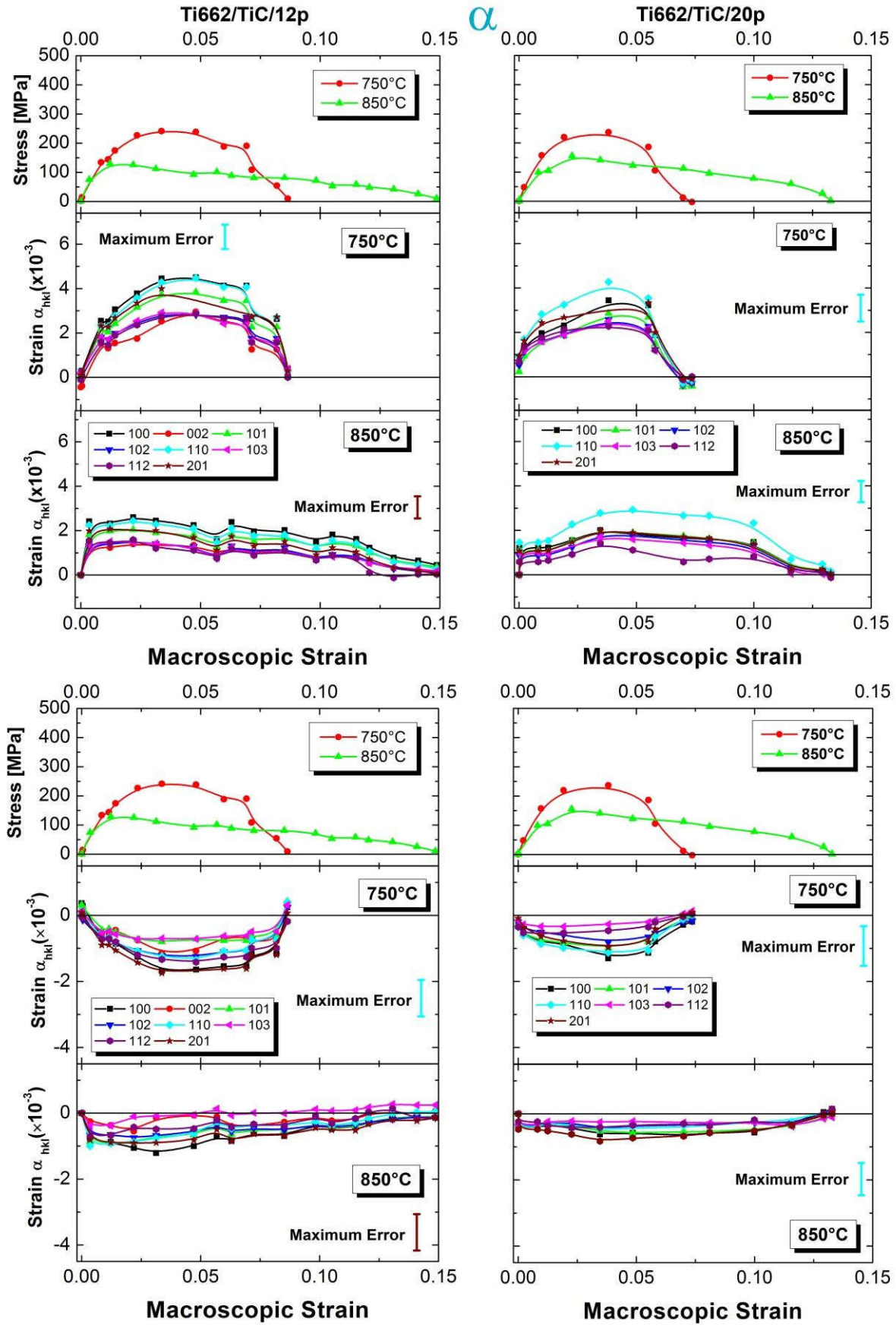

Fig. 4.29. Lattice strain evolution for the α-reflections in the axial (top) and orthogonal directions (bottom) at 750°C and 850°C for the Ti662/TiC/12p (left) and Ti662/TiC/20p (right) during tensile loading.

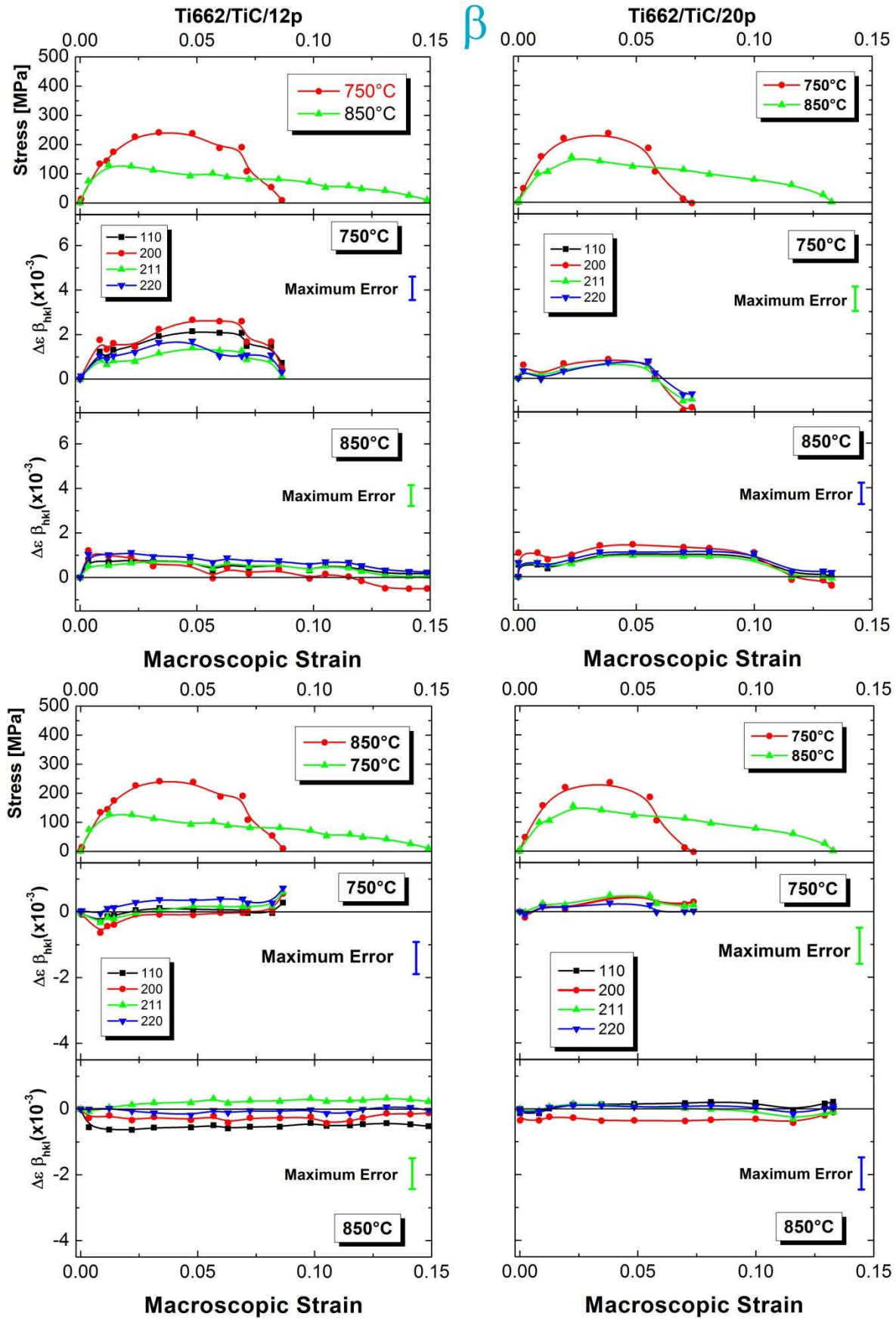

Fig 4.30. Lattice strain evolution for the β-reflections in the axial (top) and orthogonal directions (bottom) at 750°c and 850°C for the Ti662/TiC/12p (left) and Ti662/TiC/20p (right) during tensile loading.

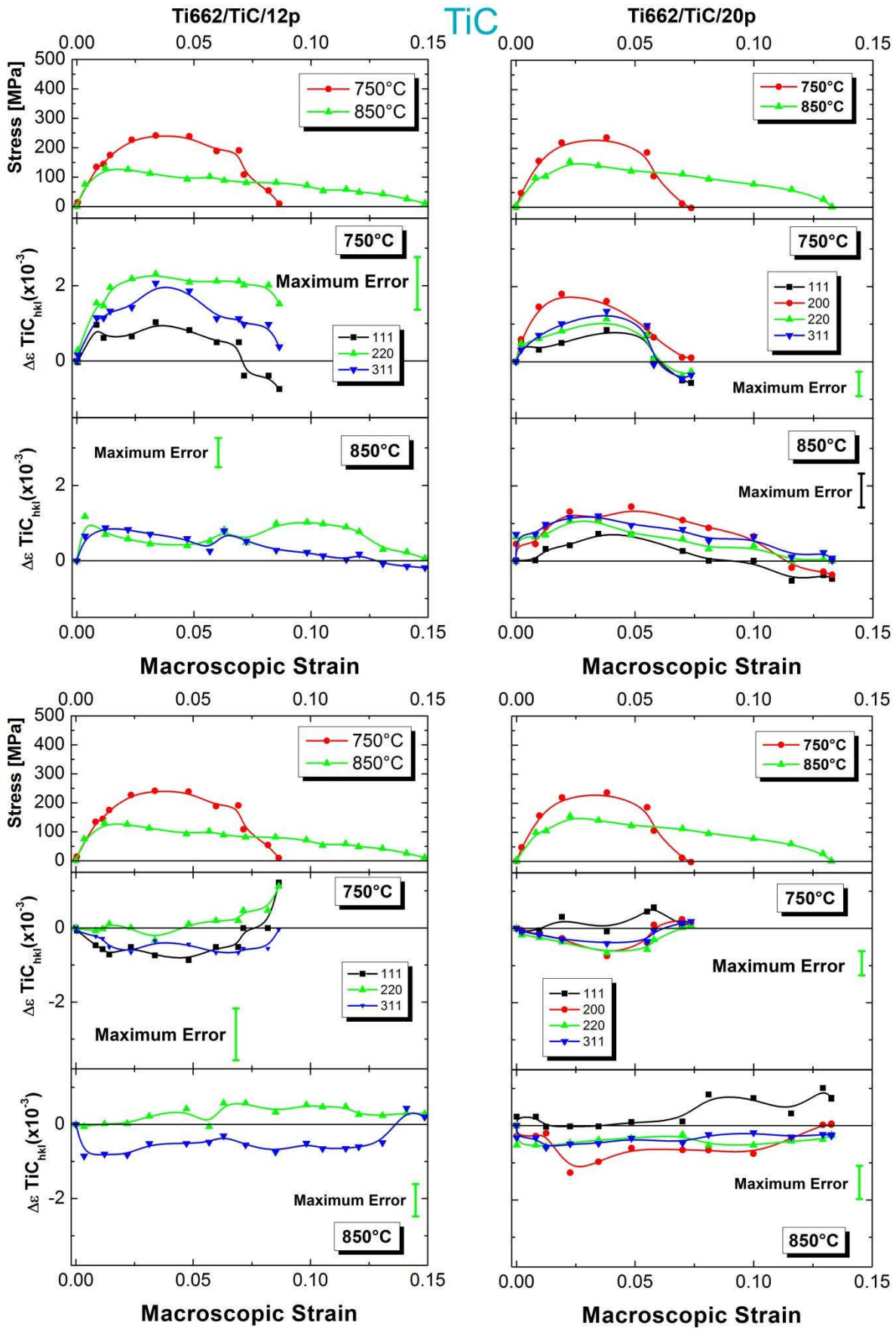

Fig. 4.31. Lattice strain evolution for the TiC-reflections in the axial (top) and orthogonal directions (bottom) at 750°C and 850°C for the Ti662/TiC/12p (left) and Ti662/TiC/20p (right) during tensile loading.

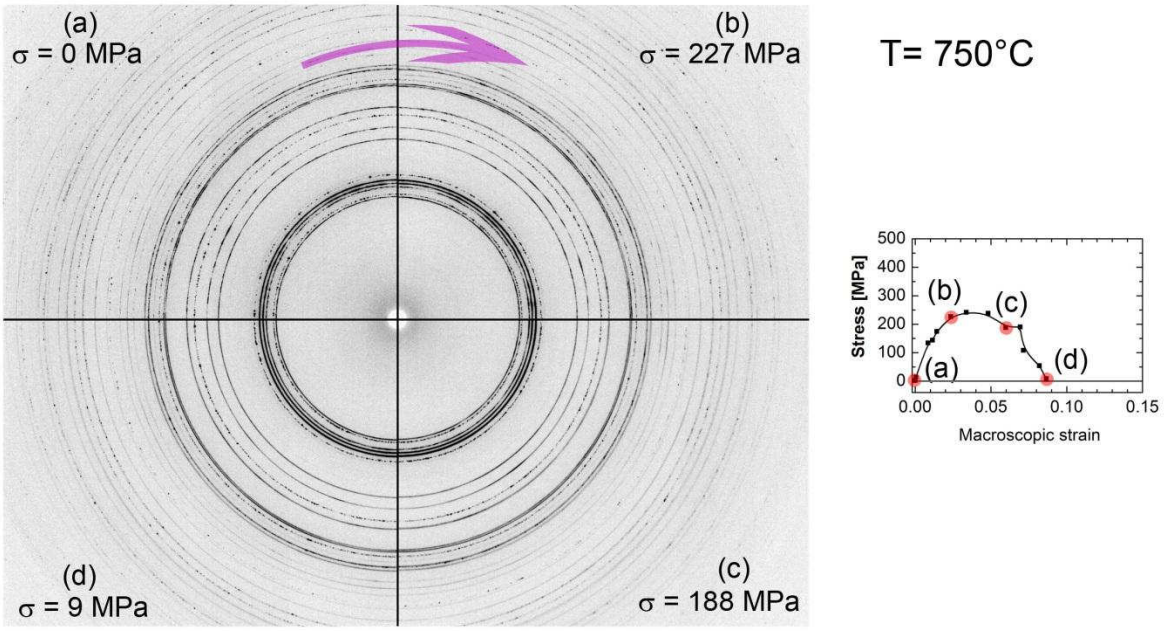

Fig. 4.32. Representative portions of the acquired diffraction rings assembled with four sectors for the Ti662/TiC/12p at 750°C. Corresponding α-, β- and TiC-planes are indicated in Fig. 3.24 b). On the right, the macroscopic stress vs. strain curve is plotted.

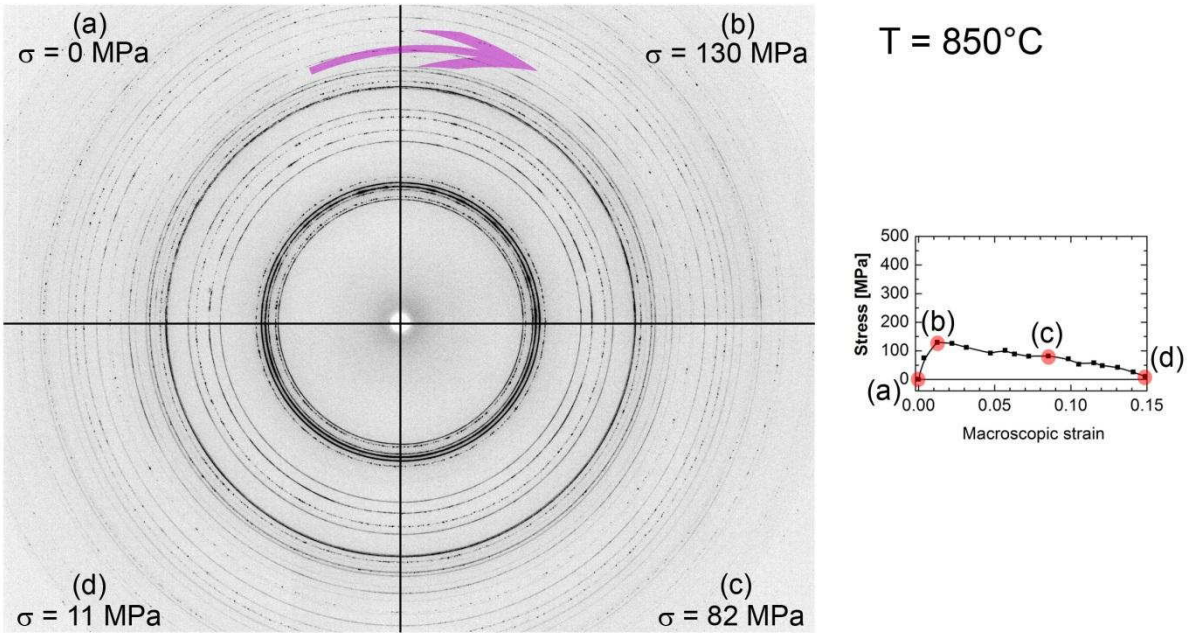

Fig. 4.33. Representative portions of the acquired diffraction rings assembled with four sectors for the Ti662/TiC/12p at 850°C. Corresponding α-, β- and TiC-planes are indicated in Fig. 3.24 b). On the right, the macroscopic stress vs. strain curve is plotted.

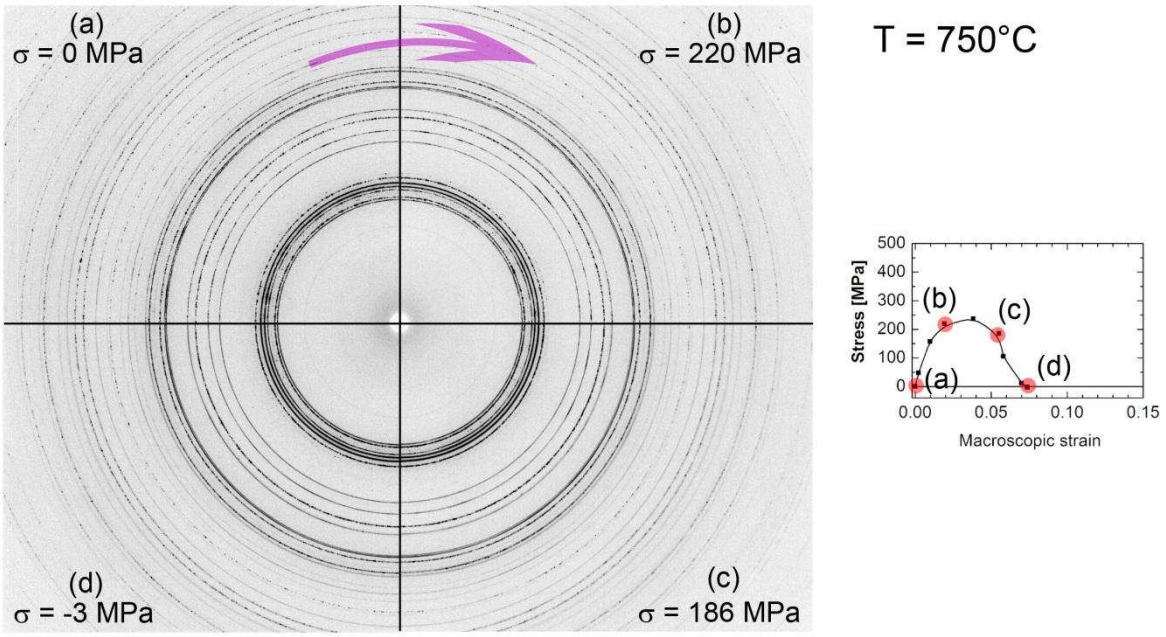

Fig. 4.34. Representative portions of the acquired diffraction rings assembled with four sectors for the Ti662/TiC/20p at 750°C. Corresponding α-, β- and TiC-planes are indicated in Fig. 3.24 b). On the right, the macroscopic stress vs. strain curve is plotted.

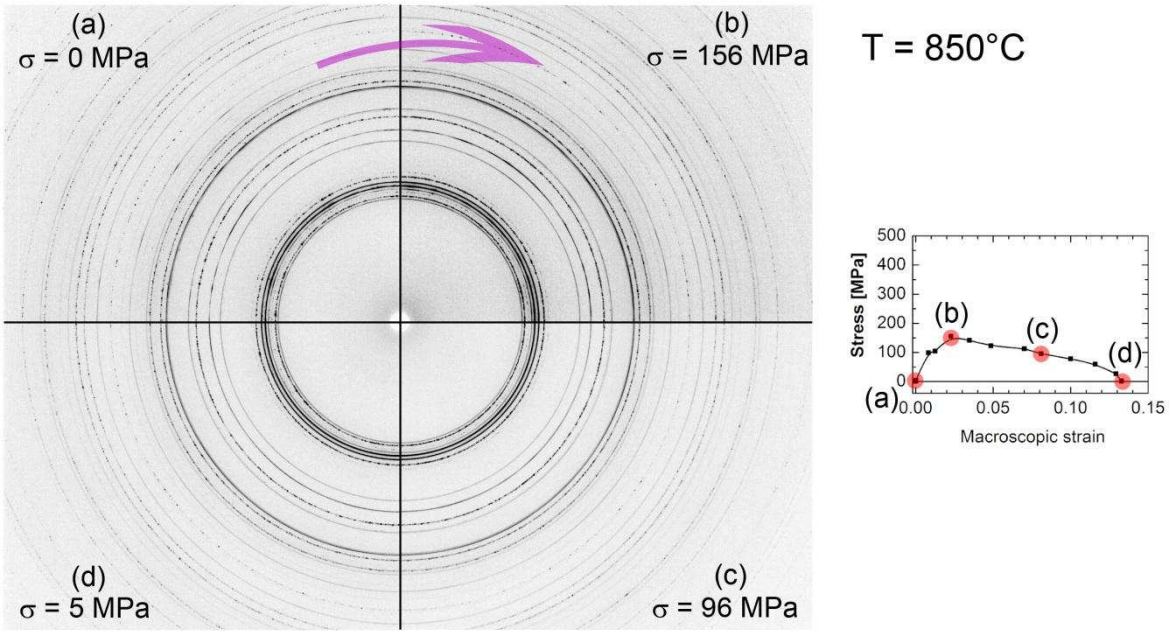

Fig. 4.35. Representative portions of the acquired diffraction rings assembled with four sectors for the Ti662/TiC/20p at 850°C. Corresponding α-, β- and TiC-planes are indicated in Fig. 3.24 b). On the right, the macroscopic stress vs. strain curve is plotted.

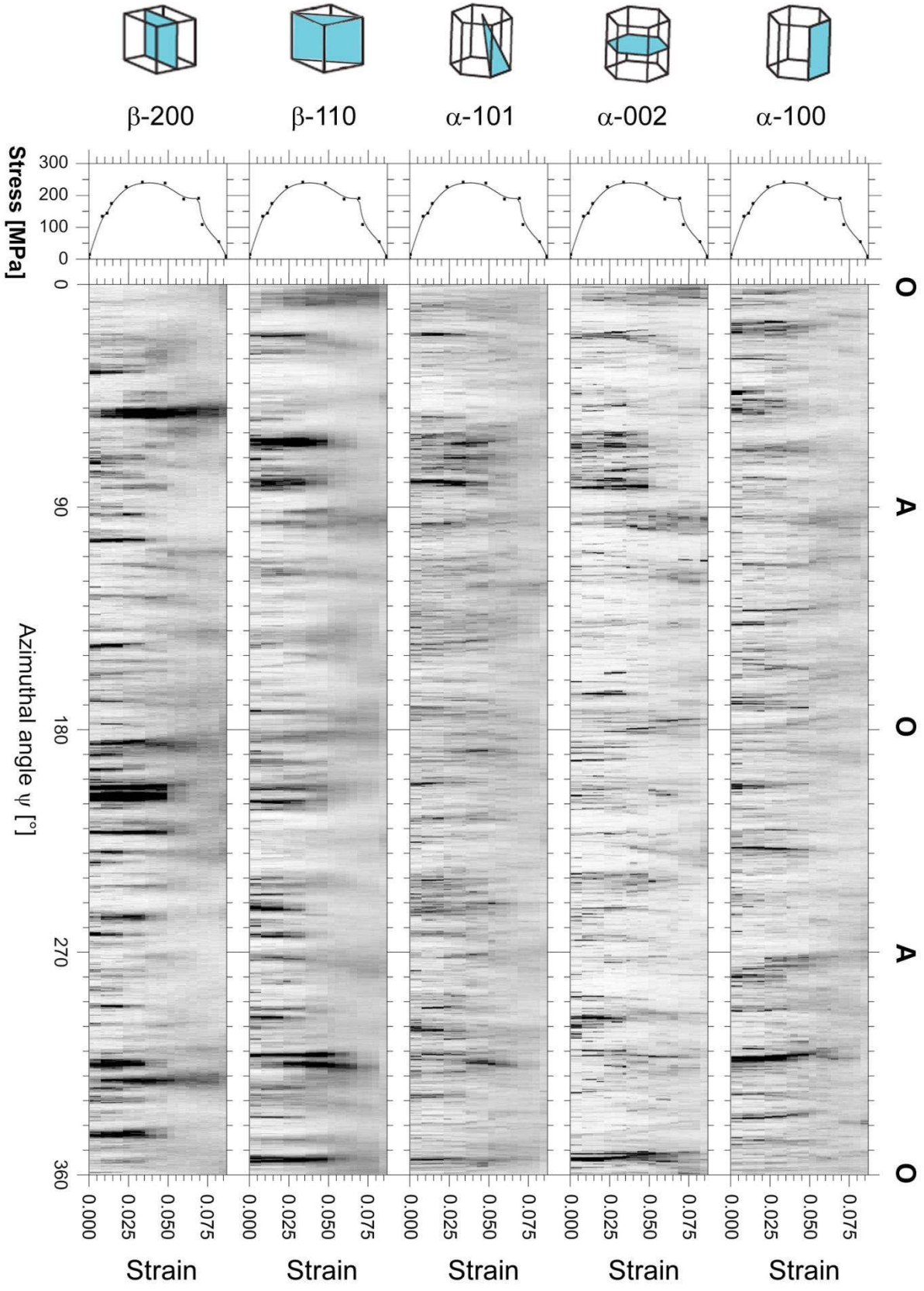

Fig. 4.36. AS-plots for the α-100, α-002, α-101 and β-110, β-200 at 750°C for the Ti662/TiC/12p. The azimuthal angle is indicated on the bottom and axial (A) and orthogonal (O) directions on top. Left side plot corresponds to the macroscopic stress vs. strain curve.

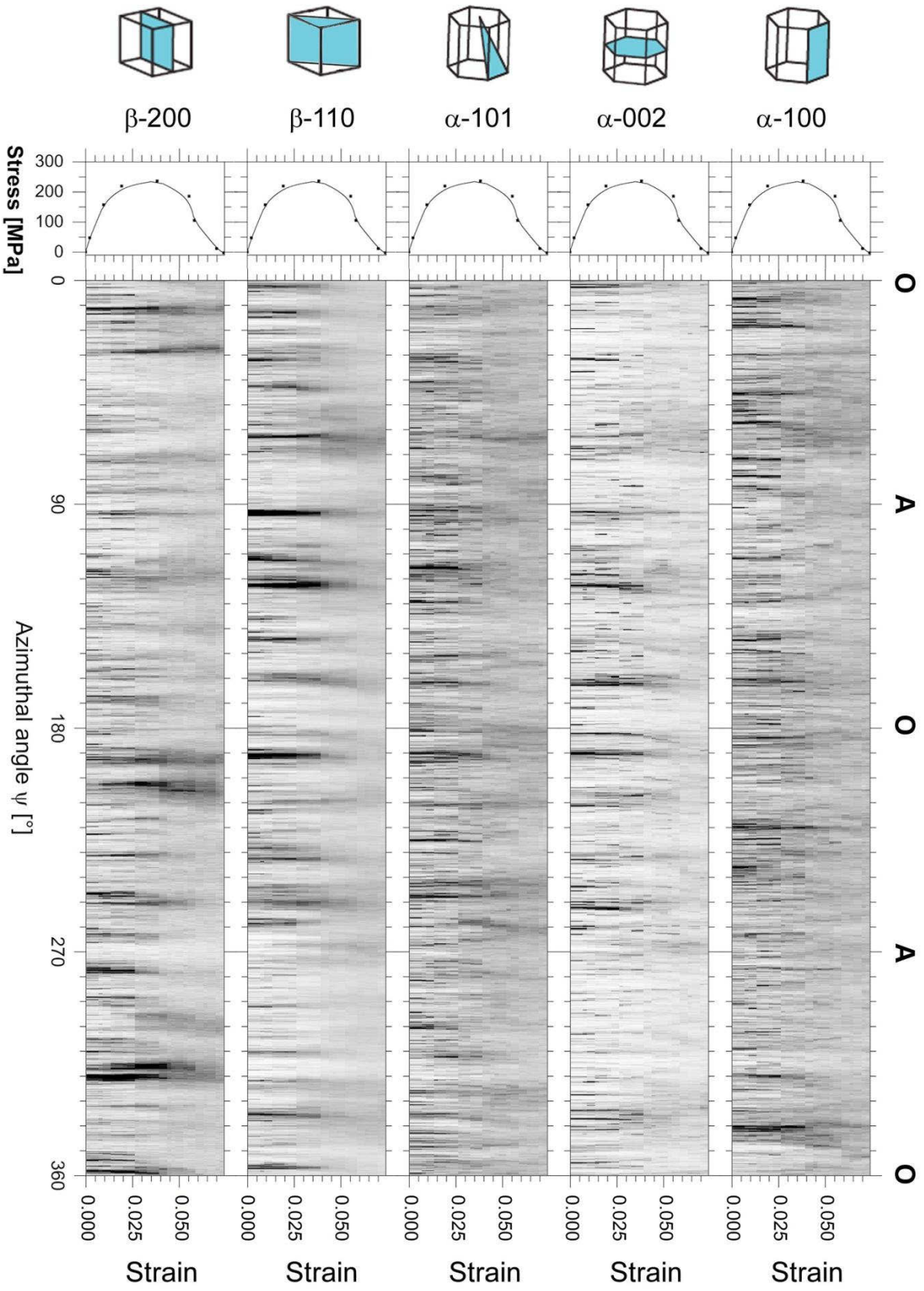

Fig. 4.37. AS-plots for the α-100, α-002, α-101 and β-110, β-200 at 750°C for the Ti662/TiC/20p. The azimuthal angle is indicated on the bottom and axial (A) and orthogonal (O) directions on top. Left side plot corresponds to the macroscopic stress vs. strain curve.

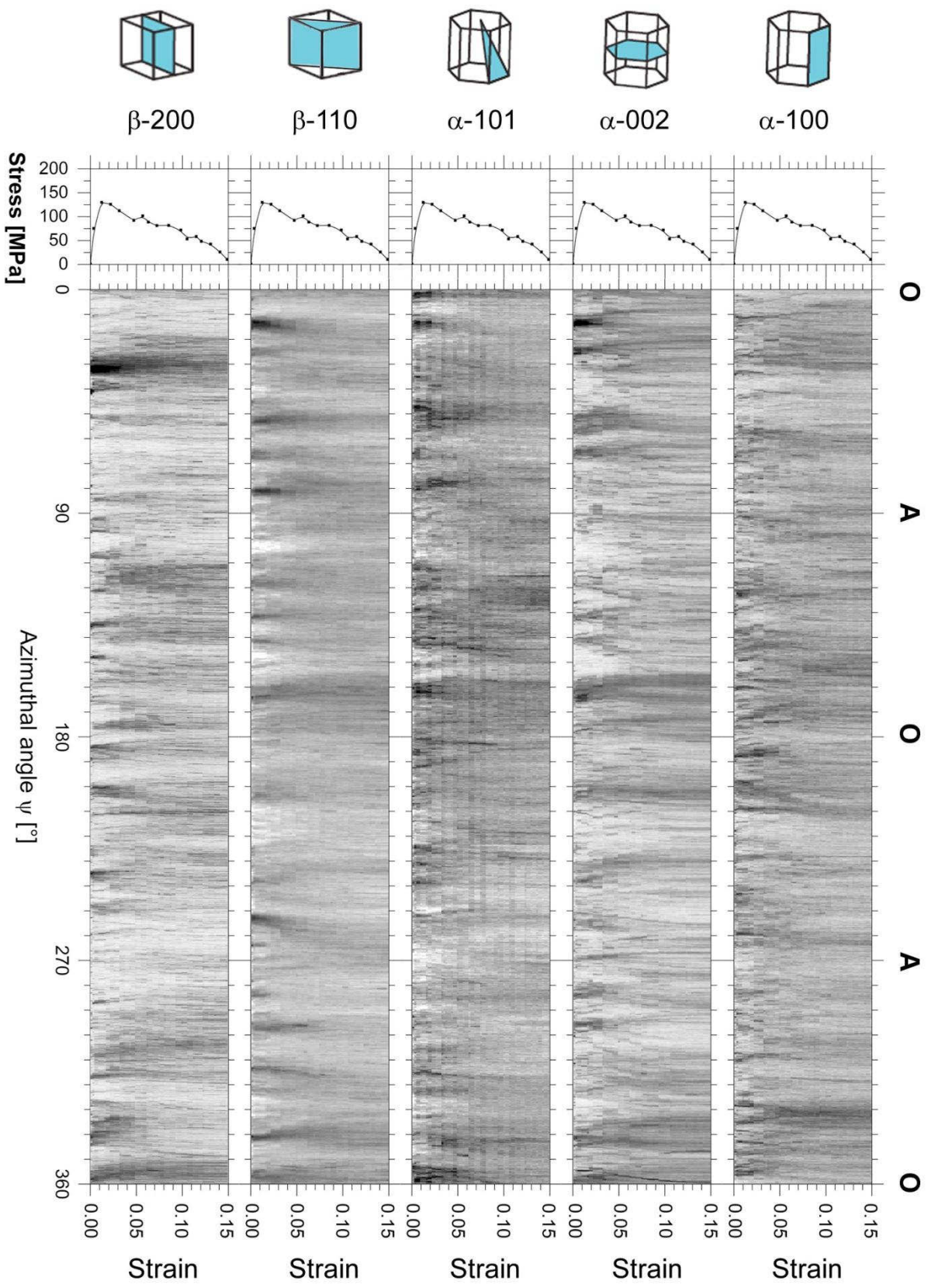

Fig. 4.38. AS-plots for the α-100, α-002, α-101 and β-110, β-200 at 850°C for the Ti662/TiC/12p. The azimuthal angle is indicated on the bottom and axial (A) and orthogonal (O) directions on top. Left side plot corresponds to the macroscopic stress vs. strain curve.

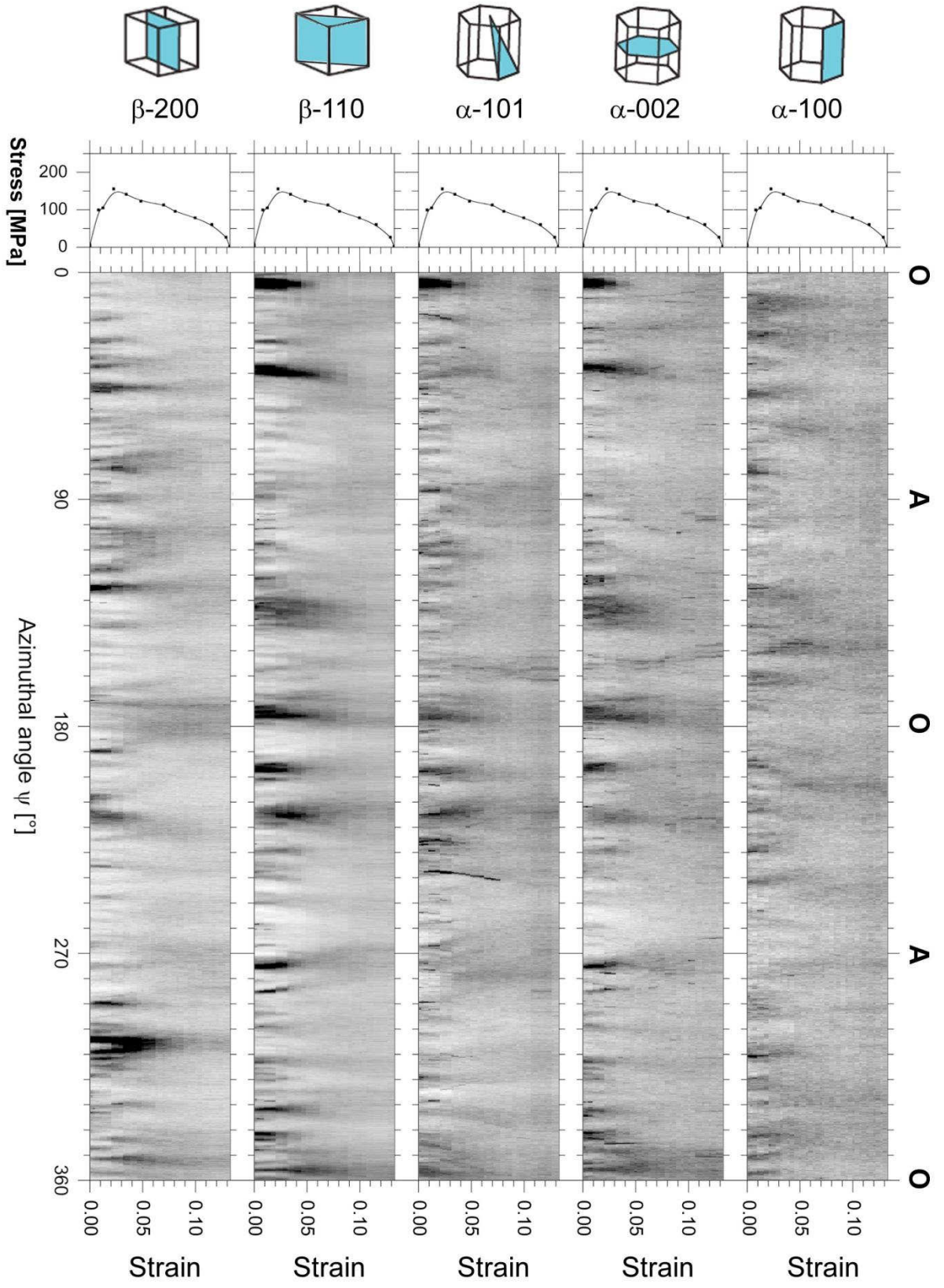

Fig. 4.39. AS-plots for the α-100, α-002, α-101 and β-110, β-200 at 850°C for the Ti662/TiC/20p. The azimuthal angle is indicated on the bottom and axial (A) and orthogonal (O) directions on top. Left side plot corresponds to the macroscopic stress vs. strain curve.

5 Interpretation and Discussion of Results

5.1 Load partition in the AlSi12 and AlSi10Cu6Ni2 alloys

The Si-311 reflection was selected to analyze the load partition in both alloys since it is weakly affected by intergranular strains [97]. Fig. 5.1 shows the stresses calculated using Eq. 3.2 and the elastic constants indicated in 3.4.5 up to the maximum external stress for the AlSi12 (left) and 1062 (right) alloys.

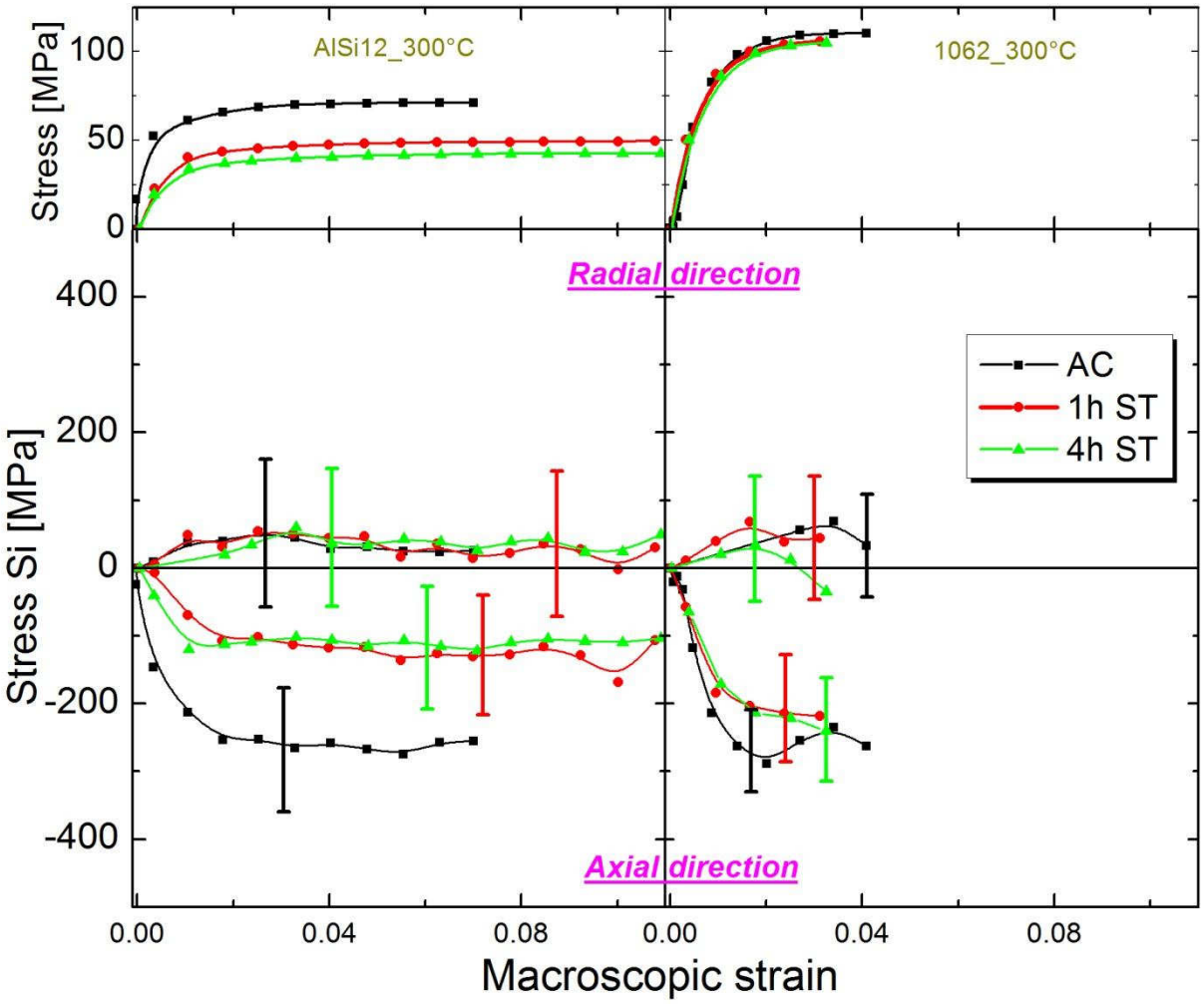

Fig. 5.1. Stress evolution for the Si-311 reflection in AC, 1h and 4h ST for ASi12 (left) and 1062 at 300°C (right). The evolution is shown up to the maximum external stress for each ST condition.

An incremental analysis between maximum and minimum stresses during the deformation period can be done to assess the total load bearing capability of Si. During loading, axial stresses in Si increase as a function of the applied strain with different slopes in both alloys depending on the ST time. Thus, the AC condition (i.e. 0h ST) shows a steeper stress increase (for both alloys) than the other ST conditions for the same applied strain. This indicates that the Si in the AC condition is able to carry a larger load portion than after 1h and

4h ST for identical externally applied strains. The load bearing capability of the Si depends on its interconnectivity and morphology [12, 37-38]. This more effective load transfer from the Al-matrix to the 3D Si network in AC condition was proposed in [65] and [67] for compression tests at 300°C for the AlSi12 and the AlSi10Cu5Ni2 alloys, respectively. There, the decrease in the stress carried by the Si after solution treatments was attributed to the spheroidization of the 3D Si network, which is a combined process of disintegration of 3D networks of Si and further rounding of the disconnected particles. This effect is very pronounced for the AlSi12 alloy [12], while the interconnectivity of Si is highly preserved in the AlSi10Cu5Ni2 alloy even after 4h ST [67].

The maximum stress increase found for the Si in the AlSi12 alloy is $\Delta\sigma \sim -250$ MPa for the AC condition and ~ -100 MPa for the 1h and 4h ST conditions. The 1062 alloy shows, in all conditions, a more effective load transfer from the Al-matrix to the Si 3D network than the AlSi12 alloy reflected by the steeper stress increase for the equivalent ST conditions. This difference can be understood taking into account that the 3D network of Si forms a hybrid 3D structure together with intermetallic phases [67]. This results in ~ 24 vol.% fraction of highly interconnected rigid phases whose interconnectivity is highly preserved during the ST [67]. Al_2Cu is one of the intermetallic phases forming these 3D structures of aluminides and Si [64]. Its contribution to the strength of the alloy is reflected by the similar strain slopes for all conditions in axial direction for this phase (Fig. 4.5). The maximum $\Delta\sigma_{Si}$ found for the 1062 alloy is ~ 270 MPa for the AC condition and ~ 250 MPa for the 1h and 4h ST, values in the same range as for the AlSi12 alloy in AC condition. This indicates that the presence of the aluminides does not affect strongly to the load born by the 3D Si network but instead they bear their own portion of load. Asghar et al. [112] reported recently that damage during compression of the AlSi10Cu5Ni2 alloy takes place at $\varepsilon \geq 0.04$. The results obtained in this work for the 1062 alloy show that the maximum load born by the Si 3D network is achieved at $\varepsilon \sim 0.04$ for all ST conditions, with subsequent stress decrease. The Al_2Cu-phase is one of the firsts to fail since the lattice strains decrease rapidly in the axial direction when the external stress is maximum for all ST conditions (see Fig. 4.5).

The stress evolution in Al was calculated using Eq. 2.3 and it is shown in Fig. 5.2. Only the AlSi12 alloy allowed this analysis since the load born by the aluminides in 1062 is unknown due to the absence of strains for some of the intermetallic phases and their respective elastic constants at high temperature are unknown. The AlSi12 alloy has the same Al-matrix in all conditions and, therefore, similar load bearing capability must be expected for

this phase. Rietveld refinements at the end of the experiments indicate the exact volume fraction of Si and Al that must be considered during this analysis. The volume fraction of Si within the gauge volume ranges between 17.4 vol.% and 18.3 vol.%. This results in a maximum $\Delta\sigma \sim 30$ MPa for the Al matrix in all conditions. This value is similar to the yield stress reported by Asghar et al [65] for an identical matrix alloy at 300°C.

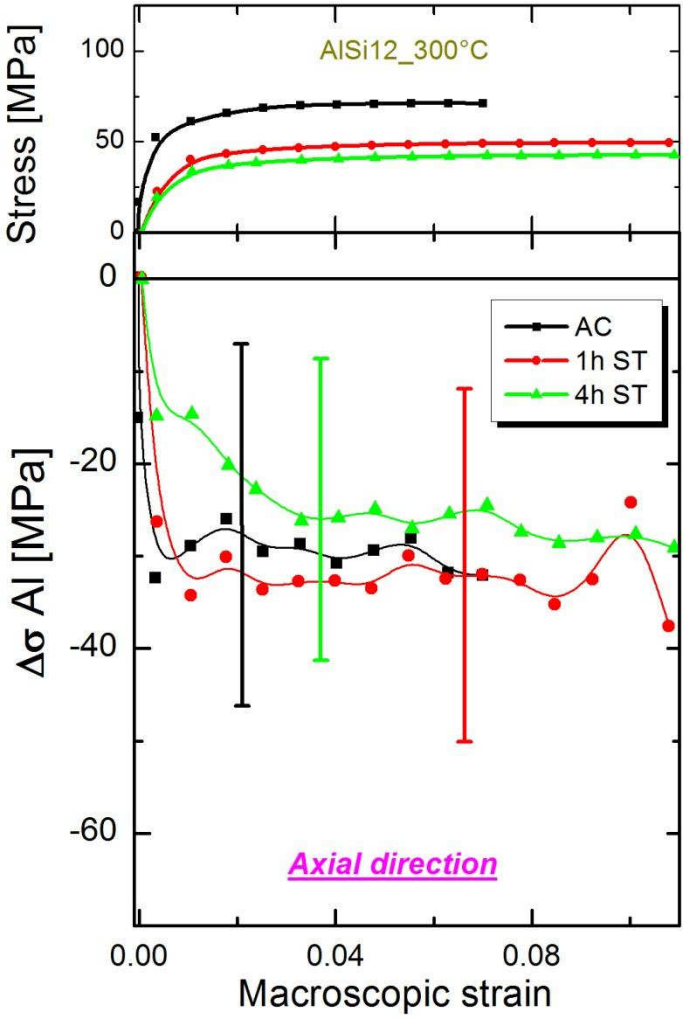

Fig. 5.2. Stress evolution for Al matrix in AC, 1h and 4h ST for ASi12 at 300°C. The evolution is shown up to the maximum external stress for each ST condition.

An earlier plastification of the Al-matrix is observed for the AC condition in the AlSi12 alloy, followed by 1h and 4h ST conditions although the large error bars hinder a deep analysis. The study of the peak broadening (FWHM) is a valid tool to investigate this issue. Different contributions are involved in this FWHM. For the Si, constant dislocation densities can be considered for all ST conditions since this phase does not deform plastically. Therefore, the FWHM is an indication of the elastic microstrains distribution generated in this phase. The larger aspect ratio of the interconnected Si lamellae for the 0h ST condition results in larger local strain differences between different regions of the same lamella leading to higher stresses in Al and finally to a faster onset of the plastification. This is reflected by the

higher FWHM for the 0h ST condition in Fig. 5.3. On the contrary, the 4h ST exhibits the lowest FWHM since the shape of the Si particles is more rounded resulting in a more homogeneous distribution of elastic microstrains, delaying the onset of the plastification. Similar FWHM evolution is observed for Si in the 1062 alloy, where the more rounded Si shows smaller FWHM values for the 4h ST.

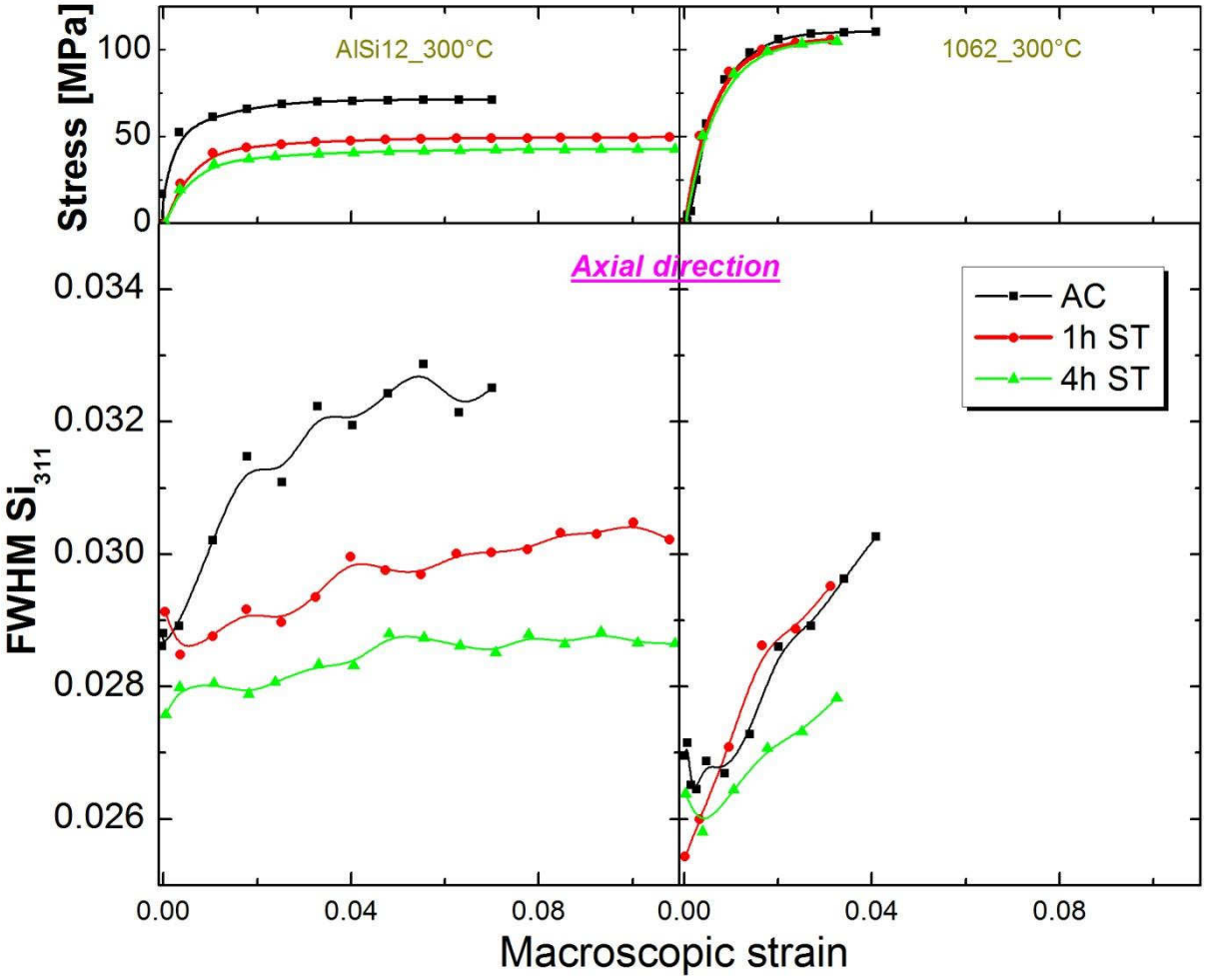

Fig. 5.3. FWHM evolution for the Si-phase in AC, 1h and 4h ST for the AlSi12 (left) and 1062 (right) alloys at 300°C. The evolution is shown up to the maximum external stress for each ST condition.

5.2 Load transfer in particle reinforced Ti alloys

Similarly to the unreinforced Al alloys, the stresses in the α-, β- and TiC-phases were evaluated using Eq. 3.2 and the elastic constants defined in section 3.4.5. In order to simplify the load transfer study, reflections corresponding to α-103, β-211 and TiC-311 (with NaCl cubic structure [83]) were selected since they are weakly affected by intergranular strains in the hcp, bcc and fcc crystal structures, respectively [97]. Finding the crystallographic elastic constants for the β-phase is not a straightforward task due to the difficulty to determine them experimentally. Therefore, and in order to simplify the problem, a linear interpolation was

carried out using the macroscopic E and ν at RT and 1000°C [101-102]. It is assumed that the crystallographic elastic constants E and ν for the β-211 reflection do not differ considerably with respect to the macroscopic values.

Fig. 5.4 shows the stresses calculated for the PM alloy and the PRMs at 750°C (left) and 850°C (right). Only the region until the maximum external stress is considered for the stress analysis. The stress-strain curves show similar slopes for the unreinforced alloy and the PRMs, i.e., the presence of the TiC particles does not improve the strength of the composites with respect to the matrix. Comparing the micrographs of the PM alloy (Fig. 3.6) and the PRMs (Fig. 3.8), smaller α-lamellae are observed for the PRMs, which are responsible for their higher ductility. Using the Hall-Petch relation (2.3.2), the yield stress increment of the PRM can be roughly calculated considering an equivalent diameter $D \sim 20\mu m$, giving $\Delta\sigma_{YM} \sim 22$ MPa, i.e., in the same order of magnitude as observed for engineering stress-strain curves.

In order to avoid uncertainties in the determination of d_0, the stresses for the different phases are analyzed from an incremental point of view, i.e., they are shifted to zero at the beginning of the tensile test. At 750°C, the α-stresses in the axial direction vary with higher initial slope in the PM alloy, while the PRMs evolve with approximately similar slopes. The β-phase shows identical values for the unreinforced and reinforced alloys and the TiC-phase is able to bear load with a slightly higher initial slope for the 12 vol.% PRM.

The equilibrium phase diagram of the Ti662 alloy [3] shows that the volume fraction of β-phase is 35 vol.% and 50 vol.% at 750°C and 850°C, respectively. Additionally, it is possible to perform Rietveld refinements at the end of the experiments, revealing the following phase volume fractions (R_w = 19.9%, 13.6% and 14.2 % for the Ti662PM, Ti662/TiC/12p and Ti662/TiC/20p, respectively) within the investigated gauge volumes at 750°C:

1) Ti662 PM: α ~ 59.9 vol.% and β ~ 40.1 vol.%.
2) Ti662/TiC/12p: α ~ 52.2 vol.%, β ~ 28.6 vol.% and TiC ~ 19 vol.% for Ti662/TiC/12p (35 vol.% of β in the matrix).
3) Ti662/TiC/20p: α ~ 30.2 vol.%, β ~ 29.1 vol.% and TiC ~ 40.5 vol.% for Ti662/TiC/20p (49 vol.% of β in the matrix).

These values show that the volume fraction of α- and β-phases differ significantly for Ti662 PM and Ti662/TiC/20p from those expected from the equilibrium diagram.

Furthermore, the volume fraction of TiC particles is up to two times larger than the nominal concentration. However, stress equilibrium is not achieved applying the relationship:

$$\sigma_A = f'_{TiC}\sigma_{TiC} + f'_{\beta}\sigma_{\beta} + f'_{\alpha}\sigma_{\alpha} \qquad (5.1)$$

where f'_i indicates the local volume fraction of each phase within the gauge volume.

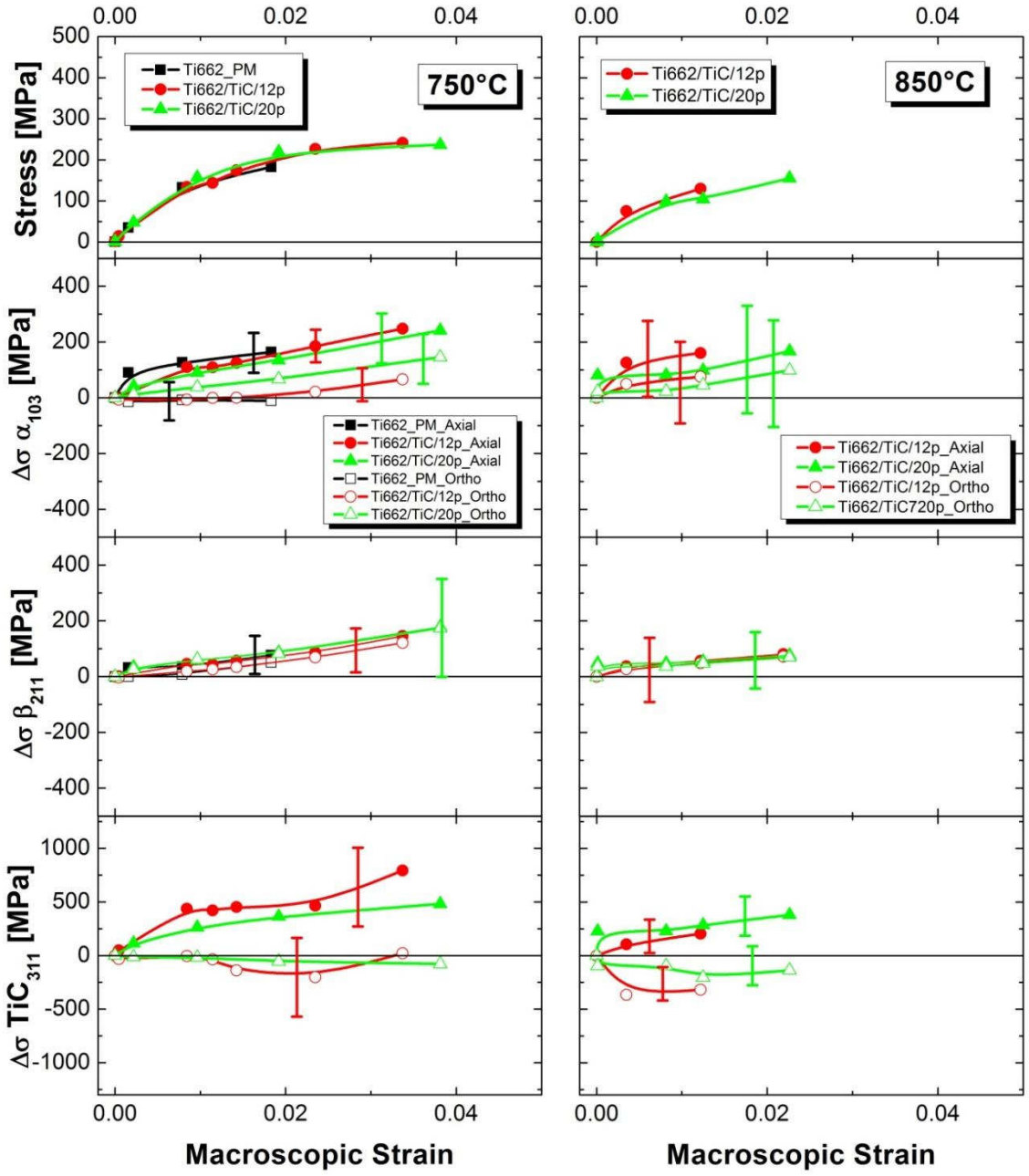

Fig. 5.4. Stress vs macroscopic strain evolution up to the maximum external load of the PM and PRMs alloys during tensile loading for the α-103, β-211 and Ti-311 reflections at 750°C (left) and 850°C (right).

A more detailed study of the microstructure and the experimental conditions must be done to understand this issue. Fig. 5.5 shows the Ti662/TiC/20p after deep etching of the matrix where a particle cluster with some interconnectivity can be observed. Furthermore, these particle clusters are heterogeneously distributed within the matrix (Fig. 3.8).

Considering the "dogbone" sample used during the hot tensile experiments (Fig. 5.6 a)) and analysing a cross section parallel to the load direction for the PRMs (Fig. 5.6 b)), the gauge volume represents only a small region that could even include only TiC particle clusters. This variation of local volume fraction in regions of the same size as the gauge volume results in the formation of a heterogeneous macrostress profile σ_I (see Fig. 5.6 c)), whose local mean magnitude is added to the microstresses at the position of the gauge volume. Therefore, the following expression must be applied to correctly describe the stress condition within the applied gauge volume:

$$\sigma_A = \sigma_I + f'_{TiC}\sigma_{TiC} + f'_{\beta}\sigma_{\beta} + f'_{\alpha}\sigma_{\alpha} \qquad (5.2)$$

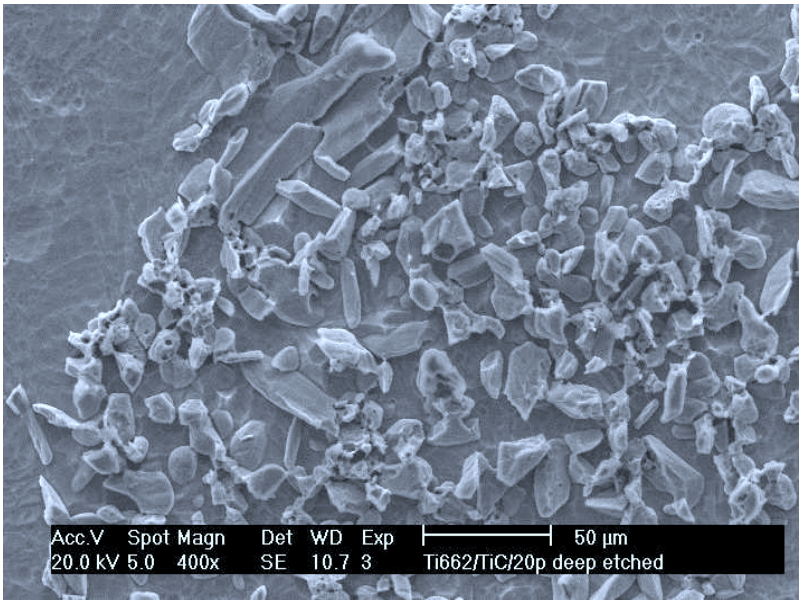

Fig. 5.5. Deep etching of the Ti662/TiC/20p at RT showing interconnected TiC particles.

Therefore, the small gauge volume plays an important role in the stress determination for such heterogeneous microstructures. Similar gauge volume effect was observed by Bruno el al. [113] during the residual stress determination in MMCs. A complete coverage of the cross-section of the sample by the gauge volume would have vanished the effect of the local macro stresses.

Another way to analyse the evolution of the load is looking at the evolution of the deviatoric stresses. Fig. 5.7 shows the calculated deviatoric stresses at 750°C (left) and 850°C (right) with the expression proposed by Garcés et al. [56], where no stress-free reference d_0 is needed:

$$\sigma_1 - \sigma_3 = -\frac{E}{(1+\nu)}(\theta_1 - \theta_3)\cot\theta \qquad (5.3)$$

$$\sigma_2 - \sigma_3 = -\frac{E}{(1+\nu)}(\theta_2 - \theta_3)\cot\theta \qquad (5.4)$$

$$\sigma_1 - \sigma_2 = -\frac{E}{(1+\nu)}[(\theta_1 - \theta_3) - (\theta_2 - \theta_3)]\cot\theta \qquad (5.5)$$

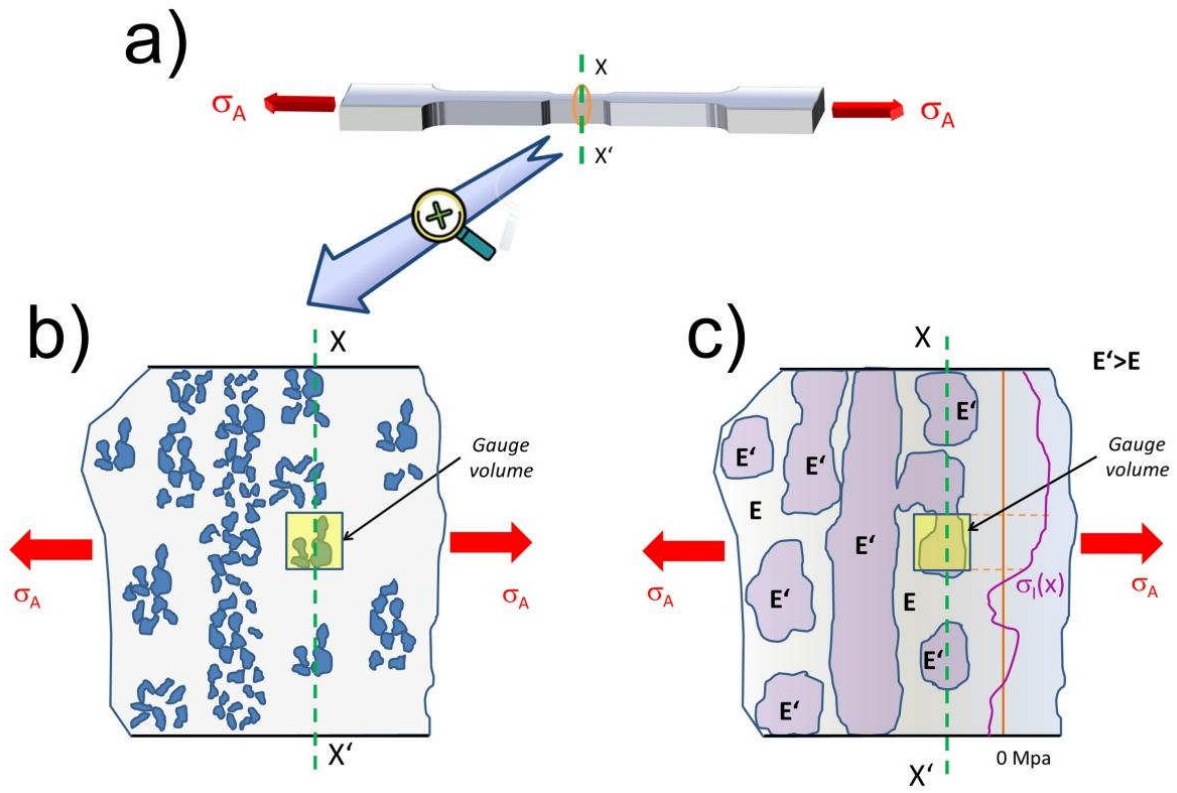

Fig. 5.6. a) "Dogbone" PRM sample used during the hot temperature tensile tests. A cross section parallel to the load direction where the particle cluster and the scaled gauge volume are observed is shown in b). Regions with different local physical and mechanical properties as a result of particle clusters are shown in c).

The stresses in the axial direction are indicated by σ_1 while those corresponding to the orthogonal direction are σ_2 and σ_3. The θ angle corresponds to the scattering angle at the beginning of the tensile test, either in axial or orthogonal direction since the influence is negligible in the final stress differences. Assuming a cylindrical symmetry in our case, i.e., $\sigma_2 = \sigma_3$, the first and the third expressions are equal and the second one is zero.

At 750°C, the α-phase exhibits a maximum (σ_1-σ_3) of ~ 230 MPa, ~ 180 MPa and ~ 140 MPa for the PM alloy, Ti662/TiC/12p and Ti662/TiC/20p, respectively. The TiC-phase shows a maximum $\Delta\sigma$ of ~ 790 MPa and ~ 660 MPa for the Ti662/TiC/12p and Ti662/TiC/20p, respectively. The β-phase shows practically identical values close to zero in the matrix and the composites. Similarly to Fig. 5.4, the hardening slopes for the α-phase and the TiC particles show that the particles are able to bear part of the load. This load transfer to the TiC particles is not reflected macroscopically as an effective reinforcement of the matrix owing to their inhomogeneous distribution with local volume fractions much higher than the nominal values and particle-free regions. Therefore, there may be a potential to improve the strength of these composites if a more homogeneous distribution of the TiC particles is achieved.

The lack of results for the PM alloy at 850°C does not allow to study completely the load partition. Nevertheless, a behaviour similar to 750°C is found (Fig. 5.7), i.e., different slopes for the α-phase stress-strain curves.

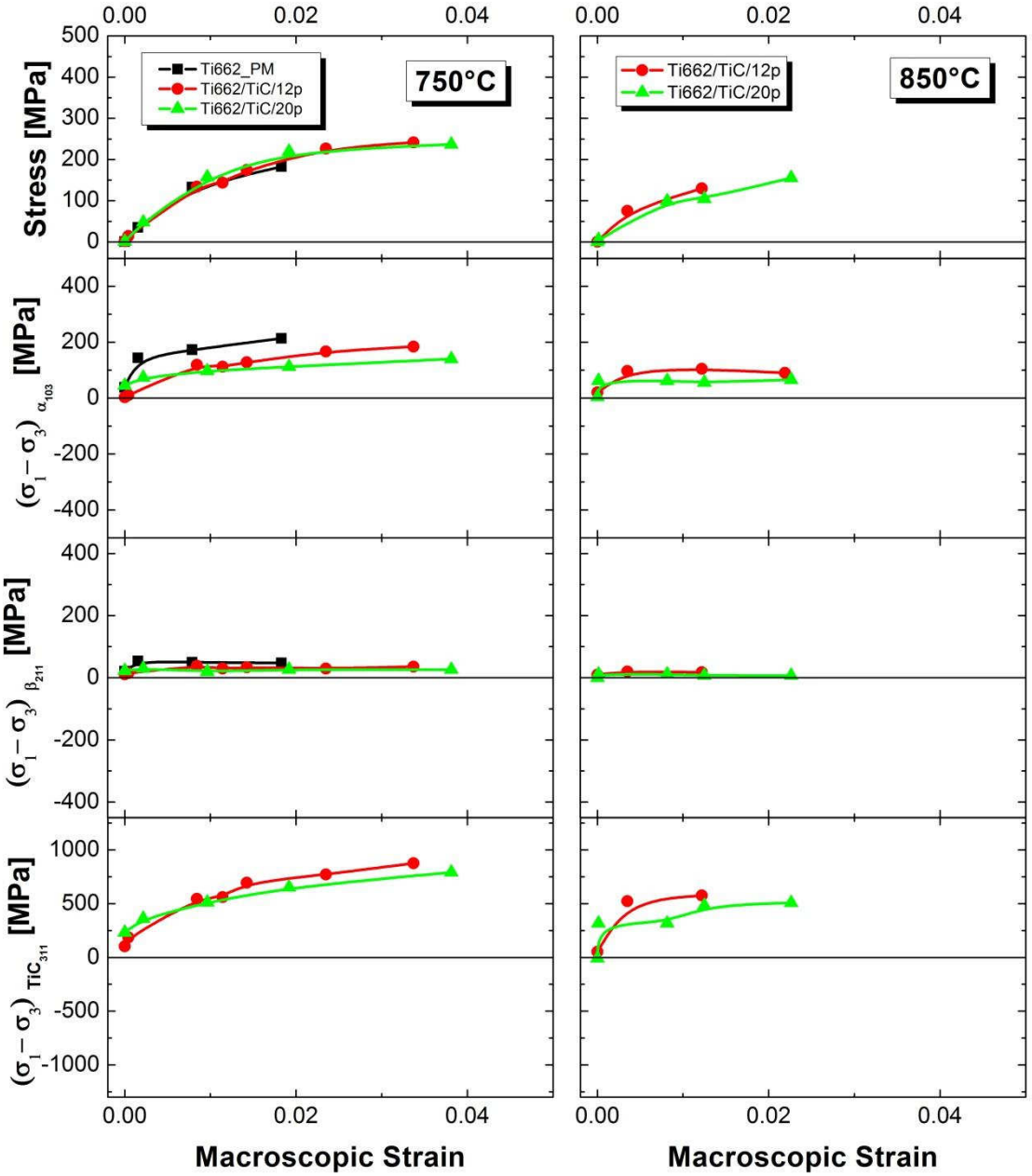

Fig. 5.7. Deviatoric stresses vs macroscopic strain during tensile loading for the α-103, β-211 and Ti-311 reflections at 750°C (left) and 850°C (right). Error bars are included in the symbols.

5.3 Particle reinforced aluminium alloys

The net initial stress condition at RT at the beginning of the thermal cycles is the same for all PRMs, namely compressive in the SiC particles and tensile in the Al-matrix. These stresses arise during the cooling from 300 ºC after the 2 h overaging heat treatment at this temperature. Since the highest temperature reached during the thermal cycles is 300 ºC, the

same stress condition is achieved at RT after each thermal cycle, resulting in the observed closing of the temperature-stress loop. The thermal stresses build up due to the thermal mismatch between the SiC particles and the 2124 and 6061 matrices (see e.g. [20]). During heating, the stresses in the SiC particles and the Al-matrix invert at a certain temperature, becoming tensile and compressive, respectively. This initial tensile stress condition and its inversion from tensile to compressive stresses in the metallic matrix during heating are well known for MMC [20].

The stress evolution during heating is expected to be linear up to the yield stress of the matrix in absence of relaxation mechanisms (see e.g. [20]). However, the linear tendency of the stress evolution during heating of the BM and WB PRMs disappears at a stress smaller than the yield stress of the matrix at 300 ºC ($\sigma_{0.2\text{-}300ºC}$ ~ 90 MPa for the 2124 [99] and ($\sigma_{0.2\text{-}300ºC}$ ~ 57 MPa for the 6061 [87]). Furthermore, the stress difference $\Delta\sigma$ expected in the matrix-particle interface by heating from RT to 300 ºC can be roughly estimated by the simple relationship [114]

$$\Delta\sigma = \Delta\alpha \cdot \Delta T \cdot \frac{4G_{Al}(1-f_{SiC})}{3-\frac{4}{3}G_{Al}(\frac{1}{K_{Al}}-\frac{1}{K_{SiC}})(1-f_{SiC})} \qquad (5.6)$$

where $\Delta\alpha$ is the CTE difference between the matrix and the SiC particles, ΔT ~ 270 °C, G_{Al} ~ 23 GPa is the shear modulus of the matrix at 300 °C [99], K_{Al} ~ 50 is the bulk modulus of the matrix at 300 °C [99] and K_{SiC} = 375 GPa is the bulk modulus of SiC at 300 °C [115]. This gives $\Delta\sigma$ = - 145 MPa, which is larger than the maximum stress change observed experimentally for the composites for the same temperature change, i.e. $\Delta\sigma_{expBM\ 2124}$ ~ - 120 MPa, $\Delta\sigma_{expWB\ 2124}$ ~ - 95 MPa and $\Delta\sigma_{expWB\ 6061}$ = - 80 MPa. Such a discrepancy between the measured misfit stress and that expected from the temperature variation was also observed in [116] for a PM 2124 alloy reinforced with 17 vol.% of SiC particles quenched from 505°C and naturally aged at room temperature and this was attributed to relaxation of the internal stresses in the MMC. In the present work, the loss of linearity during heating and $\Delta\sigma_{exp} < \Delta\sigma$, indicate that some kind of relaxation process acts during thermal cycling. This relaxation mechanism is also more effective in the WB PRM since it shows a smaller slope of the heating curve. One possible relaxation mechanism is internal damage, e.g. particle fracture, decohesion of the interface matrix-particle, etc. However, damage is not likely to take place in the early stages of thermal cycling without applied stresses in this type of composites [117]. On the other hand, thermally activated relaxation mechanisms, i.e. creep, may also take place. Thus, the relaxation process of the thermal stresses generated by temperature changes will be divided in a low and a high temperature

region depending if creep is activated or not. The transition temperature separating these two regions can be roughly estimated as 0.4 × Tm, where Tm is the absolute melting point of the phase/s for which creep is activated, in our case the 2124 and 6061 Al matrices. The liquidus temperature of these alloys is 638 ºC, which means that the transition temperature is ~ 90 ºC.

The tensile creep behaviour at 300 ºC of BM 2124/SiC/25p/<20µm and WB 2124/SiC/25p/<20µm in the direction of extrusion has been recently reported in [39] and for the WB 6061/SiC/25p in [87]. Although the creep results are for tensile stress conditions and the stresses obtained for the matrix during thermal cycling in the present study are compressive, a comparison between both studies is valid for the primary and stationary creep states where damage does not play a significant role. The BM PRM showed a superior creep resistance than both the 2124 matrix and the WB PRM owing to the higher volume fraction of sub-µm oxide and SiC particles introduced during the BM process. The stationary creep rate at 300 ºC in the WB PRM is ~ 4 orders of magnitude faster than in the BM PRM for the same load condition in the range of stresses investigated (Fig. 5.8 – extracted from [39, 87]). This indicates that stress relaxation occurs faster in the WB PRMs and this is the reason why the thermal stresses generated during heating in the axial direction show a smaller slope than for the BM PRM (see Fig. 4.26).

The thermal stresses in the matrix in the axial direction during heating reach ~ - 10 MPa, ~ - 15 MPa and ~ - 50 MPa at 230 ºC for the WB 2124, WB 6061 and BM 2124 composites, respectively. These stresses remain practically constant up to the maximum measured temperature of 300 ºC. Furthermore, the stresses in the isothermal step at 230 ºC also remain constant indicating that the thermal stresses generated within this period of time (30-35 min) cannot relax completely. The stationary creep rate at 300 ºC at these stresses (10, 15 and 50 MPa) is the same for both composites, namely ~ 10^{-10} s^{-1} (Fig. 5.8 [39, 87]). This is, however, an underestimation of the stress relaxation rate since it corresponds to a stationary creep condition, while diffraction was carried out immediately after reaching the test temperature and for only 200 s. This is a situation much closer to a primary creep process that must result in faster stress relaxation rates that gradually decrease with time. Fig. 5.8 also shows the dependence of the creep rate measured at the beginning of the creep tests [87] (during the first 1-10 h of creep, depending on the stress) and of the stationary creep rates at 300 ºC on the applied stress for the BM and WB composites [39]. The relaxation rate for the thermal stresses measured at 300 °C, namely ~ - 10 MPa, ~ - 15 MPa and ~ - 50 MPa for the WB 2124, WB 6061 and BM 2124 PRM, respectively, is between 5 × 10^{-9} - 3 × 10^{-8} s^{-1} as

indicated by the shadowed region in Fig. 5.8. Higher thermal stresses relax completely at faster rates during the 200 s of diffraction scanning.

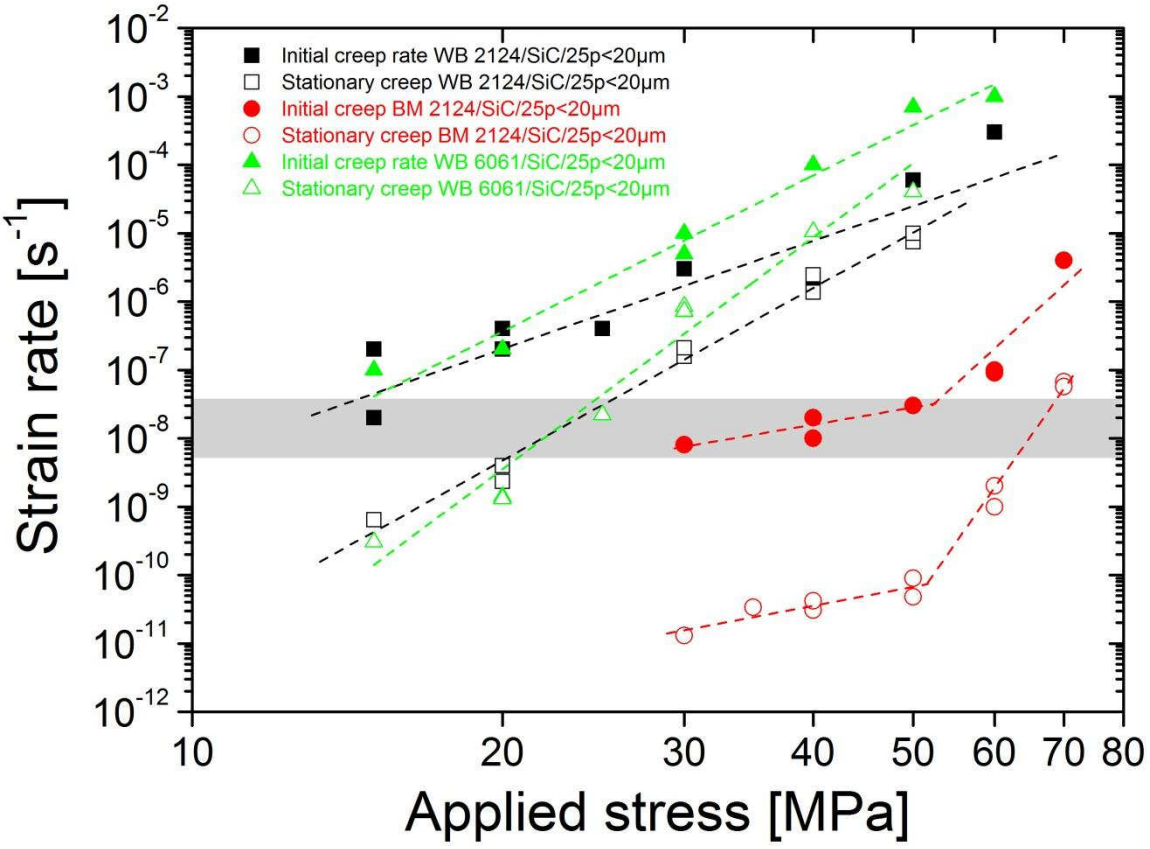

Fig. 5.8. Primary and stationary creep rates at 300°C for the BM and WB composites [39, 87]. The grey band marks the strain rate of the investigated thermally induced relaxation.

It has to be pointed out that the thermal stresses generated during thermal cycling are practically the same for the axial and radial directions in the WB composites. On the other hand, there is a marked difference between the axial and radial directions of the BM PRM, with the relaxation behaviour of the radial direction being more similar to the WB PRMs. Rösler and Arzt. [44] observed similar differences in the microstructure of extruded oxide dispersion strengthened aluminium that resulted in a higher creep resistance in the direction of extrusion which was attributed to a strong [111] fibre texture of the matrix developed during the extrusion process. Anisotropic relaxation of the thermal misfit strain was also considered in [116] to explain the different thermal stresses measured in different directions in a PM 2124/SiC/17p.

During cooling the thermal stresses produce the initial stress state, i.e. the SiC particles are in net compressive state, while the 2124 and 6061 matrices are under net tensile stress. From 300 ºC down to 100 ºC the thermal stresses vary linearly for all PRM, while a decrease of the slope is observed between 100 ºC and RT that results in the closing of the thermal stress loop (see Fig. 4.26). This means that the initial and final stress state after thermal

cycling for all composites is the same, namely ~ 80 ± 30 MPa and 60 ± 30 MPa in the axial and radial directions of the matrix. The change in slope at lower temperatures is related to matrix yielding resulting in a period of matrix flow (see e.g. [118, 119]). However, the yield stress of the 2124 and 6061 matrices in T7 condition is higher than the average thermal stress values obtained at RT indicating that local microplasticity takes place.

5.4 Microstructural evolution and deformation mechanisms in unreinforced and particle reinforced Ti662 alloys

According to the AS-plots (Fig. 4.15, Fig. 4.16 and from Fig. 4.36 to Fig. 4.39), the changes observed in the α- and β-phase of the unreinforced PM alloy and PRMs start when the stress is maximum, i.e., a previous accumulation of plastic deformation is necessary for their activation [120]. The α-phase in the PM alloy, at 650°C and 750°C, undergoes mainly grain rotation since the bands corresponding to the initial diffraction spots only modify their azimuthal angle and keep their width relatively constant. The vanishing of some bands occurs when the grains do not match the Ewald´s sphere in the reciprocal space owing to their rotation. This deformation mechanism was already observed by Liss et al. [78] during hot compression of titan aluminide alloys with globular α-grains. During the in situ tensile tests, rotation of α-002 is observed in all directions and no preferred reorientation is identifiable at the end of the deformation. The grain rotation observed by diffraction in the α-phase is a combination of the geometrical reorientation of the lamellae [121] and crystallographic rotation within the lamellae.

The rotation of the α-lamellae can be linked to the macroscopic strain. If we consider a lamella with an orientation γ with respect to the external load (Fig. 5.9 a)) rotating φ degrees clockwise, the axial strain provoked by this deformation can be roughly estimated as follows:

$$\varepsilon = \frac{L\times\cos(\gamma-\varphi)-L\times\cos(\gamma)}{L\times\cos(\gamma)} = \frac{\cos(\gamma-\varphi)-\cos(\gamma)}{\cos(\gamma)} \qquad (5.7)$$

where L is the length of the lamella, γ the initial angle of the lamella with respect to the external load and φ the rotation angle. At 650°C, considering an "activity strain" (strain increment that corresponds to the interval during which the rotation is observed in the AS-plots) of ε = 0.06 and varying the different lamellae angle γ, the function shown in Fig. 5.10 is obtained:

$$\varphi = \gamma - \cos^{-1}[(0.06+1)\times\cos\gamma] \qquad (5.8)$$

The maximum rotation angle φ observed in Fig. 4.15 for the α-002 reflection is ~ 10° at Ψ ~ 135°. Taking into account that the α-{002} planes are oriented parallel to the length of

the lamellae [122] in undeformed condition then the correspondence shown in Fig. 5.9 b) can be done between Ψ, γ and lamella orientation. Thus, Ψ = 135° corresponds to γ = 45° for which φ = 3.5. However, as mentioned before a maximum rotation of ~ 10° is observed for α-{002} in the AS-plots (Fig. 4.15) indicating that also crystallographic rotation within the lamellae must take place during deformation. Similar conclusion can be drawn for the experiment at 750°C, where the maximum rotation angle observed is 5° with an "activity strain" of ~ 0.05. EBSD is an appropriate tool to analyze crystallographic rotation. An analysis performed for the Ti662 PM sample deformed at 650°C indicates that different geometrical orientations are generated within the lamellae reflected by the different colour within them in Fig. 5.11.

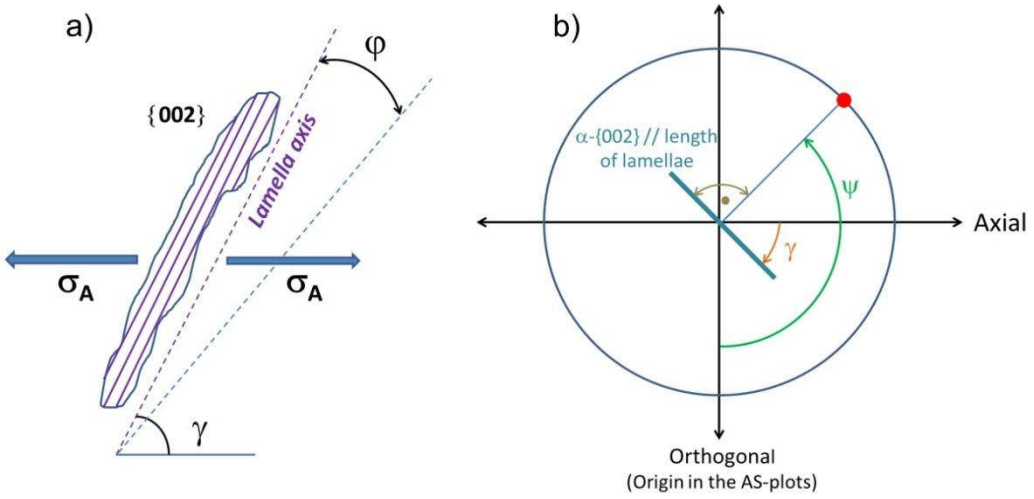

Fig. 5.9. a) Schematic representation of α-lamella orientation. b) Orientation of α-{002} with respect to γ and Ψ during the in situ tensile tests.

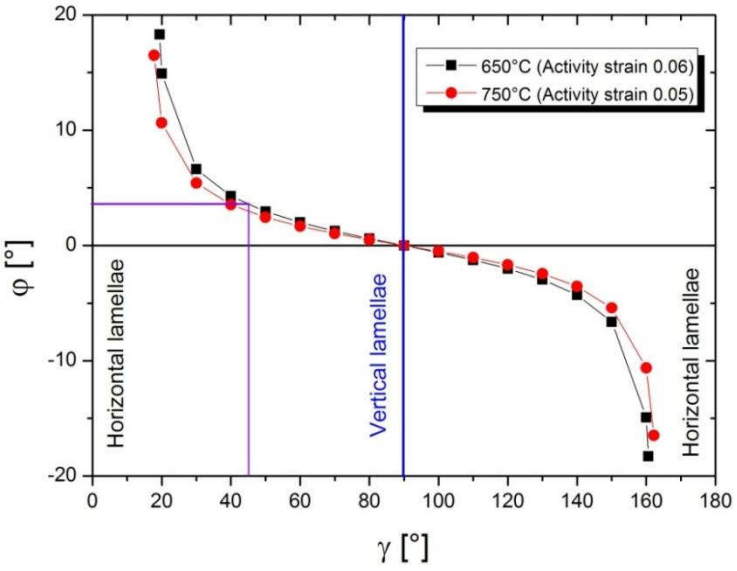

Fig. 5.10. Maximum lamella rotation considering the activity strains ε = 0.06 and ε= 0.05 for the experiments at 650°C and 750°C, respectively.

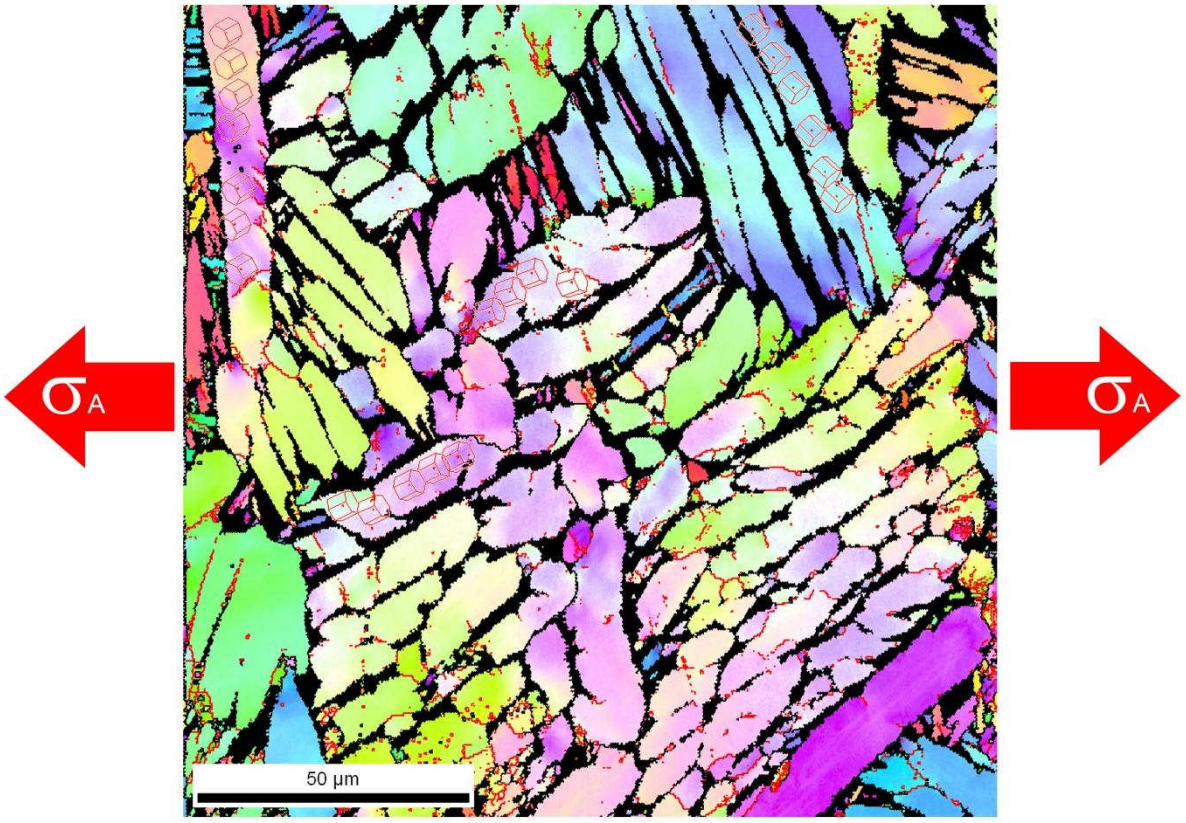

Fig. 5.11. α-grain orientations of the PM alloy tested at 650°C. Different crystallographic orientations within the lamellae can be distinguished by the depicted hexagonal lattices and different colours within them.

The PRMs exhibit the same deformation mechanisms as the unreinforced matrix but the smaller lamella size leads to a larger number of initial diffraction spots that result in a more continuous scattering intensity distribution in the AS-plots hindering a clear observation of these deformation mechanisms.

No evidence of dynamic recrystallization was clearly revealed. It is important to point out that the tensile tests were carried out sequentially. Therefore, the accumulated energy at high temperature may partially dissipate during the interruption between deformation steps unloading steps. Warwick et al. [123] reported recently the presence of dynamic recrystallization in a Ti64 alloy during high rolling strains applied in a continuous process.

The observed texture for the IM alloy at different tensile test temperatures is a consequence of the processing route where the billet is subjected to a hot compression together with a cogging process just below the transus temperature provoking a dominant orientation for the α-phase with the 002-plane orientated orthogonally to the radial/transversal direction of the billet (radial direction of the samples), i.e., parallel to the cogging direction (orthogonal direction of the samples) [83]. This is reflected by the higher intensity regions at 90° and 270°C in Fig. 4.17 and Fig. 4.18 and in the reconstructed pole figures of Fig. 4.20 and Fig. 4.21. The globular structure of the α-grains try to align with the α-002 crystallographic

plane orthogonal to the load direction [78], i.e., undergoes a crystallographic rotation. Since the α-002 plane nucleates from β-110, some relation can be expected between them. Indeed, the β-110 plane shows equally to the α-002 certain texture orthogonally to the radial/transversal direction of the billet (axial direction of the sample) although the dominant orientation seems to be orthogonally to the cogging direction (orthogonal direction of the sample).

6 Conclusions

The next conclusions can be drawn from the present work:

6.1 Load partition in Al-based alloys

6.1.1 High temperature compression of cast Al-Si alloys

- The eutectic Si in the AlSi10Cu6Ni2 alloy is capable of bearing a higher load than in the AlSi12 alloy in corresponding heat treatment conditions owing to the presence of highly contiguous 3D networks of Cu, Ni and Fe aluminides. These aluminides partially avoid the spheroidization of eutectic Si during the solution treatments conserving thus its load bearing capability.
- The high interconnectivity of eutectic Si in the AC condition of the AlSi12 and 1062 alloys results in a higher load carrying capability than after 1h and 4h solution treatment at 500°C for identical externally applied strains. The longer the solution treatment the more rounded the Si lamellae (isolated particles in the AlSi12 alloy after 4h solution treatment at 500°C).
- The Al_2Cu-phase plays an important role on the onset of the damage in the AlSi10Cu6Ni2 since it is one of the first phases that fail during the high temperature compression tests.

6.1.2 Thermal cycling of powder metallurgy particle reinforced Al-alloys

- The different microstructures of the unreinforced matrices and both PRMs do not allow to obtain a suitable stress-free reference sample using matrix powders. The analysis of the evolution of the thermal stresses during thermal cycling was evaluated using the stress in the matrix obtained by stress balance with the SiC phase, which has a pure elastic behaviour throughout the investigated temperature range. A recalculation of d_0 from the stress-balance condition shows that the bulk matrix samples show acceptable values to be used as the stress-free reference sample for temperatures up to 230°C.
- The thermal stresses generated during the early stages of thermal cycling in both the wet blending and ball milling PRMs relax by creep at temperatures above 90°C.
- The higher axial creep resistance of the ball milling PRM, which is a consequence of the presence of a larger volume fraction of sub-μm oxide and SiC particles, slows down the relaxation process at high temperature in comparison with the wet blending

PRM. This results in the presence of an average axial compressive thermal stress of ~ - 50 MPa and ~ -10 MPa at temperatures between 230 and 300°C in the matrices of the ball milling and WB PRM, respectively. These stresses relax at rates $\leq 5 \times 10^{-9}$ -3×10^{-8} s^{-1}.

6.2 Load partition in Ti-based alloys

- The higher strength exhibited by the PRMs is related to the smaller size of the α-lamellae in comparison to the Ti662 powder metallurgy matrix. The smaller lamellae in the PRMs results in an increase of ductility of the matrix. This makes that the matrix in the PRM exhibit a longer period of strain hardening than the unreinforced alloy. Furthermore, the presence of the TiC particles does not play an important macroscopic role because of their inhomogeneous spatial distribution that reduces their efficiency. Local strain evolution shows that TiC particles are able to bear part of the applied load.
- The β-phase plastifies practically at the beginning of the tensile tests.
- The load carried by the α-phase increases with deformation until the maximum strength of the alloy is reached. The higher the vol.% of TiC particles, the slower the increment of load with the applied strain in the α-phase.
- Part of the external load is carried by the TiC particles in the PRMs and, similarly to the α-phase, the higher the vol.% of TiC particles, the slower the increment of load in TiC-phase.
- The PRMs show potential to improve the mechanical properties of the powder metallurgy alloy but a more homogeneous TiC particle distribution must be achieved.

6.3 Microstructural evolution and deformation mechanisms in Ti-based alloys

- The α-phase deforms by grain rotation in the Ti662 powder metallurgy alloy. This rotation is the consequence of geometrical reorientation of the lamellae and crystallographic rotation within the lamellae. No preferred final orientation of α-002 is observed during the hot tensile tests for the Ti662 alloy produced by powder metallurgy.
- The β-phase in the Ti662 powder metallurgy alloy deforms by increase of misorientation within grains and subgrain formation, especially at T > 750°C.
- The ingot metallurgy Ti662 alloy, and because of its globular structure, only undergoes crystallographic rotation of the α-lattice with final texture related to the cogging direction.

6.4 Comparison of methods

As a result of the present work, Table 6.1 shows the advantages and disadvantages of the two different diffraction techniques applied to the unreinforced and reinforced Al and Ti alloys to carry out in situ high temperature tests.

Alloy	Test	Neutron diffraction		Synchrotron diffraction	
		Advantages	*Disadvantages*	*Advantages*	*Disadvantages*
AlSi12 ***AlSi10Cu6Ni2***	High temperature compression test			- Fast acquisition times allow following in situ strains in Si	- Hindered the study of Al strain because of the large grain size and small gauge volume 1x1x5 mm^3
2124/SiC/25p ***6061/SiC/25p***	Thermal cycling	- Large gauge volumes 5x5x5 mm^3 avoid influence of macrostresses and allow analysing Al strains even for large grains	- Slow acquisition time leads to influence of stress relaxation during acquisition		
Ti662 powder metallurgy	High temperature tensile test			- Fast acquisition times - Allows determining deformation mechanisms for large-grained materials	- Influence of macrostresses - Large uncertainty in the strain evaluation for large-grained materials
Ti662 ingot metallurgy	High temperature tensile test			- Allows to study the strains because of fine-grained wrought billet microstructure - In situ texture evolution	
Ti662/TiC/12p ***Ti662/TiC/20p***	High temperature tensile test			- Strain better defined than in the matrix because of the smaller grain size	- Influence of macrostresses - The microstructure evolution is not clearly defined

Table 6.1. Asses of the neutron and synchrotron diffraction techniques over the different Al- and Ti-based alloys.

7 References

[1] Polmear I.J., *Light Alloys*, Elsevier 2006.

[2] http://aluminium.matter.org.uk

[3] Peters M., Leyens C., *Titan und Titanlegierungen*, Wiley VCH, Weinheim 2002.

[4] Ashby M., *Materials Selection in Mechanical Design*, Butterworth-Heinemann 2000.

[5] CES Selector 5.1.0, Granta Design, Cambridge 2009.

[6] Callister W.D., Rethwisch D.G., *Materials Science and Engineering: An introduction*, John Wiley & Sons 2010.

[7] Burgers W.G., *On the process of transition of the cubic-body-centered modification into the hexagonal-close packed modification of zirconium*, Physica, vol.1, pp.561-586, 1934.

[8] Lütjering G., Williams J.C., *Titanium*, Springer 2007.

[9] Davis J.R., *ASM specialty handbook: Aluminium and Aluminium alloys*, 1993.

[10] Bell J.A.E., Winegard W.C., *Interconnexion of silicon in modified aluminium-silicon eutectic*, Nature, vol.208, 5006, p.177, 1965.

[11] Lasagni F., Lasagni A., Marks E., Holzapfel C., Mücklich F., Degischer H.P., *Three-dimensional characterization of 'as-cast' and solution-treated AlSi12(Sr) alloys by high-resolution FIB tomography*, Acta Materialia, vol.55, pp.3875-3882, 2007.

[12] Requena G., Garcés G., Rodríguez M., Pirling T., Cloetens P., *3D architecture and load partition in eutectic Al-Si alloys*, Advanced Engineering Materials, vol.11, pp.1007-1014, 2009.

[13] Zhu P.Y., Liu Q.Y., Hou T.X., *Spheroidization of eutectic silicon in Al-Si alloys*, AFS transactions, vol. 93, pp.609-614, 1985.

[14] Sahoo M., Smith R.W., *Mechanical properties of unidirectionally solidified Al-Si eutectic alloys*, Metal Science J, vol. 9, pp.217-222, 1975.

[15] Hosch T., Napolitano R.E., *The effect of the flake to fiber transition in silicon morphology on the tensile properties of Al-Si eutectic alloys*, Materials Science and Engineering A, vol.528, pp.226-232, 2010.

[16] *Binary Alloy Phase Diagrams*, vol.1, Massalski T.B., ed., ASM, Metals Park, Ohio, 1986.

[17] Boyer R., Welsch G., Collings E.W., *Materials Properties Handbook: Titanium Alloys*, ASM International, Materials Park, 2007.

[18] http://mmc-assess.tuwien.ac.at

[19] Degischer H.P., *Innovative light metals: metal matrix composites and foamed aluminium*, Materials & Design, vol.18, pp.221-226, 1997.

[20] Clyne T.W., Withers P.J., An introduction to Metal Matrix Composites, Cambridge University Press, 1993.

[21] Cox H.L., *The elasticity and strength of paper and other fibrous materials*, British Journal of Applied Physics, vol.3, pp.72-79, 1952.

[22] Nardone V.C., Prewo K.M., *On the strength of discontinuous silicon carbide reinforced aluminium composites*, Scripta Metallurgica, vol.20, pp.43-48, 1986.

[23] Kainer K.U., *Metal Matrix Composites*, Wiley-VCH, Weinheim, 2006.

[24] Miller W.S., Humphreys F.J., *Strengthening mechanisms in particulate metal matrix composites,* Scripta Metallurgica et Materiala, vol.25, pp.33-38, 1991.

[25] Arsenault R.J., Shi N., *Dislocation generation due to differences between coefficients of thermal expansion*, Materials Science and Engineering, vol.81, pp.175-87, 1986.

[26] Hansen N., *The effect of grain size and strain on the tensile flow stress of aluminium at room temperature*, Acta Metallurgica, vol.25, pp.863-869, 1977.

[27] Hall E.O., *The deformation and ageing of mild steel: III. Discussion of results*, Proceedings of the Physical Society B, vol.64, pp.747-753, 1951.

[28] Petch N.J., *The cleavage strength of polycrystals*, Journal of the Iron and Steel Institute, vol.174, pp.25-28, 1953.

[29] McElroy R.J., Szkopiak Z.C., *Dislocation-substructure-strengthening and mechanical-thermal treatments of metals*, International Metallurgical Reviews, vol.17, pp.175-202, 1972.

[30] Christman T., Suresh S., *Microstructural development in an aluminum alloy-SiC whisker composite*, Acta Metallurgica, vol.36, pp.1691-1704, 1988.

[31] *Powder Metal Technologies and Applications*, ASM Handbook, vol.7, ASM International, 1998.

[32] Withers P.J., Bhadeshia, H.K.D.H., *Residual stress part 1 – Measurement techniques*, Materials Science and Technology, vol.17, pp.355-365, 2001.

[33] Hauk V., *Structural and Residual Stress Analysis by Nondestructive Methods*, Elsevier, 1997.

[34] Eshelby J.D., *The determination of the elastic field of an ellipsoidal inclusion, and related problems*, Proceedings of the Royal Society A, vol.241, pp.376-396, 1957.

[35] Rabinovitch M., Stohr J.F., Khan T., Bibring H., *Directionally solidified composites for application at high temperatures*, Handbook of Composites, vol.4, Fabrication of Composites, ed. by Kelly A., and Mileiko S.T., Elsevier, Amsterdam, pp.295-372, 1983.

[36] Chawla N., Chawla K.K., *Metal Matrix Composites*, Springer Science, 2006.

[37] Winand H.M.A., Whitehouse A.F., Withers P.J., *An investigation of the isothermal creep response of Al-based composites by neutron diffraction*, Materials Science and Engineering A, vol.284, pp.103-113, 2000.

[38] Requena G., Garcés G., Danko S., Pirling T.,Boller E., *The effect of eutectic Si on the strength of short-fibre reinforced Al*, Acta Materialia, vol.57, pp.3199-3210, 2009.

[39] Requena G., Bauer B., Degischer H.P., Lieblich M., *The effect of ball milling and wet blending on the creep behavior of a particle reinforced 2124 Al-Alloy*, International Journal of Materials Research, vol.102, pp.982-992, 2011.

[40] Requena G., Degischer H.P., *Effects of particle reinforcement on creep behavior of AlSi1MgCu*, Zeitschrift fuer Metallkunde, vol.96, pp.807-813, 2005.

[41] Mohamed F.A., *Correlation between creep behavior in Al-based solid solution alloys and power metallurgy Al alloys*, Materials Science and Engineering A, vol.245, pp.242-256, 1998.

[42] Whitehouse A.F., Winand H.M.A., Clyne T.W., *The effect of processing route and reinforcement geometry on isothermal creep behavior of particulate and short fibre MMCs*, Materials Science and Engineering A, vol.242, pp.57-69, 1998.

[43] Ma Z.Y., Tjong S.C., *The high-temperature creep behavior of 2124 aluminium alloys with and without particulate and SiC-whisker reinforcement*, Composites Science and Technology, vol.59, pp.737-747, 1999.

[44] Rösler J., Arzt E., *A new model-based creep equation for dispersion strengthened materials*, Acta Metallurgica Et Materialia, vol.38, pp.671-683, 1990.

[45] Staron P., Stress Analysis by Angle-Dispersive Neutron Diffraction, in *Neutrons and Synchrotron Radiation in Engineering Materials Science*, ed. by Reimers W., Pyzalla A.R., Schreyer A., Clemens H., Wiley-VCH, Weinheim, pp.137-153, 2008.

[46] Santisteban J.R., Stress Analysis by Energy-Dispersive Neutron Diffraction, in *Neutrons and Synchrotron Radiation in Engineering Materials Science*, ed. by Reimers W., Pyzalla A.R., Schreyer A., Clemens H., Wiley-VCH, Weinheim, pp.155-176, 2008.

[47] Valéry-Martins R., Residual Stress Analysis by Monochoromatic High-Energy X-rays, in *Neutrons and Synchrotron Radiation in Engineering Materials Science*, ed. by Reimers W., Pyzalla A.R., Schreyer A., Clemens H., Wiley-VCH, Weinheim, pp.177-194, 2008.

[48] Genzel C., Pyzalla A.R., Residuals Stress Analysis by White High Energy X-Rays, in *Neutrons and Synchrotron Radiation in Engineering Materials Science*, ed. by Reimers W., Pyzalla A.R., Schreyer A., Clemens H., Wiley-VCH, Weinheim, pp.195-220, 2008.

[49] Reimers W., Broda M., Brusch G., Dantz D., Liss K.-D., Pyzalla A., Schmackers T., Tschentscher T., *Evaluation of residual stress in the bulk of materials by high energy synchrotron diffraction*, Journal of Nondestructive Evaluation, vol.17, pp.129-140, 1998.

[50] Reimers W., Pyzalla A., Broda M., Brusch G., Dantz D., Schmackers T., Liss K.-D., Tschentscher T., *The use of high-energy synchrotron diffraction for residual stress analyses, Journal of Materials Science Letters*, vol.18., pp.581-583, 1999.

[51] Withers P.J., Use of synchrotron X-ray radiation for stress measurement, in *Analysis of residual Stress by Diffraction using Neutron and Synchrotron Diffraction*, ed. by Fitzpatrick M.E., Lodini A., Taylor & Francis, pp.170-189, 2003.

[52] Daymond, M., Withers, P.J., *A synchrotron radiation study of transient internal strain changes during the early stages of thermal cycling in an Al/SiC$_w$ MMC*, Scripta Materialia, vol.35, pp. 1229-1234, 1996.

[53] Steuwer A., Edwards L., Pratihar S., Ganguly S., Peel M., Fitzpatrick M.E., Marrow T.J., Withers P.J., Sinclair I., Singh K.D., Gao N., Buslaps T., Buffiere J.-Y., *In situ analysis of cracks in structural materials using synchrotron X-ray tomography and diffraction*, Nuclear Instruments and Methods in Physics Research B, vol.246, pp.217-225, 2006.

[54] Withers P.J., *Neutron strain measurement of internal strain in metal and ceramic matrix composites*, Key Engineering Materials, vol.108, pp.291-314, 1995.

[55] Requena G., Garcés G., Asghar Z., Marks E., Staron P., Cloetens P., *The effect of the connectivity of rigid phases on strength of Al-Si alloys*, Advanced Engineering Materials, vol.13, pp.674-684, 2011.

[56] Garcés G., Bruno G., Wanner A., *Residual stresses in deformed random-planar aluminium/Saffil® short-fibre composites*, Materials Science and Engineering A, vol.417, pp.73-81, 2006.

[57] Young M.L., DeFouw J., Almer J.D., Dunand D.C., *Load partitioning during compressive loading of a Mg/MgB$_2$ composite*, Acta Materialia, vol.55, pp.3467-3478, 2007.

[58] Requena G., Degischer H.P., *Creep behavior of unreinforced and short fibre reinforced AlSi12CuMgNi piston alloy*, Materials Science and Engineering A, vol.420, pp.265-275, 2006.

[59] Requena G., Garcés G., Danko S., Pirling T., Boller E., *The effect of eutectic Si on the strength of short-fibre-reinforced Al*, Acta Materialia, vol.57, pp.3199-3210, 2009.

[60] Roy S., Gibmeier J., Wanner A., *In situ study of internal load transfer in a novel metal/ceramic composite exhibiting lamellar microstructure using energy dispersive synchrotron X-ray diffraction*, Advanced Engineering Materials, vol.11, pp.471-477, 2009.

[61] Roy S., Gibmeier J., Kostov V., Weidenmann K.A., Nagel A., Wanner A., *Internal load transfer in a metal matrix composite with a three-dimensional interpenetrating structure*, Acta Materialia, vol.59, pp.1424-1435, 2011.

[62] Roy S., Gibmeier J., Kostov V., Weidenmann K.A., Nagel A., Wanner A., *Internal load transfer and damage evolution in a 3D interpenetrating metal/ceramic composite*, Materials Science and Engineering A, vol.551, pp.272-279, 2012.

[63] Sinchuk Y., Roy S., Gibmeier J., Piat R., Wanner A., *Numerical study of internal load transfer in metal/ceramic composites based on freeze-cast ceramic preforms and experimental validation*, Materials Science and Engineering A, vol.585, pp.10-16, 2013.

[64] Asghar Z., Requena G., Degischer H.P., Cloetens P., *Three-dimensional study of Ni aluminides in an AlSi12 alloy by means of light optical and synchrotron microtomography*, Acta Materialia, vol.57, pp.4125-4132, 2009.

[65] Asghar Z., Requena G., Kubel F., *The role of Ni and Fe aluminides on the elevated temperature strength of an AlSi12 alloy*, Materials Science and Engineering A, vol.527, pp.5691-5698, 2010.

[66] Asghar Z., Requena G., Boller E., *3D interpenetrating hybrid network of rigid phases in an AlSi10Cu5NiFe piston alloy*, Praktische Metallographie, vol.47, pp.471-486, 2010.

[67] Asghar Z., Requena G., Boller E., *Three-dimensional rigid multiphase networks providing high-temperature strength to cast AlSi10Cu5Ni1-2 piston alloys*, Acta Materialia, vol.59, pp.6420-6432, 2011.

[68] Winand H.M.A., Whitehouse A.F., Withers P.J., *An investigation of the isothermal creep response of Al-based composites by neutron diffraction*, Materials Science and Engineering A, vol.284, pp.103-113, 2000.

[69] Madgwick A., Mori T., Withers P.J., *A neutron diffraction study of creep and damage occurrence in an A359/SiC composite*, Materials Science and Engineering A, vol.333, pp.232-238, 2002.

[70] Lorentzen T., Clarke A.P., *Thermomechanically induced residual strains in Al/SiC$_p$ metal-matrix-composites*, Composites Science and Technology, vol.58, 345-353, 1998.

[71] Poletti C., Degischer H.P., Kremmer S., Marketz W., *Processing maps of Ti662 unreinforced and reinforced with TiC particles according to dynamic models*, Materials Science and Engineering A, vol.486, pp.127-137, 2008.

[72] Poletti C., Höltl G., *Mechanical properties of particle reinforced titanium and titanium alloys*, Kovove Materialy, vol.48, pp.87-95, 2010.

[73] Cho J.R., Dye D., Conlon K.T., Daymond M.R., Reed R.C., *Intergranular strain accumulation in a near-alpha titanium alloy during plastic deformation*, Acta Materialia, vol.50, pp.4847-4864, 2002.

[74] Raghunathan S.L., Stapleton A.M., Dashwood R.J., Jackson M., Dye D., *Micromechanics of Ti-10V-2Fe-3Al: In situ synchrotron characterization and modeling*, Acta Materialia vol.55, pp.6861-6872, 2007.

[75] Stapleton A.M., Raghunathan S.L., Bantounas I., Stone H.J., Lindney T.C., Dye D., *Evolution of lattice strain in Ti-6Al-4V during tensile loading at room temperature*, Acta Materialia, vol.56, pp.6186-6196, 2008.

[76] Warwick J.L.W., Jones N.G., Rahman K.M., Dye D., *Lattice strain evolution during tensile and compressive loading of CP Ti*, Acta Materialia, vol.60, pp.6720-6731, 2012.

[77] Warwick J.L.W., Coakley J., Raghunathan S.L., Talling R.J., Dye D., *Effect of texture on load partitioning in Ti-6Al-4V*, Acta Materialia, vol.60, pp.4117-4127, 2012.

[78] Liss K.-D., Yan K., *Thermo-mechanical processing in a synchrotron beam*, Materials Science and Engineering A, vol.528, pp.11-27, 2010.

[79] http://www.lkr.at/

[80] Lasagni F.A., *The role of Si on the microstructure of Al casting alloys and short fibre composites*, PhD thesis, Vienna University of Technology, 2006.

[81] http://www.kspg.com/

[82] Flourez A., Koos R., *Influence of solution treatment time and ageing on microstructure and hardness of an AlSi10Cu6Ni2Mg piston*, Internal report, 2011.

[83] Poletti C., *Hot deformation and properties of PRTi alloys*, PhD Thesis, Vienna University of Technology, 2005.

[84] Department of Physical Metallurgy, National Center for Metallurgical Research, CENIM-CSIC, Av. Gregorio del Amo 8, 28040 Madrid, Spain.

[85] http://www.alpoco.com/

[86] http://www.esk-sic.de/

[87] Bauer B., *Enhancement of creep resistance by particle reinforcement,* PhD Thesis, Vienna University of Technology, pp.75-81, 2009, available from: http://media.obvsg.at/display_object-id=401417.

[88] Hofmann M, Schneider R, Seidl G.A., Rebelo-Kornmeier J., Wimpory R.C., Garbe U., Brokmeier H.-G., *The new materials science diffractometer STRESS-SPEC at FRM-II*, Physica B , vol.385-386, pp.1035-1037, 2006.

[89] Requena G, Garcés G, Fernández R, Schöbel M., Determination of Internal Stresses in Lightweight Metal Matrix Composites, in *Neutron Diffraction*, ed. by Khidirov I., InTech, pp. 268-269, 2012, available from: http://www.intechopen.com/books/neutron-diffraction/determination-of-internal-stresses-in-lightweight-metal-matrix-composites.

[90] http://www.esrf.eu/UsersAndScience/Experiments/StructMaterials/ID15 (accesed March 2013).

[91] http://www.instron.com

[92] Ed. by Lippmann T., Lottermoser L., Beckmann F., Martins R.V., Dose T., Kirchhof R., Schreyer A., Caliebe W., Drube W., Rickers K., Schneider J. R, HASYLAB Annual Report, HASYLAB/DESY, Hamburg, 2007.

[93] http://www.hzg.de/central_departments/genf/branch/desy/004909/index_0004909.html (accessed March 2013)

[94] Randau C., Garbe U., Brokmeier H.-G, *Stress Texture Calculator: A software tool to extract texture, strain and microstructure information from area-detector measurements*, Journal of Applied Crystallography, vol.44, pp.641-646, 2011.

[95] Hammersley A.P., Svensson S.O., Hanfland M., Fitch A.N., Häusermann D., Two-dimensional detector software: From real detector to idealized image or two-theta scan, High Pressure Research, vol.14, pp.235-248, 1996.

[96] Hauk V.M., Oudelhoven R.W.M., Vaessen G.J.H., *State of residual stress in the near surface region of homogeneous and heterogeneous materials after grinding*, Metallurgical transactions A, vol.13, pp.1239-1244, 1982.

[97] Hutchings M.T., Withers P.J., Holden T.M., Lorentzen T., *Introduction to the characterization of residual stresses by neutron diffraction*, Taylor and Francis, 2005.

[98] Wern H., Johannes R., Walz H., *Dependence of the X-ray elastic constants on the diffraction plane*, Physica Status Solidi B, vol.206, pp.545-557, 1998.

[99] Bauer B., Requena G., Lieblich M., in *Proceedings of the International Conference on Powder Metallurgy and Particulate Materials,* Las Vegas, P.9-1-9-13, 2009.

[100] Shackelford J.F., Alexander W., *Materials Science and Engineering Handbook*, 3rd edition, CRC Press, 2000.

[101] Fréour S., Gloaguen D., Francois M., Perronnet A., Guillén R., *Determination of single-crystal elasticity constants in a cubic phase within a multiphase alloy: X-ray diffraction measurements and inverse-scale transition modelling*, Journal of Applied Crystallography, vol.38, pp.30-37, 2005.

[102] Ledbetter M., Ogi H., Kai S., Kim S., Hirao M., Elastic constants of body-centered-cubic titanium monocrystals, Journal of Applied Physics, vol.95, pp.4642-4644, 2004.

[103] ImageJ, available in http://rsbweb.nih.gov/ij/.

[104] http://rsbweb.nih.gov/ij/plugins/polar-transformer.html

[105] Lutterotti L., Bortolotti M., Ischia G., Lonardelli I., Wenk H.-R., *Rietveld texture analysis from diffraction images*, Zeitschrift für Kristallographie, Supplement, vol.1, pp.125-130, 2007.

[106] Popa N.C., *The (hkl) dependence of diffraction-line broadening caused by strain and size for all laue groups in rietlveld refinement*, Journal of Applied Crystallography, vol.31, pp.176-180, 1998.

[107] Williams R.O., *Analytical methods for representing complex textures by biaxial pole figures*, Journal of Applied Physics, vol.39, pp.4329-4335, 1968.

[108] Imhof J., *The resolution of orientation space with reference to pole figure resolution*, Textures & Microstructures, vol.4, pp.189-200, 1982.

[109] Matthies S., Vinel G.W., *On the reproduction of the orientation distribution function of texturized samples from reduced pole figures using the conception of a conditional ghost correction*, Physica Status Solidi B, vol.112, pp.K111-K114, 1982.

[110] *The Rietveld Method*, ed. by Young R.A., Oxford University Press, New York, 1996.

[111] Withers P.J., Preuss M., Steuwer A., Pang J.W.L., *Methods for obtaining the strain-free lattice parameter when using diffraction to determine residual stress*, Journal of Applied Crystallography, vol.40, pp.891-904, 2007.

[112] Asghar Z, Requena G., *Three dimensional post-mortem study of damage after compression of cast Al-Si alloys*, Materials Science and Engineering A, vol.591, pp.136-143, 2014.

[113] Bruno G., Fernández R., González-Doncel G., *Gauge volume effects in residual stress determination by neutron diffraction: The strength differential effect in metal matrix composites*, Materials Science and Engineering A, vol.437, pp.100-108, 2006.

[114] Delannay F., Thermal stresses and thermal expansion in MMCs, in *Comprehensive composite materials*, ed. by Kelly A., Zweben C., vol.3, Elsevier; pp.341-369, 2000.

[115] Nam T.H., Requena G., Degischer H.P., *Thermal expansion behaviour of aluminum matrix composites with densely packed SiC particles*, Composites Part A, vol.39, pp.856-865, 2008.

[116] Fitzpatrick M.E., Hutchings M.T., Withers P.J., *Separation of macroscopic, elastic mismatch and thermal expansion misfit stresses in metal matrix composite quenched plates from neutron diffraction measurements*, Acta Materialia, vol.45, pp.4867-4876, 1997.

[117] Klaska A.M., Beck T., Wanner A., Löhe D., *Residual stress and damage development in the aluminium alloy EN AW-6061 particle reinforced with Al_2O_3 under thermal fatigue loading*, Materials Science and Engineering A, vol.501, pp.6-15, 2009.

[118] Majumdar S., Singh J.P., Kupperman D., Krawitz A.D., *Application of neutron diffraction to measure residual strains in various engineering composite materials*, Journal of Engineering Materials and Technology, vol.113, pp.51-59, 1991.

[119] Daymond M.R., Withers P.J., *A synchrotron radiation study of transient internal strain changes during the early stages of thermal cycling in an Al/SiC_W MMC*, Scripta Materialia, vol.35, pp.1229-1234, 1996.

[120] Humphreys F.J., Hatherly M., *Recrystallization and related annealing phenomena*, Elsevier, 2004.

[121] Requena G., Canelo Yubero D., Fiedler G., Garcés G., Poletti C., *In-situ diffraction during deformation and synchrotron tomography of light alloys*, MECA SENS VI, 7-9 September, Hamburg (Germany), 2011.

[122] Donaiche M.J, *Titanium. A Technical Guide*, ASM International, 2nd ed., 2000.

[123] Warwick J.L.W., Jones N.G., Bantounas I., Preuss M., Dye D., *In situ observation of texture and microstructure evolution during rolling and globularization of Ti-6Al-4V*, Acta Materialia, vol.61, pp.1603-1615, 2013.

8 Appendix

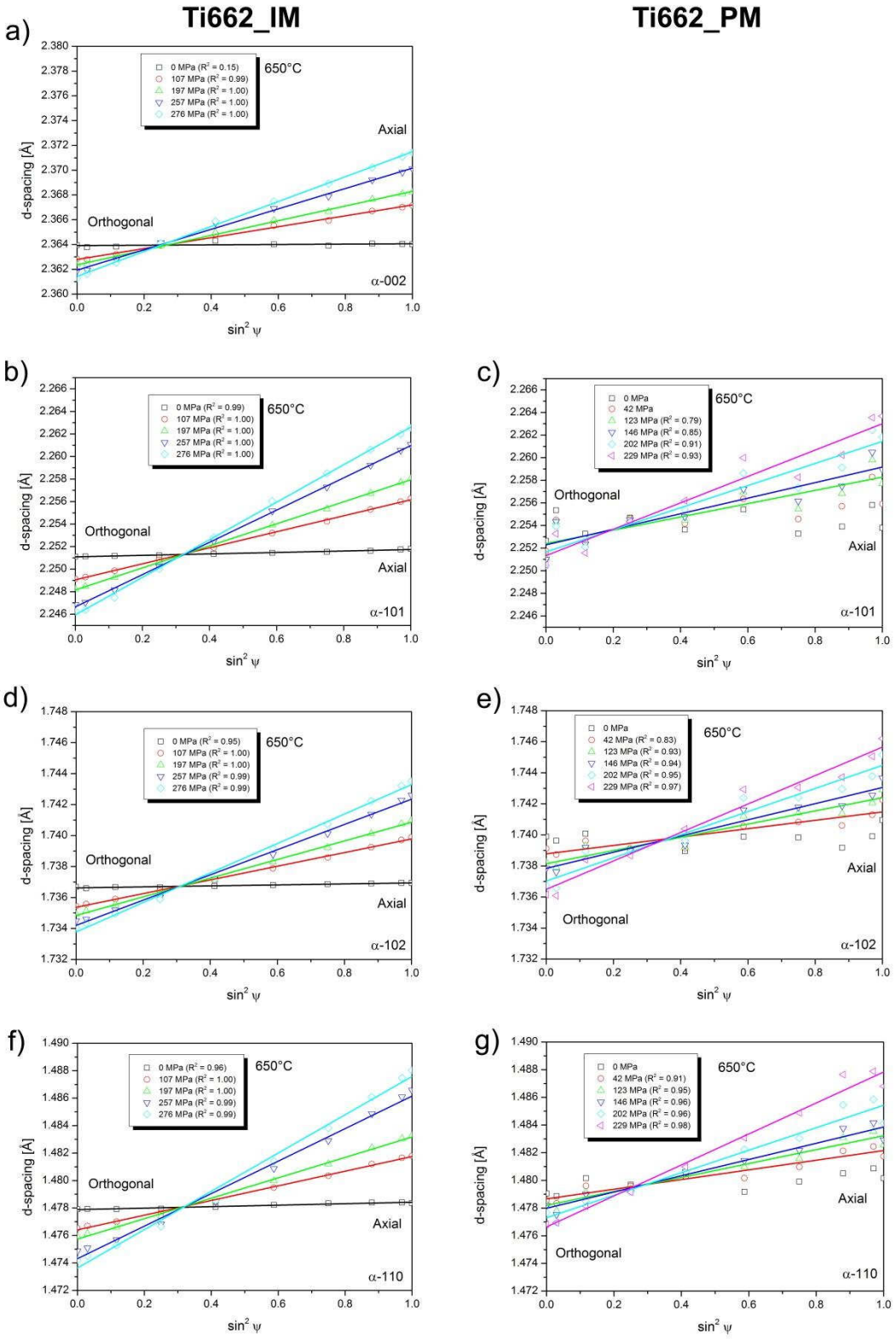

Fig. A. 1. *d* vs $\sin^2 \psi$ plots of α-Ti reflections with the linear fits at different tension stresses at 650°C in a) α-002 for IM, b) α-101 for IM, c) α-101 for PM, d) α-102 for IM, e) α-102 for PM, f) α-110 for IM and g) α-110 for PM. R^2 values are also indicated.

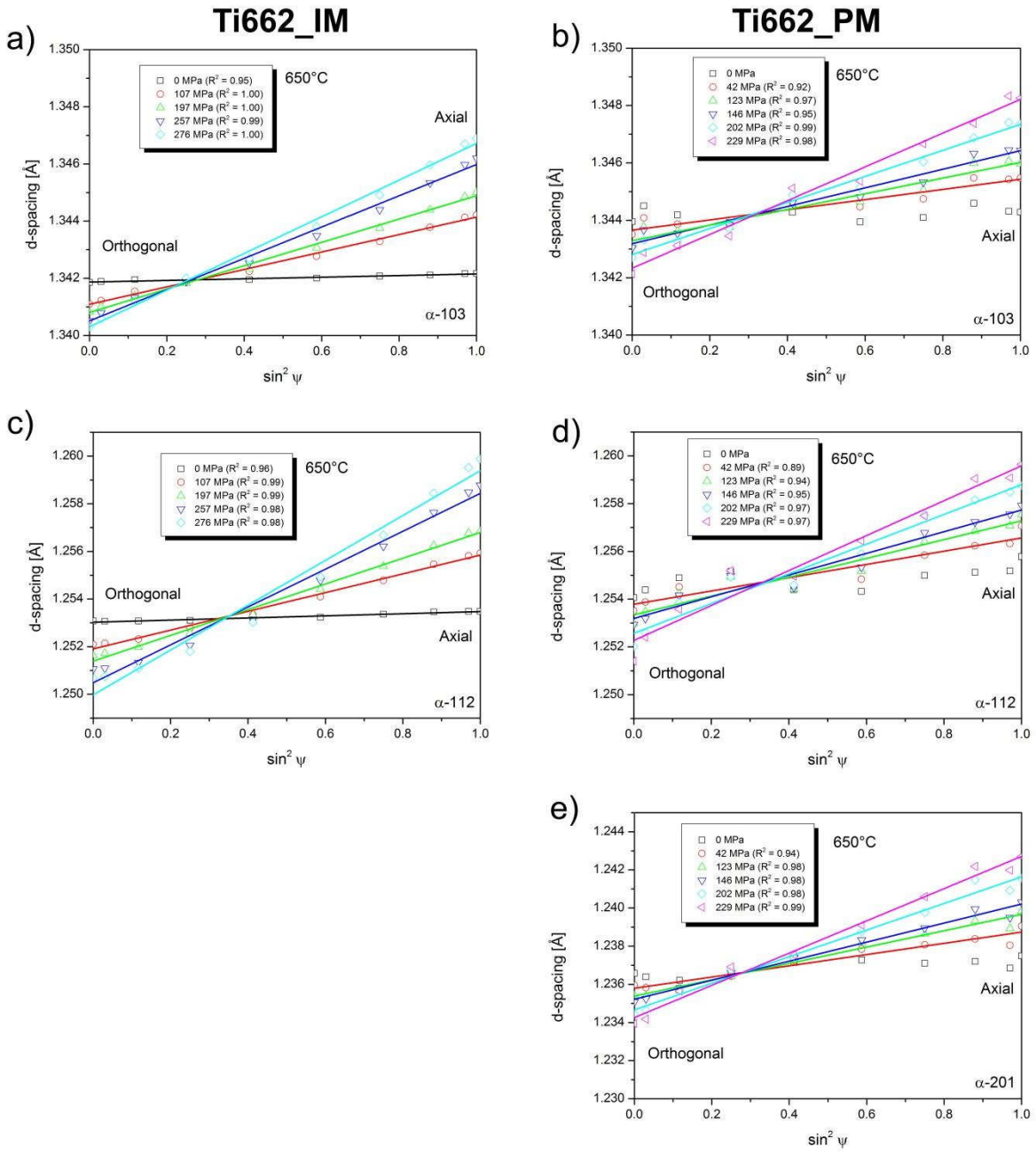

Fig. A. 2. *d* vs $\sin^2 \psi$ plots of α-Ti reflections with the linear fits at different tension stresses at 650°C in a) α-103 for IM, b) α-103 for PM, c) α-112 for IM, d) α-112 for PM and e) α-201 for PM. R^2 values are also indicated.

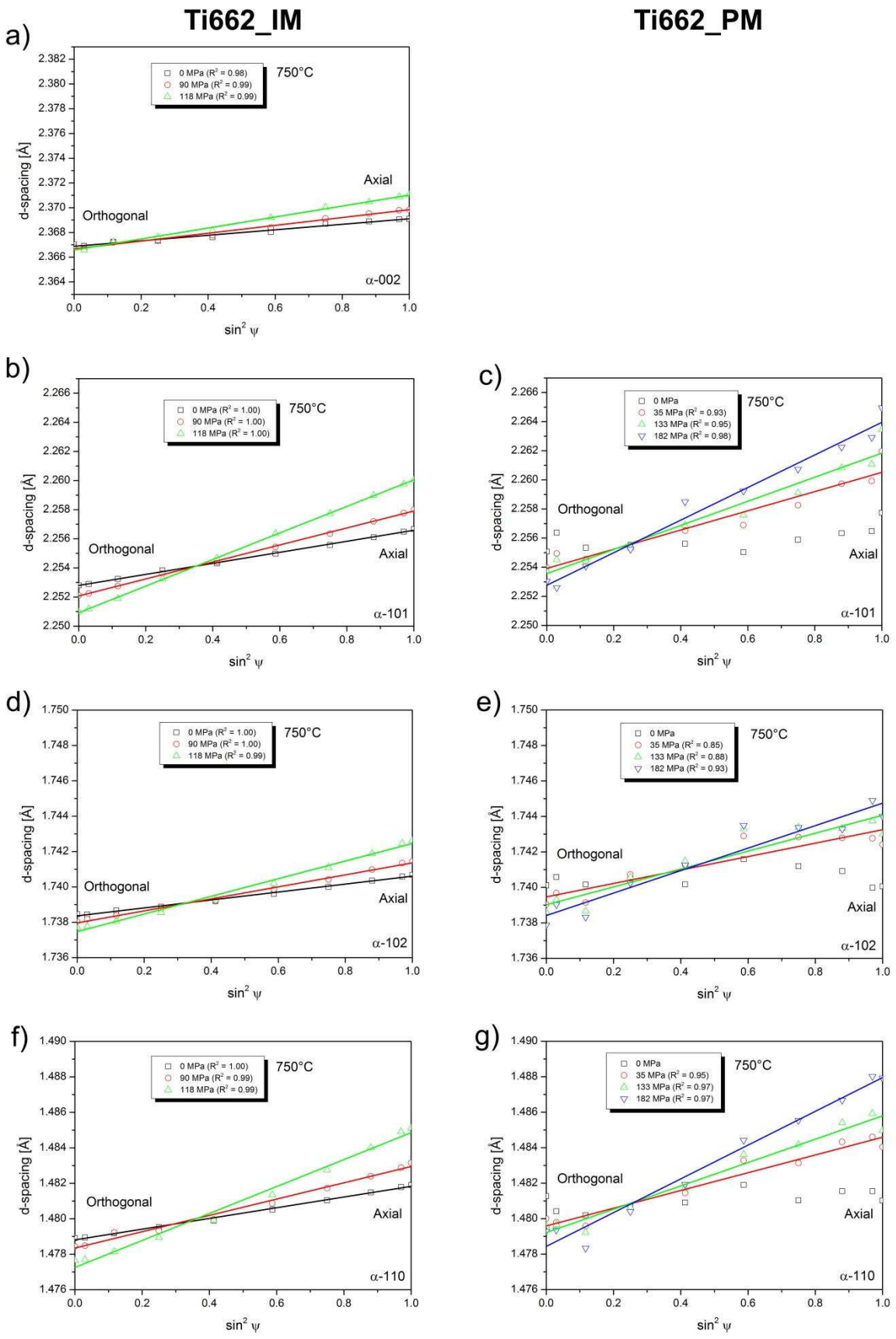

Fig. A. 3. *d* vs $\sin^2 \psi$ plots of α-Ti reflections with the linear fits at different tension stresses at 750°C in a) α-002 for IM, b) α-101 for IM, c) α-101 for PM, d) α-102 for IM, e) α-102 for PM, f) α-110 for IM and g) α-110 for PM. R^2 values are also indicated.

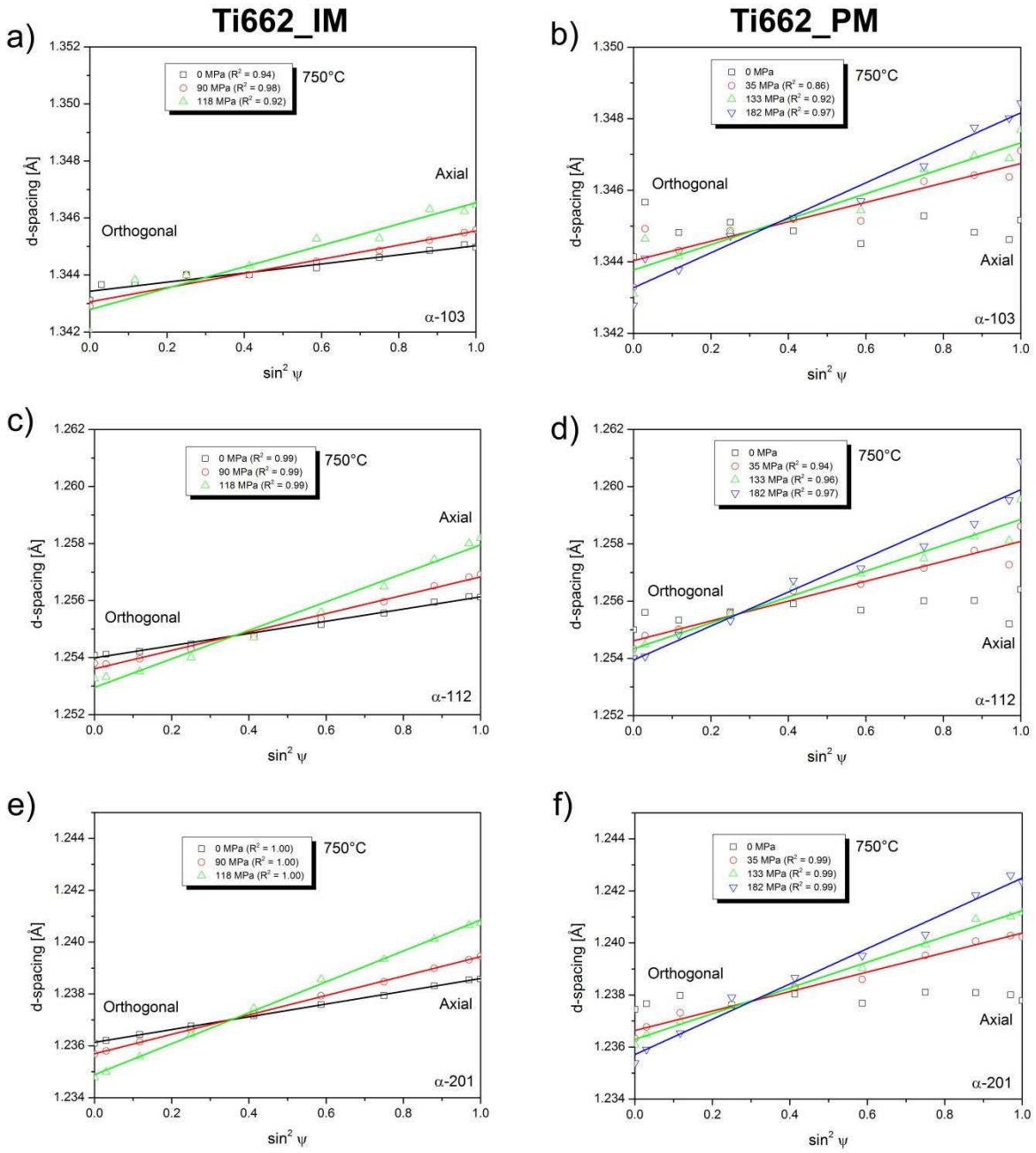

Fig. A. 4. *d* vs $\sin^2 \psi$ plots of α-Ti reflections with the linear fits at different tension stresses at 750°C in a) α-103 for IM, b) α-103 for PM, c) α-112 for IM, d) α-112 for PM, e) α-201 for IM and f) α-201 for PM. R^2 values are also indicated.

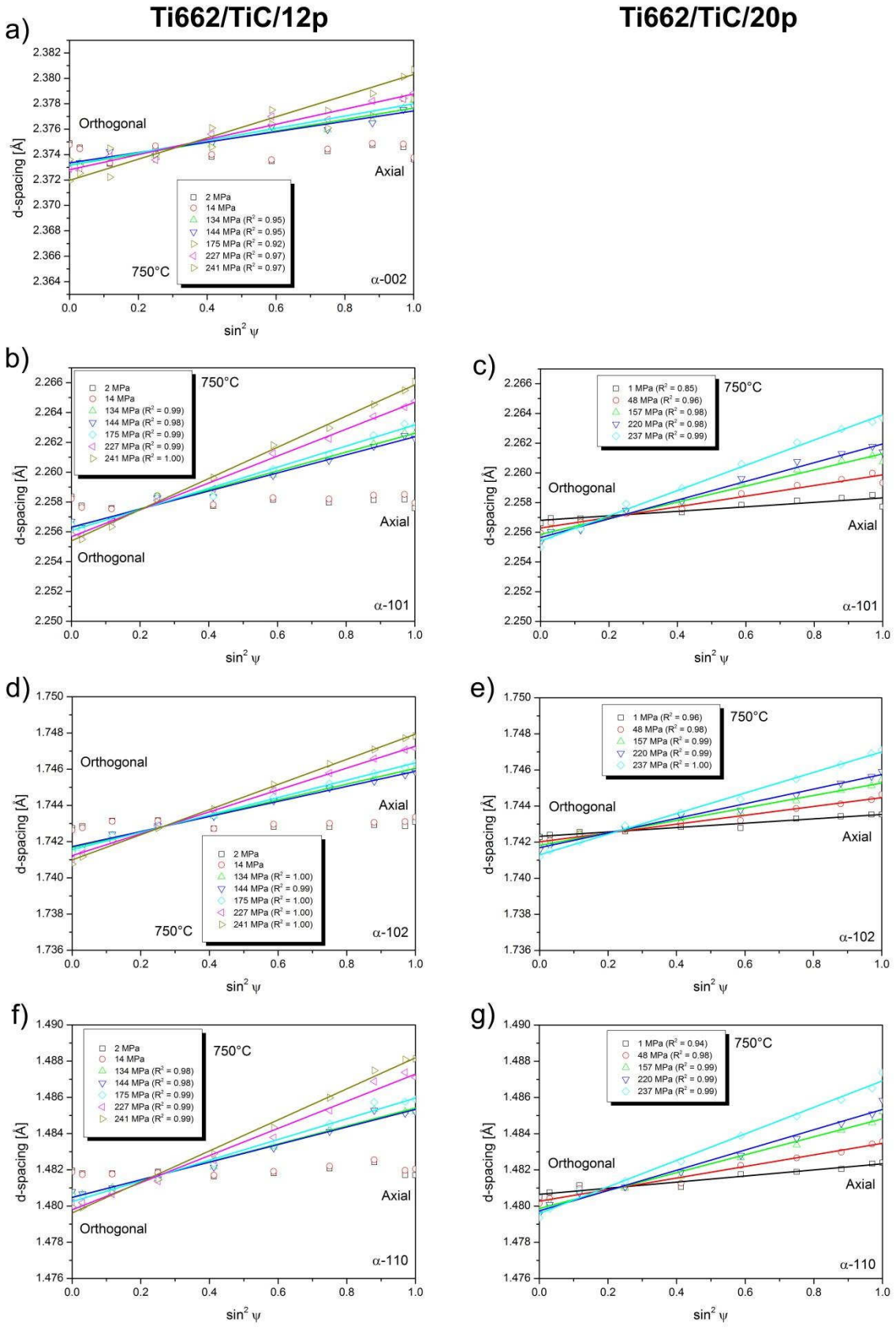

Fig. A. 5. *d* vs $\sin^2 \psi$ plots of α-Ti reflections with the linear fits at different tension stresses at 650°C in a) α-002 for Ti662/TiC/12p, b) α-101 for Ti662/TiC/12p, c) α-101 for Ti662/TiC/20p, d) α-102 for Ti662/TiC/12p, e) α-102 for Ti662/TiC/20p, f) α-110 for Ti662/TiC/12p and g) α-110 for Ti662/TiC/20p. R^2 values are also indicated.

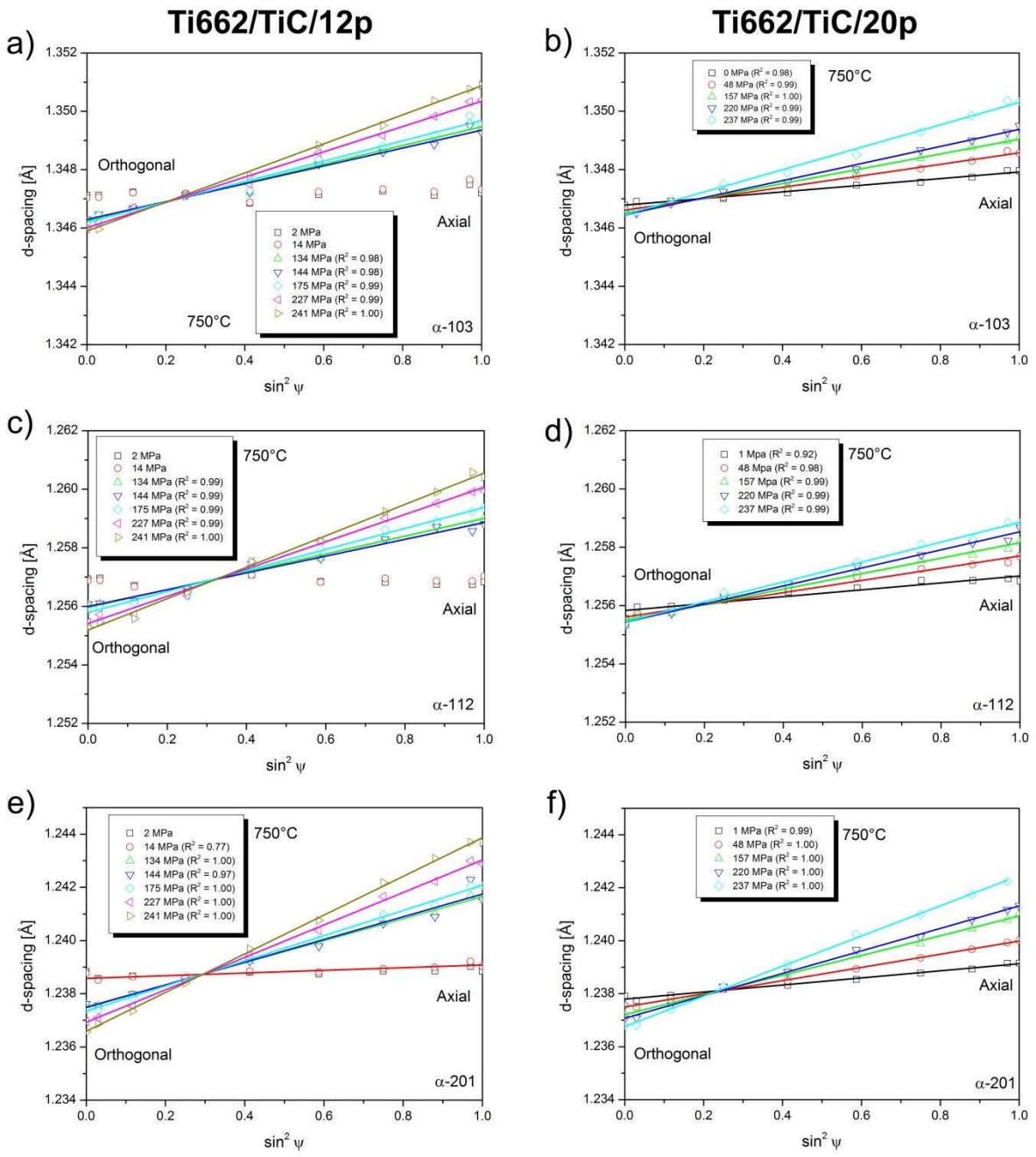

Fig. A. 6. *d* vs $\sin^2 \psi$ plots of α-Ti reflections with the linear fits at different tension stresses at 650°C in a) α-103 for Ti662/TiC/12p, b) α-103 for Ti662/TiC/20p, c) α-112 for Ti662/TiC/12p, d) α-112 for Ti662/TiC/20p, e) α-201 for Ti662/TiC/12p and f) α-201for Ti662/TiC/20p. R^2 values are also indicated.